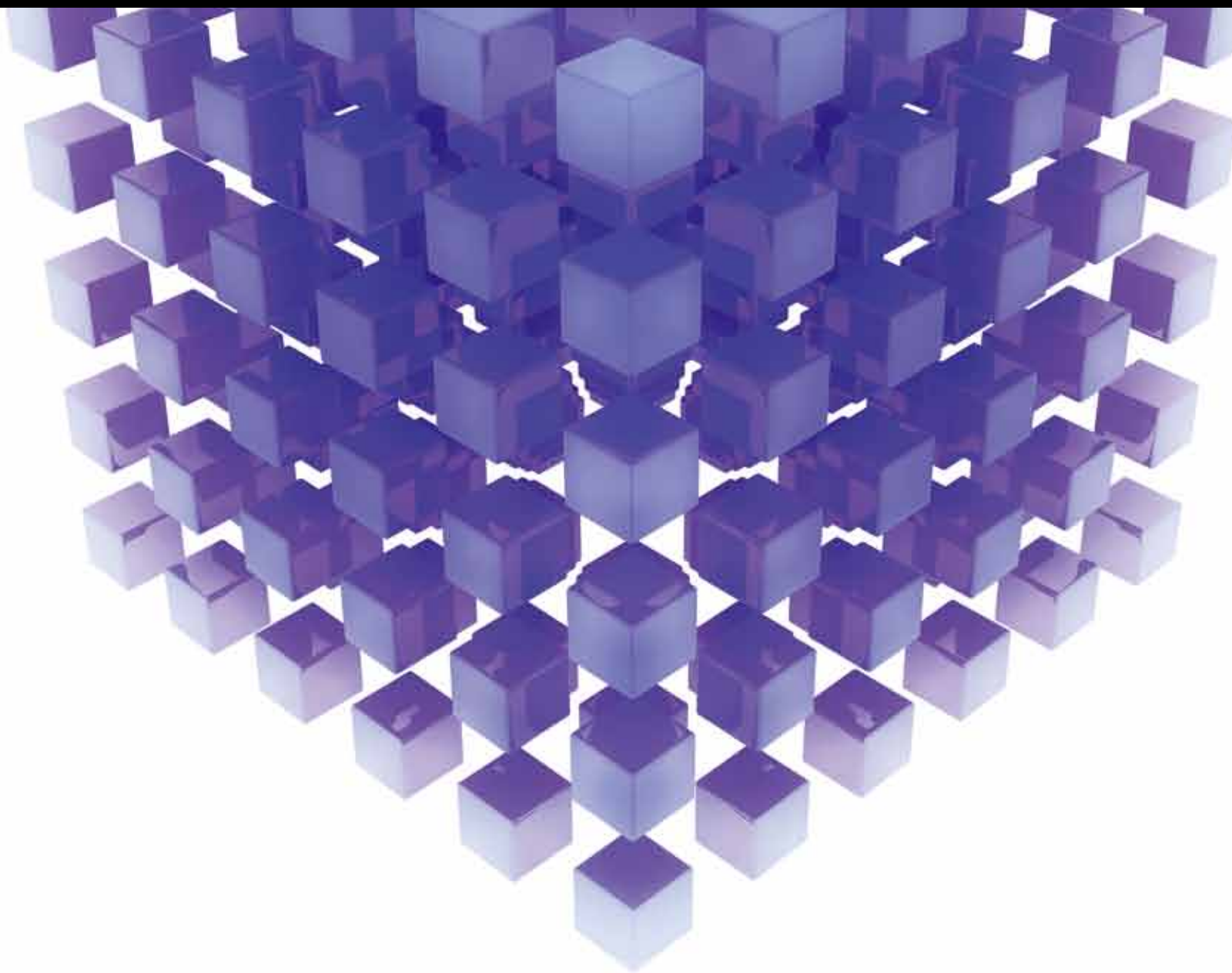


MATHEMATICAL PROBLEMS IN ENGINEERING

NEW STRATEGIES AND CHALLENGES IN SHM FOR AEROSPACE AND CIVIL STRUCTURES

GUEST EDITORS: ALESSANDRO MARZANI, ZHONGQING SU, AND IVAN BARTOLI





New Strategies and Challenges in SHM for Aerospace and Civil Structures

Mathematical Problems in Engineering

New Strategies and Challenges in SHM for Aerospace and Civil Structures

Guest Editors: Alessandro Marzani, Zhongqing Su,
and Ivan Bartoli



Copyright © 2013 Hindawi Publishing Corporation. All rights reserved.

This is a special issue published in “Mathematical Problems in Engineering.” All articles are open access articles distributed under the Creative Commons Attribution License, which permits unrestricted use, distribution, and reproduction in any medium, provided the original work is properly cited.

Editorial Board

Mohamed Abd El Aziz, Egypt
E. M. Abdel-Rahman, Canada
Rashid K. Abu Al-Rub, USA
Salvatore Alfonzetti, Italy
Igor Andrianov, Germany
Sebastian Anita, Romania
W. Assawinchaichote, Thailand
Erwei Bai, USA
Ezzat G. Bakhoun, USA
José Manoel Balthazar, Brazil
Rasajit K. Bera, India
Jonathan N. Blakely, USA
Stefano Boccaletti, Spain
Daniela Boso, Italy
M. Boutayeb, France
Michael J. Brennan, UK
John Burns, USA
Salvatore Caddemi, Italy
Piermarco Cannarsa, Italy
Jose E. Capilla, Spain
Carlo Cattani, Italy
Marcelo M. Cavalcanti, Brazil
Diego J. Celentano, Chile
Mohammed Chadli, France
Arindam Chakraborty, USA
Yong-Kui Chang, China
Michael J. Chappell, UK
Kui Fu Chen, China
Xinkai Chen, Japan
Kue-Hong Chen, Taiwan
Jyh Horng Chou, Taiwan
Slim Choura, Tunisia
Cesar Cruz-Hernandez, Mexico
Swagatam Das, India
Filippo de Monte, Italy
Maria de Pinho, Portugal
Antonio Desimone, Italy
Yannis Dimakopoulos, Greece
Baocang Ding, China
Joao B. R. Do Val, Brazil
Daoyi Dong, Australia
Balram Dubey, India
Horst Ecker, Austria
M. Onder Efe, Turkey
Elmetwally Elabbasy, Egypt

Alex Elias-Zuniga, Mexico
Anders Eriksson, Sweden
Vedat S. Erturk, Turkey
Qi Fan, USA
Moez Feki, Tunisia
Ricardo Femat, Mexico
Rolf Findeisen, Germany
R. A. Fontes Valente, Portugal
C. R. Fuerte-Esquivel, Mexico
Zoran Gajic, USA
Ugo Galvanetto, Italy
Xin-Lin Gao, USA
Furong Gao, Hong Kong
Behrouz Gatmiri, Iran
Oleg V. Gendelman, Israel
Didier Georges, France
P. Batista Gonçalves, Brazil
Oded Gottlieb, Israel
Fabrizio Greco, Italy
Quang Phuc Ha, Australia
M. R. Hajj, USA
Thomas Hanne, Switzerland
Tasawar Hayat, Pakistan
Katica R. Hedrih, Serbia
M.I. Herreros, Spain
Wei-Chiang Hong, Taiwan
J. Horacek, Czech Republic
Chuangxia Huang, China
Gordon Huang, Canada
Yi Feng Hung, Taiwan
Hai-Feng Huo, China
Asier Ibeas, Spain
Anuar Ishak, Malaysia
Reza Jazar, Australia
Zhijian Ji, China
J. Jiang, China
J. J. Judice, Portugal
Tadeusz Kaczorek, Poland
Tamas Kalmar-Nagy, USA
Tomasz Kapitaniak, Poland
Hamid Reza Karimi, Norway
Metin O. Kaya, Turkey
Nikolaos Kazantzis, USA
Farzad Khani, Iran
Kristian Krabbenhoft, Australia
Jurgen Kurths, Germany
Claude Lamarque, France

F. Lamnabhi-Lagarrigue, France
Marek Lefik, Poland
Stefano Lenci, Italy
Roman Lewandowski, Poland
Ming Li, China
Shanling Li, Canada
Tao Li, China
Jian Li, China
Shihua Li, China
Teh-Lu Liao, Taiwan
P. Liatsis, UK
Jui-Sheng Lin, Taiwan
Shueei M. Lin, Taiwan
Yuji Liu, China
Wanquan Liu, Australia
Bin Liu, Australia
Paolo Lonetti, Italy
V. C. Loukopoulos, Greece
Junguo Lu, China
Chien-Yu Lu, Taiwan
Alexei Mailybaev, Brazil
Manoranjan Maiti, India
O. Daniel Makinde, South Africa
R. Martinez-Guerra, Mexico
Driss Mehdi, France
Roderick Melnik, Canada
Xinzhu Meng, China
Y. Vladimirovich Mikhlin, Ukraine
G. Milovanovic, Serbia
Ebrahim Momoniat, South Africa
Trung Nguyen Thoi, Vietnam
Hung Nguyen-Xuan, Vietnam
Ben T. Nohara, Japan
Anthony Nouy, France
Sotiris K. Ntouyas, Greece
Gerard Olivar, Colombia
Claudio Padra, Argentina
Francesco Pellicano, Italy
Matjaz Perc, Slovenia
Vu Ngoc Phat, Vietnam
A. Pogromsky, The Netherlands
Seppo Pohjolainen, Finland
Stanislav Potapenko, Canada
Sergio Preidikman, USA
Carsten Proppe, Germany
Hector Puebla, Mexico
Justo Puerto, Spain
Dane Quinn, USA



K. Ramamani Rajagopal, USA
Gianluca Ranzi, Australia
Sivaguru Ravindran, USA
G. Rega, Italy
Pedro Ribeiro, Portugal
J. Rodellar, Spain
R. Rodriguez-Lopez, Spain
A. J. Rodriguez-Luis, Spain
Ignacio Romero, Spain
Hamid Ronagh, Australia
Carla Roque, Portugal
Rubén Ruiz García, Spain
Manouchehr Salehi, Iran
Miguel A. F. Sanjuán, Spain
Ilmar Ferreira Santos, Denmark
Nickolas S. Sapidis, Greece
Bozidar Sarler, Slovenia
Andrey V. Savkin, Australia
Massimo Scalia, Italy
Mohamed A. Seddeek, Egypt
Alexander P. Seyranian, Russia
Leonid Shaikhet, Ukraine
Cheng Shao, China
Daichao Sheng, Australia
Tony Sheu, Taiwan
Jian-Jun Shu, Singapore

Zhan Shu, UK
Dan Simon, USA
Luciano Simoni, Italy
Grigori M. Sisoiev, UK
Christos H. Skiadas, Greece
Davide Spinello, Canada
Sri Sridharan, USA
Rolf Stenberg, Finland
Changyin Sun, China
Jitao Sun, China
Xi-Ming Sun, China
Andrzej Swierniak, Poland
Allen Tannenbaum, USA
Cristian Toma, Romania
Irina N. Trendafilova, UK
Alberto Trevisani, Italy
Jung-Fa Tsai, Taiwan
John Tsiniias, Greece
Kuppalapalle Vajravelu, USA
Victoria Vampa, Argentina
Josep Vehi, Spain
Stefano Vidoli, Italy
Xiaojun Wang, China
Dan Wang, China
Youqing Wang, China
Yongqi Wang, Germany
Cheng C. Wang, Taiwan

Moran Wang, USA
Yijing Wang, China
Gerhard-Wilhelm Weber, Turkey
Jeroen A. S. Witteveen, USA
Kwok-Wo Wong, Hong Kong
Ligang Wu, China
Zheng-Guang Wu, China
Wang Xing-yuan, China
X. Frank Xu, USA
Xuping Xu, USA
Jun-Juh Yan, Taiwan
Xing-Gang Yan, UK
Suh-Yuh Yang, Taiwan
Mahmoud T. Yassen, Egypt
Mohammad I. Younis, USA
Huang Yuan, Germany
S. P. Yung, Hong Kong
Ion Zaballa, Spain
Arturo Zavala-Rio, Mexico
Ashraf M. Zenkour, Saudi Arabia
Yingwei Zhang, USA
Xu Zhang, China
Lu Zhen, China
Liancun Zheng, China
Jian Guo Zhou, UK
Zexuan Zhu, China
Mustapha Zidi, France

Contents

New Strategies and Challenges in SHM for Aerospace and Civil Structures, Alessandro Marzani, Zhongqing Su, and Ivan Bartoli
Volume 2013, Article ID 614050, 2 pages

Locally Resonant Band Gaps in Flexural Vibrations of a Timoshenko Beam with Periodically Attached Multioscillators, Zhenyu Wang, Pei Zhang, and Yongqiang Zhang
Volume 2013, Article ID 146975, 10 pages

Warped Wigner-Hough Transform for Defect Reflection Enhancement in Ultrasonic Guided Wave Monitoring, Luca De Marchi, Emanuele Baravelli, Giampaolo Cera, Nicolò Speciale, and Alessandro Marzani
Volume 2012, Article ID 358128, 15 pages

Finite Element Modelling Tuned on Experimental Testing for the Structural Health Assessment of an Ancient Masonry Arch Bridge, G. Castellazzi, S. De Miranda, and C. Mazzotti
Volume 2012, Article ID 495019, 18 pages

Fractal Dimension Analysis of Higher-Order Mode Shapes for Damage Identification of Beam Structures, Runbo Bai, Maosen Cao, Zhongqing Su, Wiesław Ostachowicz, and Hao Xu
Volume 2012, Article ID 454568, 16 pages

Application of Kernel Density Estimation in Lamb Wave-Based Damage Detection, Long Yu and Zhongqing Su
Volume 2012, Article ID 406521, 24 pages

Higher-Harmonic Generation Analysis in Complex Waveguides via a Nonlinear Semianalytical Finite Element Algorithm, Claudio Nucera and Francesco Lanza di Scalea
Volume 2012, Article ID 365630, 16 pages

Wave Propagation Analysis in Composite Laminates Containing a Delamination Using a Three-Dimensional Spectral Element Method, Fucai Li, Haikuo Peng, Xuewei Sun, Jinfu Wang, and Guang Meng
Volume 2012, Article ID 659849, 19 pages

Editorial

New Strategies and Challenges in SHM for Aerospace and Civil Structures

Alessandro Marzani,¹ Zhongqing Su,² and Ivan Bartoli³

¹ *Department of Civil, Chemical, Environmental and Materials Engineering, University of Bologna, 40126 Bologna, Italy*

² *Department of Mechanical Engineering, The Hong Kong Polytechnic University, Hung Hom, Kowloon, Hong Kong*

³ *Department of Civil, Architectural and Environmental Engineering, 3141 Chestnut Street, Philadelphia, PA 19104, USA*

Correspondence should be addressed to Alessandro Marzani; alessandro.marzani@unibo.it

Received 18 February 2013; Accepted 18 February 2013

Copyright © 2013 Alessandro Marzani et al. This is an open access article distributed under the Creative Commons Attribution License, which permits unrestricted use, distribution, and reproduction in any medium, provided the original work is properly cited.

This special issue includes six original research papers discussing new approaches and laboratory validations as well as practical field applications of structural health monitoring (SHM) techniques for aerospace, mechanical, and civil structures. A variety of methodologies including guided waves, finite element model updating, and vibration-based methods are presented. A brief description of each contribution is provided below.

A team of researchers from the University of Bologna (Italy) presented a nonlinear signal processing approach based on a warped frequency transform (WFT) to compensate for the dispersive behavior of ultrasonic guided waves, followed by a Wigner-Ville time-frequency analysis and a Hough transform to further improve the defect detectability and localization accuracy of Lamb wave inspection systems. As a result, an automatic detection procedure to locate defect-induced reflections was demonstrated and successfully tested by analyzing numerically simulated Lamb waves propagating in an aluminum plate.

A different group of researchers from the University of Bologna (Italy) discussed the structural health monitoring of an ancient railway masonry arch bridge located in Bologna. In particular, they developed a three-dimensional finite element model of the entire bridge and updated leveraging data from an in situ experimental campaign involving static and dynamic load tests performed on the structure. The study included also material testing performed on samples of the masonry structure extracted from the bridge. The structural performances of the bridge both in its actual state and in the case of a retrofitting action were assessed.

A research group consisting of researchers from Shandong Agricultural University (China), Hohai University (China), the Polish Academy of Sciences (Poland), and The Hong Kong Polytechnic University (Hong Kong) proposed a fractal dimension-based analysis of mode shapes for damage identification of beam structures. In particular, they were able to obviate false peaks of high magnitude in fractal dimension due to the natural inflexions of higher-order mode shapes by using specially designed affine transformations, thus overcoming limitations of classical fractal-based methods. The new method was numerically demonstrated on a multiple cracked cantilever beam and was experimentally validated using a scanning laser vibrometer to acquire higher-order mode shapes.

A team from the Northwestern Polytechnical University (China) and The Hong Kong Polytechnic University (Hong Kong) presented a paper on the estimation of the probability density function of measured data extracted from Lamb wave-based damage detection procedures in the presence of strong measurement noise. In particular, they proposed and validated a nonparametric method based on the kernel density estimation in order to enhance the estimation of the probability density function. The results showed that the nonparametric methods outperformed the empirical methods in terms of accuracy.

A group from the University of California, San Diego (USA), presented a work on the generation of higher harmonics in waveguides of complex cross-section. The paper extended classical semianalytical finite element formulations to the nonlinear regime analysis for predicting second-

harmonic generations. Nonlinear guided waves represent an attractive phenomenon for structural health monitoring since they exhibit large sensitivity to structural damage compared to traditional approaches based on linear wave features. Results were presented for a railroad track and a viscoelastic plate. For the investigated cases, optimum combinations of primary wave modes and resonant double-harmonic nonlinear wave modes have been identified.

Finally, a group from the Shanghai Jiao Tong University (China) reported a three-dimensional spectral element method (SEM) for the analysis of Lamb wave propagation in composite laminates containing delamination. SEM is more efficient than conventional finite element method (FEM) in simulating wave propagation in structures because of its unique diagonal form of the mass matrix. The effectiveness of the method was validated by comparing the simulation results with analytical solutions based on the transfer matrix method. By a parametric analysis it was demonstrated that symmetric Lamb waves can be insensitive to delamination at certain interfaces of laminates while the antisymmetric waves are more suited for identification of delamination in composite structures.

*Alessandro Marzani
Zhongqing Su
Ivan Bartoli*

Research Article

Locally Resonant Band Gaps in Flexural Vibrations of a Timoshenko Beam with Periodically Attached Multioscillators

Zhenyu Wang, Pei Zhang, and Yongqiang Zhang

College of Civil Engineering and Architecture, Zhejiang University, Hangzhou 310058, China

Correspondence should be addressed to Zhenyu Wang; wzyu@zju.edu.cn

Received 22 October 2012; Revised 27 January 2013; Accepted 27 January 2013

Academic Editor: Zhongqing Su

Copyright © 2013 Zhenyu Wang et al. This is an open access article distributed under the Creative Commons Attribution License, which permits unrestricted use, distribution, and reproduction in any medium, provided the original work is properly cited.

A new beam structure with periodically attached multioscillators is proposed based on the idea of locally resonant (LR) phononic crystals (PCs) to reduce flexural vibrations in the frequency-multiplication ranges. Wave band structures of the new beam are derived by using the transfer matrix method. The multiple band gaps in the beam are then verified by the frequency response function (FRF), which is calculated through the finite element method. In addition, simplified models are proposed, which contribute to the calculation of the edge frequencies of the band gaps and enhance the understanding of the LR mechanism of PCs. The accuracy of the simplified models is proven by comparing them with the results derived from the analytical model under different beam structure parameters. The results suggest that lower frequencies and ranges of frequency multiplications can be achieved in the band gaps which are obtained from the new beam structure with multioscillators in a unit cell. Therefore, the ideas presented in this paper have the potential to be used in developing new devices with frequency-multiplication characteristics for vibration isolation or noise control in aerospace and civil structures.

1. Introduction

Methods to control the propagation of elastic waves, such as vibration reduction and noise isolation, are often the focus of engineering studies. Much research has been conducted over many years to suppress unwanted vibration or noise. A variety of vibration control technologies, including visco-elastic materials, springs, soft materials, hydraulic dampers, and pneumatic isolators, among others, were gradually developed and are widely used in engineering practice [1]. As technology progresses, scientific equipment and structures are developed further to be more complex and precise. The control of the higher-order vibration or coupled vibration in these complicated structures, as well as the higher precision and flexibility of the vibration isolation in precise instruments, is increasingly important. Currently, the traditional vibration/noise control technologies are facing new challenges.

In the last decade, the emergence and development of phononic crystals (PCs) have inspired new ideas for wave control [2–4]. PCs are artificial composite materials that are formed by periodic variations of properties and structures of the material. One notable aspect of these PCs is the

wave filtering property of the so-called “band gaps,” which are selected frequency ranges in which elastic waves cannot propagate through the periodic system. This property means that the vibration can be well mitigated when its frequency is located in the specified band gaps of the PCs. In addition, the frequency-space distributions of the band gaps for a PC can be regulated by the properties, geometries, and arrangements of the elements composing the so-called “artificial crystal.” Such a unique property promises an enormous potential for the development of vibration isolation structures [5], wave filters [6], sonic shields [7], and other applications; these developments may provide new ways to achieve the aims that are difficult to realise with the traditional vibration/noise control technologies.

There has been a great deal of research on the mechanisms and properties of band gaps. The earlier investigations of PCs are commonly based on the Bragg scattering mechanism [3]. Such band gaps are called Bragg-type gaps, whose centre frequencies are governed by the Bragg condition $a = n(\lambda/2)$ ($n = 1, 2, 3, \dots$), where a is the lattice constant of the periodic system and λ is the wavelength in the host material. The Bragg condition indicates that Bragg-type gaps

are not practical for filtering waves in the low frequency range because the lattice constant must be of the same order as the relevant wavelength. In contrast, the locally resonant (LR) mechanism proposed by Liu et al. [8] makes it possible to obtain resonance-type gaps with lattice constants that are two orders of magnitude smaller than the relevant wavelength by proposing a type of LR PC, which has attracted considerable attention in this field [9–16]. The LR mechanism is mainly based on the idea of mounting periodic arrays of local resonators to a host medium. Thus, the frequency can be tuned to the desired values by varying the parameters and structures of the local resonators. In analogy with LR PCs, the idea of resonance-type band gaps has recently been attempted, both theoretically and experimentally, for rods [17–19], beams [5, 20–24], pipes [25], and plates [26–28] in vibration-control engineering.

Beams are typical structural elements of many engineering constructions and equipments. The control of wave propagation in beams is of great importance in aerospace and civil structures because the unwanted transmission of waves can lead to safety issues or environmental consequences. Based on the concept of LR PCs, some research focuses on the existence of low-frequency resonance gaps in infinite systems and the validation of gap characteristics by calculating/measuring the frequency response functions (FRFs) of finite samples [5, 20, 21]. Yu et al. investigated the flexural vibration band gaps in beams with locally resonant structures that have a single degree of freedom [5] and two degrees of freedom [20]. Liu et al. discussed the frequency range and attenuation coefficient of the locally resonant gap with different local resonators [21]. However, these studies all focused on a single band gap, which is not suitable for the reduction of vibrations in the multiple frequency ranges in engineering because the high-order modes of beams may also be involved in the vibrations. The same is true in a rotor system, in which the flexural vibration is also increased at two and four times the fundamental frequency due to angular misalignment of the coupling [29].

Recently, the coexistence of resonance-type and Bragg-type band gaps was found in LR beams [22, 23]. Liu and Hussein observed the transition state between resonance-type and Bragg-type band gaps as well as an interesting wave behaviour caused by the interplay of these two mechanisms in LR beams [22]. Xiao et al. achieved broader band gaps in a locally resonant beam with multiple arrays of damped resonators at frequencies both below and around the Bragg condition [23]. These researchers' works can derive multiple band gaps under certain circumstances, whereas the wave attenuation in a Bragg-type band gap is too small to meet the higher isolation demand. In addition, complicated structure constructions are needed to achieve a significant amount of wave attenuation in the Bragg-type band gap. Similar research can be found in the study by Wen et al., which attempted to add multiple oscillators to a unit cell of an Euler-Bernoulli beam to obtain multiple resonance-type band gaps [24]. However, the first gap these researchers derived was too narrow to mitigate vibration in the low-frequency range, and the band gaps in the frequency-multiplication ranges were not provided. Thus, their research cannot well deal with the

problem of vibration reduction within multiple frequency ranges, especially in the frequency-multiplication ranges.

The main purpose of this paper is to achieve more flexible resonance-type multiband gaps by proposing a new beam with periodically attached multioscillators. The lower initial frequency and band gaps in the frequency-multiplication ranges are expected to be obtained in the new beam, which can meet the demand of wave attenuation in multiple frequency ranges in engineering. In addition, simplified models for the corresponding edge frequencies of the band gaps are studied, which can contribute to further understanding of the LR mechanism of PCs and the realisation of composite structures with multiple band gaps. The paper is organised as follows. The exact dispersion relations for the propagation of flexural vibrations in infinite Timoshenko beams that are periodically connected with multioscillators are derived in Section 2. The analytical results for the band gaps derived from the new beam are illustrated in Section 3, and the transmission FRFs obtained using the finite element (FE) method are provided to verify the accuracy of the band gap distributions. In Section 4, simplified models are proposed to calculate the initial and terminal frequencies. In addition, the band gaps in the new beam are compared with the beam studied in [24] under different structure parameters. Finally, conclusions are presented in Section 5.

2. Analytical Models

In this section, the transfer matrix method is used to derive the exact dispersion relations for the Timoshenko beams with periodically attached multioscillators, which allows for continuity conditions at the two surface boundaries of each unit cell through the use of matrices [29, 30]. The analytical models of the beams are illustrated in Figure 1. The straight beams extend infinitely along the x axis and have an annular cross section. There are two oscillators assembled on the beam at uniformly spaced intervals, and each oscillator comprises a spring K and a mass m . The length a of the interval is called the lattice constant of the PCs. Only flexural vibrations are assumed to occur in the beam. The transverse displacement $y(x, t)$ of the Timoshenko beam satisfies the following equation of motion [5, 31]:

$$\begin{aligned} \frac{EI}{\rho S} \frac{\partial^4 y(x, t)}{\partial x^4} - \frac{1}{S} \left(1 + \frac{E}{\kappa S} \right) \frac{\partial^4 y(x, t)}{\partial x^2 \partial t^2} \\ + \frac{\partial^2 y(x, t)}{\partial t^2} + \frac{\rho I}{\kappa GS} \frac{\partial^4 y(x, t)}{\partial t^4} = 0, \end{aligned} \quad (1)$$

where E and G are the Young's modulus and shear modulus of the beam's material, respectively; ρ is the density; S is the cross-sectional area; κ is the Timoshenko shear coefficient; and I is the area moment of inertia with respect to the axis perpendicular to the beam axis. By separating out the time variable, $y(x, t)$ can be written as $y(x, t) = Y(x)e^{i\omega t}$, where ω is the circular frequency. As discussed in [5], for the n th cell,

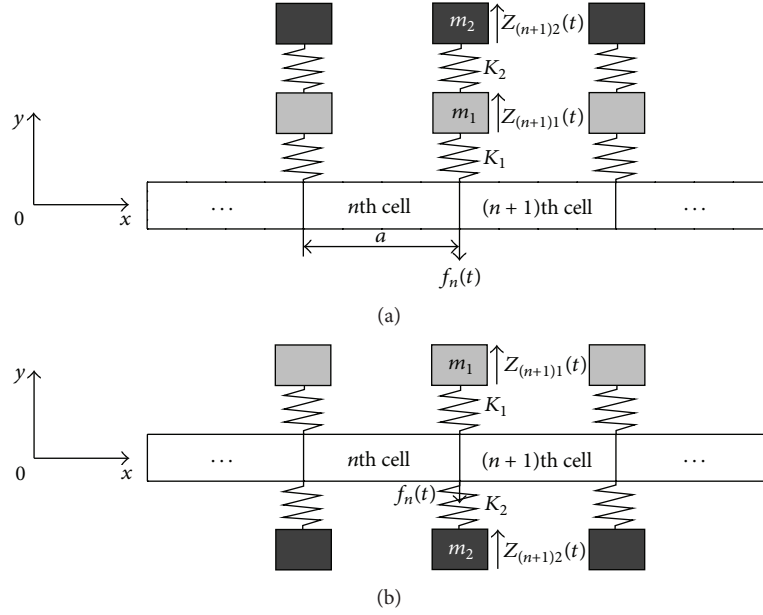


FIGURE 1: The analytical models of a Timoshenko beam with periodically attached multioscillators. (a) Model A: the oscillators are connected to each other on the same side. (b) Model B: the oscillators are distributed on different sides, a configuration which was put forward and discussed in [24].

where $x' = x - na$, and $na \leq x \leq (n+1)a$, the amplitude can be obtained by

$$Y_n(x') = A_n k_1^{-3} e^{k_1 x'} + B_n k_2^{-3} e^{k_2 x'} + C_n k_3^{-3} e^{k_3 x'} + D_n k_4^{-3} e^{k_4 x'}, \quad (2)$$

with

$$k_j = (-1)^{[j/2]} \sqrt{\frac{\alpha + (-1)^j \sqrt{\alpha^2 + 4\beta}}{2}}, \quad \text{for } j = 1, 2, 3, 4, \quad (3)$$

where $\alpha = -\rho\omega^2/E - \rho\omega^2/\kappa G$; $\beta = -\rho\omega^2/EI - \rho^2\omega^4/E\kappa G$, and $[j/2]$ is the largest integer that is less than $j/2$.

For Model A, which is shown in Figure 1(a), the dynamic equations of the two oscillators connected between the n th and $(n+1)$ th cell can be derived as

$$\begin{aligned} m_1 \ddot{Z}_{(n+1)1} + K_1 (Z_{(n+1)1} - y_{n+1}(0, t)) \\ + K_2 (Z_{(n+1)1} - Z_{(n+1)2}) = 0, \\ m_2 \ddot{Z}_{(n+1)2} + K_2 (Z_{(n+1)2} - Z_{(n+1)1}) = 0, \end{aligned} \quad (4)$$

where $Z_{(n+1)1} = V_{(n+1)1} e^{i\omega t}$ and $Z_{(n+1)2} = V_{(n+1)2} e^{i\omega t}$ are the displacements of the two oscillators of the $(n+1)$ th cell at the centre of gravity. The absolute values of $V_{(n+1)1}$ and $V_{(n+1)2}$ are the vibration amplitudes of the two oscillators of the $(n+1)$ th unit cell. From (4), the relationship between $V_{(n+1)1}$ and $Y_{(n+1)}(0)$ is

$$V_{(n+1)1} = \frac{K_1 Y_{n+1}(0)}{(K_1 - m_1 \omega^2 - K_2 m_2 \omega^2 / (K_2 - m_2 \omega^2))}. \quad (5)$$

The interactive force between the first oscillator and the beam, F_{n+1} , at $x' = (n+1)a$ is

$$\begin{aligned} F_{n+1} &= K_1 [Y_{n+1}(0) - V_{(n+1)A}] \\ &= \frac{K_1 Y_{n+1}(0) [m_1 \omega^2 + K_2 m_2 \omega^2 / (K_2 - m_2 \omega^2)]}{[m_1 \omega^2 + K_2 m_2 \omega^2 / (K_2 - m_2 \omega^2) - K_1]}. \end{aligned} \quad (6)$$

For the case of Model B studied in [24], the dynamic equation for the two unconnected oscillators at the interface shown in Figure 1(b) can be derived as [24]

$$m_i \ddot{Z}_{(n+1)i} + K_i (Z_{(n+1)i} - y_{n+1}(0, t)) = 0, \quad i = 1, 2. \quad (7)$$

The solution is

$$V_{(n+1)i} = \frac{K_i}{K_i - m_i \omega^2} Y_{n+1}(0), \quad i = 1, 2. \quad (8)$$

From (8), the interactive force between the oscillators and the beam, F_{n+1} , at $x' = (n+1)a$ is

$$\begin{aligned} F_{n+1} &= \sum K_i [Y_{n+1}(0) - V_{(n+1)i}] \\ &= \sum K_i \left(1 - \frac{K_i}{K_i - m_i \omega^2} \right) Y_{n+1}(0), \quad i = 1, 2. \end{aligned} \quad (9)$$

According to the continuity of the displacement, slope, bending moment, and shear force at the interface between the n th and $(n+1)$ th unit cell, $x' = na$,

$$\begin{aligned} Y_n(a) &= Y_{n+1}(0), \\ Y'_n(a) &= Y'_{n+1}(0), \\ EI Y''_n(a) &= EI Y''_{n+1}(0), \\ EI Y'''_n(a) &= EI Y'''_{n+1}(0) - F_{n+1}. \end{aligned} \quad (10)$$

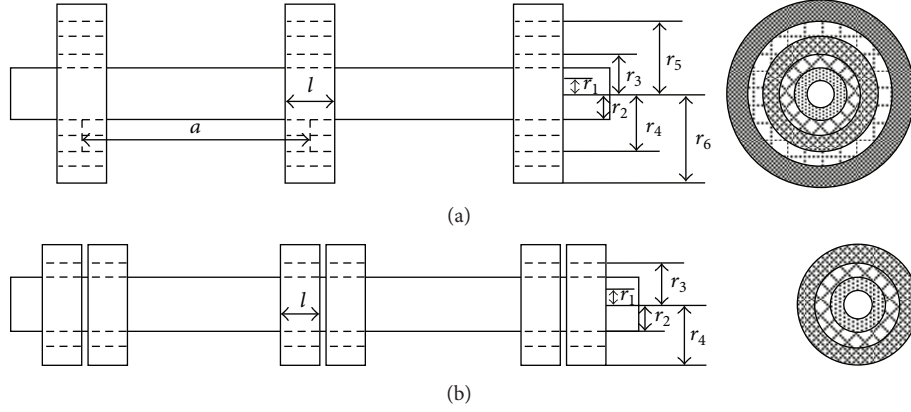


FIGURE 2: The sketch of a Timoshenko beam with periodically attached multioscillators. (a) Model A, (b) Model B.

By extracting the arbitrary coefficients from (10), $\Phi_n = [A_n \ B_n \ C_n \ D_n]^T$, these equations can be written in matrix form as follows

$$\mathbf{M}_n \Phi_n = \mathbf{N}_{n+1} \Phi_{n+1}, \quad (11)$$

where

$$\mathbf{M}_n = \begin{bmatrix} k_1^{-3} e^{k_1 a} & k_2^{-3} e^{k_2 a} & k_3^{-3} e^{k_3 a} & k_4^{-3} e^{k_4 a} \\ k_1^{-2} e^{k_1 a} & k_2^{-2} e^{k_2 a} & k_3^{-2} e^{k_3 a} & k_4^{-2} e^{k_4 a} \\ k_1^{-1} e^{k_1 a} & k_2^{-1} e^{k_2 a} & k_3^{-1} e^{k_3 a} & k_4^{-1} e^{k_4 a} \\ e^{k_1 a} & e^{k_2 a} & e^{k_3 a} & e^{k_4 a} \end{bmatrix},$$

\mathbf{N}_{n+1}

$$= \begin{bmatrix} k_1^{-3} & k_2^{-3} & k_3^{-3} & k_4^{-3} \\ k_1^{-2} & k_2^{-2} & k_3^{-2} & k_4^{-2} \\ k_1^{-1} & k_2^{-1} & k_3^{-1} & k_4^{-1} \\ 1 - \frac{F_{n+1} k_1^{-3}}{EI} & 1 - \frac{F_{n+1} k_2^{-3}}{EI} & 1 - \frac{F_{n+1} k_3^{-3}}{EI} & 1 - \frac{F_{n+1} k_4^{-3}}{EI} \end{bmatrix}. \quad (12)$$

Due to the periodicity of the structure, the Bloch theorem states that

$$\Phi_{n+1} = e^{iqa} \Phi_n, \quad (13)$$

where q is wave vector in the x direction. The problem can be transformed into an eigenvalue matrix equation:

$$|\mathbf{T} - e^{iqa} \mathbf{I}| = 0, \quad (14)$$

where $\mathbf{T} = \mathbf{N}_{n+1}^{-1} \mathbf{M}_n$ and \mathbf{I} is a 4×4 unit matrix.

The dispersion relation between the wave vector q and the frequency ω can therefore be obtained. For any ω , if q is a real number, ω is in the pass band. If q has an imaginary part, the corresponding wave is damped in that region, and the imaginary part of q can be used to describe the attenuation properties in the band gaps.

TABLE 1: Material parameters.

Material	Density (kg/m ³)	Young's Modulus E (Pa)	Shear Modulus G (Pa)	Poisson ratio σ
Rubber	1300	7.7×10^5	2.6×10^5	0.48
Al	2600	7.0×10^{10}	2.7×10^{10}	0.3
Cu	8950	1.646×10^{11}	7.53×10^{10}	0.093
Steel	7780	2.106×10^{11}	8.1×10^{10}	0.3

3. Numerical Simulation and Comparison

Figure 2 shows two simulation structures of the beam with oscillators based on Model A and Model B, respectively. Both beams are constructed using an aluminium tube, and the oscillators are composed of soft rubber rings and metal rings. As shown in Figure 2(a), the multioscillators in Model A are structures composed of four connected rings in each unit cell, whereas the periodically attached multioscillators in Model B presented in Figure 2(b) are two adjacent structures that are each composed of a rubber ring and a metal ring. The inner and outer radii of the tube are $r_1 = 0.007$ m and $r_2 = 0.01$ m, respectively. The lattice constant is $a = 0.075$ m, and the length of all the rings is $l = 0.01$ m. The outer radius of the first rubber ring, which is in contact with the tube, is $r_3 = 0.015$ m. The outer radius of the first metal ring, which is in contact with the first rubber ring, is $r_4 = 0.0195$ m. The radii of the second rubber ring and the metal ring in Figure 2(a) (r_5 and r_6) will be determined in the following

All of the material parameters used in the calculations are listed in the Table 1. As discussed in [32], the shear coefficient of the Timoshenko beam can be determined by

$$\kappa = \frac{6 + 12\sigma + 6\sigma^2}{7 + 12\sigma + 4\sigma^2}, \quad (15)$$

where σ denotes the Poisson ratio.

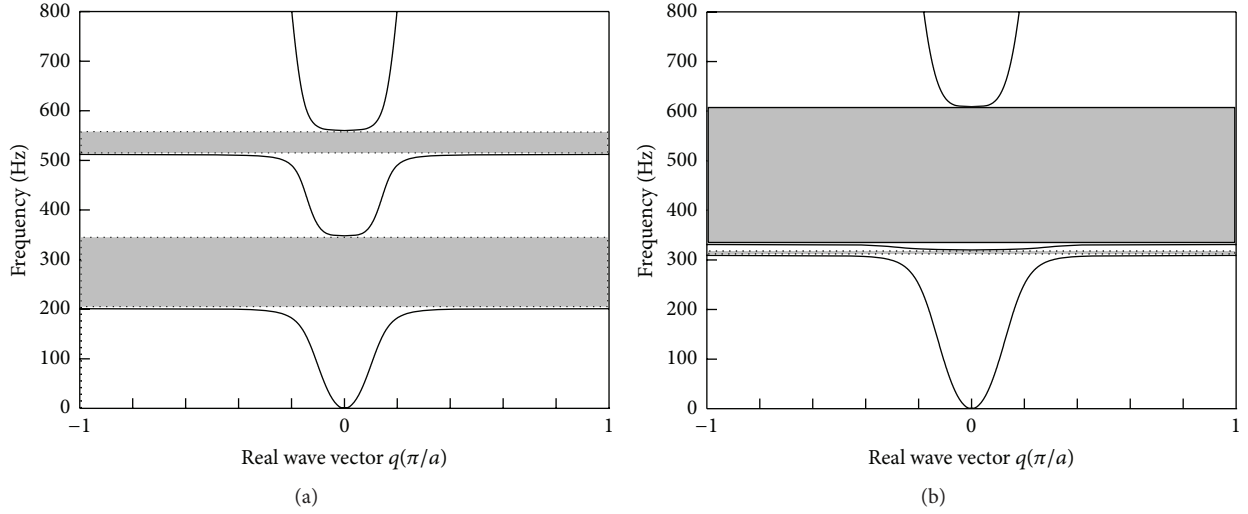


FIGURE 3: The band structure of the infinite Timoshenko beam with periodically attached multioscillators. (a) Real wave vector of Model A. (b) Real wave vector of Model B.

The radial stiffness of the rubber ring can be calculated using [33]

$$K = \frac{\pi (5 + 3.29H^2) Gl}{\ln(r_2/r_1)}, \quad (16)$$

where $H = 1/(r_1 + r_2) \ln(r_1/r_2)$ is the shape coefficient.

For comparison, the structure parameters for Model B are taken from [24]. The stiffness and mass of the LR structures in Model A and Model B are the same, namely, $m_1 = 0.0437$ kg, $m_2 = 0.0379$ kg, and $K_1 = K_2 = 1.65 \times 10^5$ N/m. The radii of the second rings are set to $r_5 = 0.02688$ m and $r_6 = 0.02963$ m.

The band structures of both models are shown in Figure 3. The complete band gaps are shaded. In both models, two complete band gaps are found between 0 and 800 Hz. The band gap characteristics of Model B based on the Timoshenko beam theory are verified with the results derived in [24]. Compared with the beam with only one oscillator in a unit cell in [5], although the initial frequencies of the first band gaps are both 309 Hz, the total width of the first two band gaps in the Model B is increased from 170.3 Hz to 297.1 Hz. However, the positions of the first two band gaps are too close and are not suitable for vibration reduction within multiple frequency ranges, especially if the frequency ranges in which vibration must be reduced have large intervals.

Figure 3(a), obtained using Model A, shows two widely separated band gaps that are not obtained in Model B. The initial frequency of the first gap in Model A is decreased to 201.4 Hz. Note that the centre frequency of the second band gap (511.8–560.9 Hz) is approximated two times the centre frequency of the first gap (201.4–348.4 Hz); that is, a frequency-multiplication relationship between the two resonance-type gap can be achieved. The “frequency-multiplication relationship” mentioned here can be explained as follows: the central frequency of the band gaps is close to the frequency $f_N = N \times f_1$ (N could be 1, 2, 3, ...), where

the fundamental frequency f_1 is the central frequency of the first band gap. Thus, the flexural vibrations at one and two times the fundamental frequency can be well reduced, a phenomenon that can be employed to address a case such as the above-mentioned angular misalignment of the coupling in a rotor system. In addition, the first band gap in Model A is wider than the second band gap, which helps to flexibly reduce vibrations of the beam at low frequencies.

The existence of the band gaps calculated from the infinite system can be verified by the transmission property derived from a corresponding finite system because PCs with a sufficient number of unit cells can provide a large wave attenuation in the corresponding band gap range [11]. The FRF, which represents the relationship between the wave response and the corresponding frequencies, has been used to describe vibration gaps effectively. Therefore, the finite system of Model A is created in Abaqus to calculate the FRF. The mesh model for the FE method is illustrated in Figure 4(a), which has the same geometry in the unit cell as the model in Figure 2(a). Based the analysis of different numbers of unit cells in the structure [11], eight unit cells used in an FE simulation can achieve a sufficient accuracy for approximating the results of the infinite system. Therefore, the length of the beam is 0.6 m in Figure 4(a). To guarantee the free vibration of the beam, there are no boundary constraints at the ends of the beam. The acceleration is induced at the left end of the beam in the y direction, and the corresponding acceleration is extracted at the opposite end. The frequency responses are illustrated as solid lines in Figure 4(b).

Note the two sharp drops below the 0 dB line (dashed line) in the Figure 4(b), which indicate the ranges of the band gaps. Compared with the response outside the band gaps, the average response attenuation of the two band gaps is approximately 40 dB. The ranges of the first two gaps calculated using the FE method are similar to those of the gaps shown in Figure 3(a), which are obtained from the

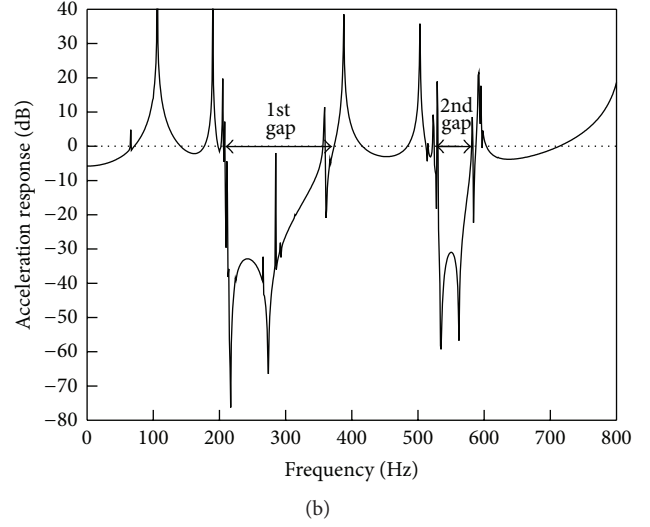
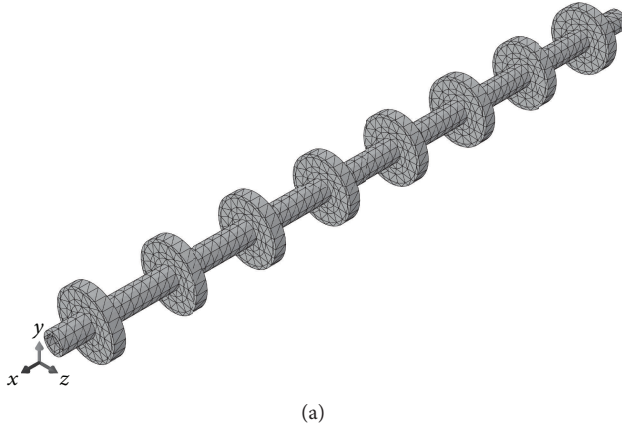


FIGURE 4: (a) The calculation model for the FE method. (b) The corresponding calculated FRF.

infinite structure. It can be concluded that the previous analysis is accurate, and using LR structures with equivalent parameters, Model A has better band gaps for vibration reduction in the frequency-multiplication ranges than does Model B. Considering the advantages of each model, an LR PC beam with the desired band gap properties can be obtained by choosing the most appropriate plan.

4. Simplified Models for the Edge Frequencies of Band Gaps

In this section, the corresponding simplified models for the initial and terminal frequencies of the band gaps for Model A are studied. The simplified models for Model B have been discussed previously in [24].

4.1. Initial Frequency Model. The initial frequency of the first band gap in a typical LR PC is determined by the resonance frequency of the oscillator in the same direction. In this resonance mode, the oscillators vibrate in specific directions, and the phases of the oscillator vibrations in adjacent unit cells are reversed to keep the dynamic balance [4, 24]. Thus, the simplified model for the initial frequencies of the two oscillators can be formed as shown in Figure 5.

The equations of motion for the model are as follows:

$$\begin{aligned} m_1 \ddot{u}_1 + K_1 u_1 + K_2 (u_1 - u_2) &= 0, \\ m_2 \ddot{u}_2 + K_2 (u_2 - u_1) &= 0, \end{aligned} \quad (17)$$

where u_1 and u_2 represent the displacements of the respective oscillator.

The natural angular frequency ω_{in} satisfies the equation

$$\det [\mathbf{k} - \omega_{in}^2 \mathbf{m}] = 0, \quad (18)$$

where $\mathbf{k} = \begin{bmatrix} K_1 + K_2 & -K_2 \\ -K_2 & K_2 \end{bmatrix}$, $\mathbf{m} = \begin{bmatrix} m_1 & 0 \\ 0 & m_2 \end{bmatrix}$.

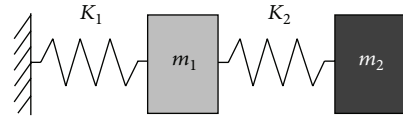


FIGURE 5: The simplified model for the initial frequencies of band gaps.

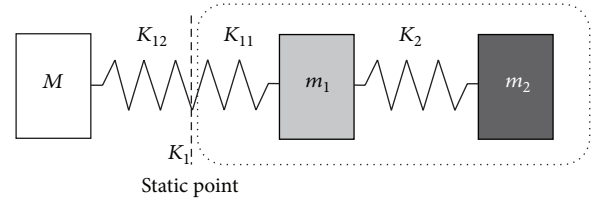


FIGURE 6: The simplified model for the terminal frequencies of the band gaps.

Thus,

$$\begin{aligned} \omega_{i1,2}^2 &= \frac{K_1 m_2 + K_2 m_1 + K_2 m_2}{2m_1 m_2} \\ &\pm \frac{\sqrt{(K_1 m_2 + K_2 m_1 + K_2 m_2)^2 - 4K_1 K_2 m_1 m_2}}{2m_1 m_2} \end{aligned} \quad (19)$$

can be obtained, and the initial frequencies of the first two band gaps are $f_{i1,2} = \sqrt{\omega_{i1,2}}/2\pi$.

4.2. Terminal Frequency Model. All of the oscillation phases of the unit cells are in the same direction at the terminal frequency of the band gap. The dynamic balance is given by the antiphases between the LR structures and the matrix [4, 24]. The matrix mentioned in [4, 24] is the beam in this paper by analogy. As illustrated in Figure 6, the simplified model for

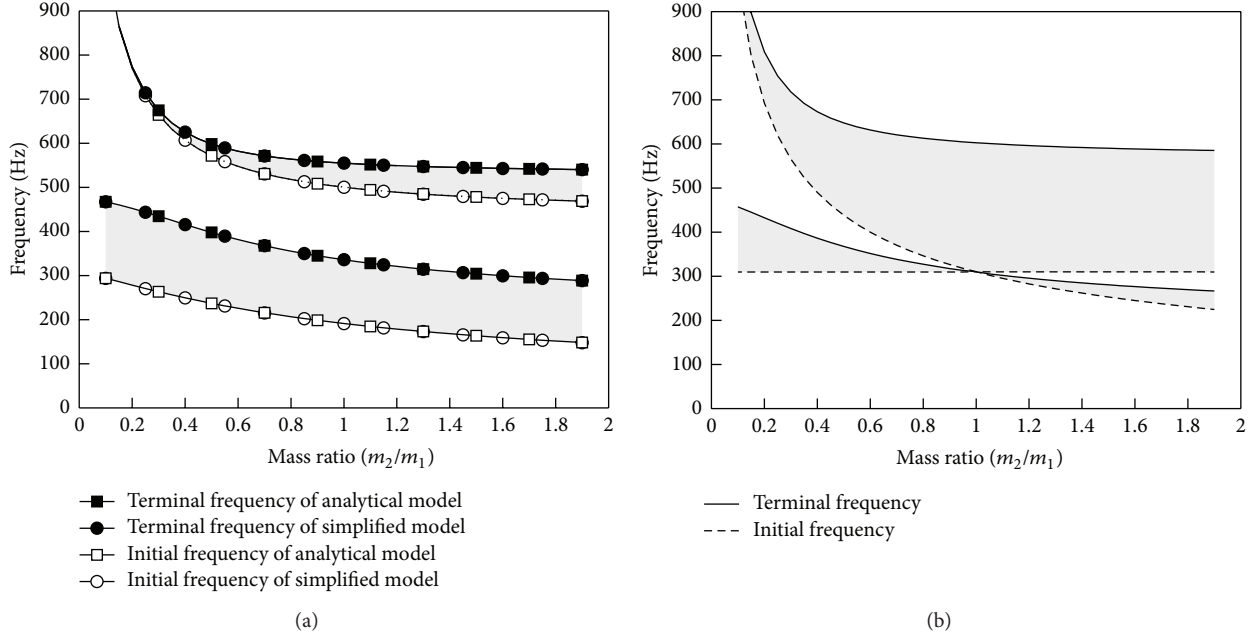


FIGURE 7: Variation of the band gaps as a function of the oscillators' mass ratio and verification of the simplified models. (a) Model A, (b) Model B. ($m_1 = 0.0437$ kg, $M = 0.0312$ kg, and $K_1 = K_2 = 1.65 \times 10^5$ N/m).

the terminal frequencies comprises the beam mass M and the oscillators in the unit cell. There is a static point between the beam and the connected oscillators that divides the model into two parts that have the same natural frequencies. At the static point, the spring K_1 can be considered a series connection of two springs K_{11} and K_{12} , which are related by the following equation:

$$\frac{1}{K_1} = \frac{1}{K_{11}} + \frac{1}{K_{12}}. \quad (20)$$

$$\omega_{t1,2}^2 = \frac{MK_1m_2 + MK_2m_1 + MK_2m_2 + K_1m_1m_2}{2Mm_1m_2} \pm \frac{\sqrt{(MK_1m_2 + MK_2m_1 + MK_2m_2 - K_1m_1m_2)^2 + 4MK_1m_1m_2(K_1m_2 - MK_2)}}{2Mm_1m_2}, \quad (22)$$

and the terminal frequencies of the first two band gaps are $f_{t1,2} = \sqrt{\omega_{t1,2}}/2\pi$.

Figures 7, 8, and 9 illustrate the dependence of the band gaps on the oscillators' mass ratio, the oscillators' stiffness ratio, and the beam's mass, respectively. In addition, for Model A, the calculations of the initial and terminal frequencies of the first two band gaps using both the analytical and simplified models are presented to verify the accuracy of the deduced formulae. The shadow regions indicate the band

The components to the right of the static point (dashed box) can be observed as a single unit. The natural angular frequency ω_{tn} is described by (17) to (19), where K_1 is replaced by K_{11} .

Because the resonances of the matrix and the connected oscillators are at the same frequency,

$$\frac{K_{12}}{M} = \omega_{tn}^2. \quad (21)$$

Thus, the relation between K_{11} and ω_{tn} can be extracted and combined with the previous discussion in Section 4.1. Therefore,

gaps, and the details of the data are illustrated in the top right corner of each figure.

Figures 7(a), 8(a), and 9(a) show that the frequencies of the band gaps obtained using the simplified models and the analytical model are in good agreement. These results prove the accuracy and validity of the methods proposed in this paper. The beams with periodically attached multioscillators have similar resonance modes to those of typical LR PCs at the boundary frequencies of the band gaps. This result reveals

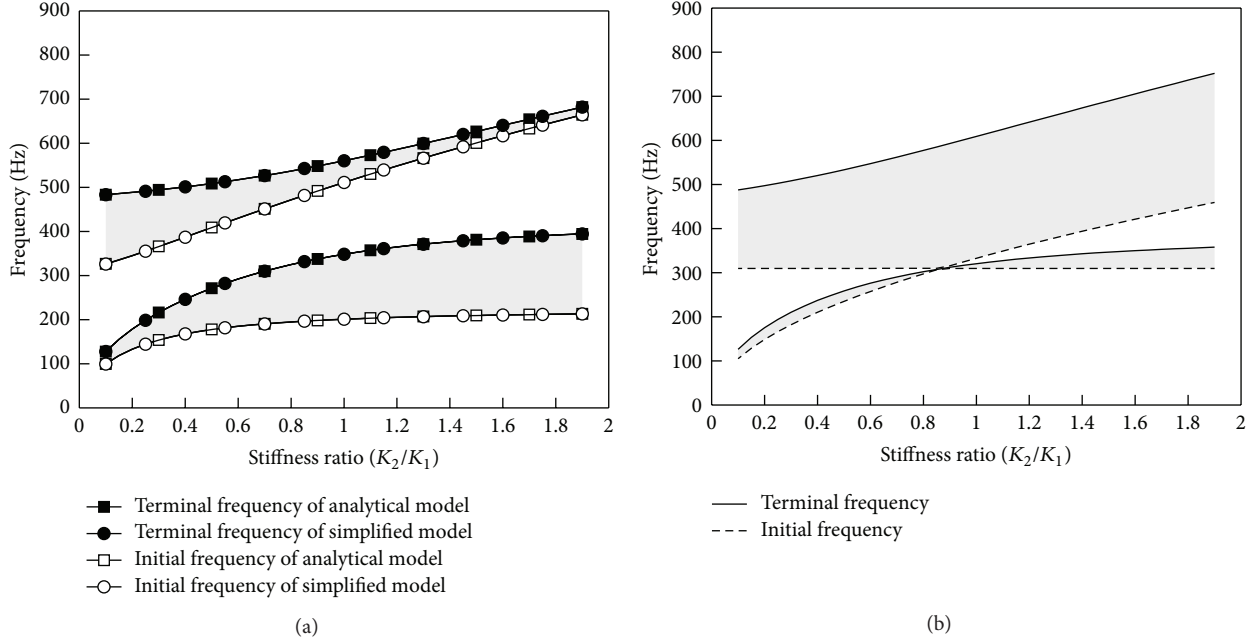


FIGURE 8: Variation of the band gaps as a function of the oscillators' stiffness ratio and verification of the simplified models. (a) Model A, (b) Model B. ($m_1 = 0.0437$ kg, $m_2 = 0.0379$ kg, $M = 0.0312$ kg, and $K_1 = 1.65 \times 10^5$ N/m).

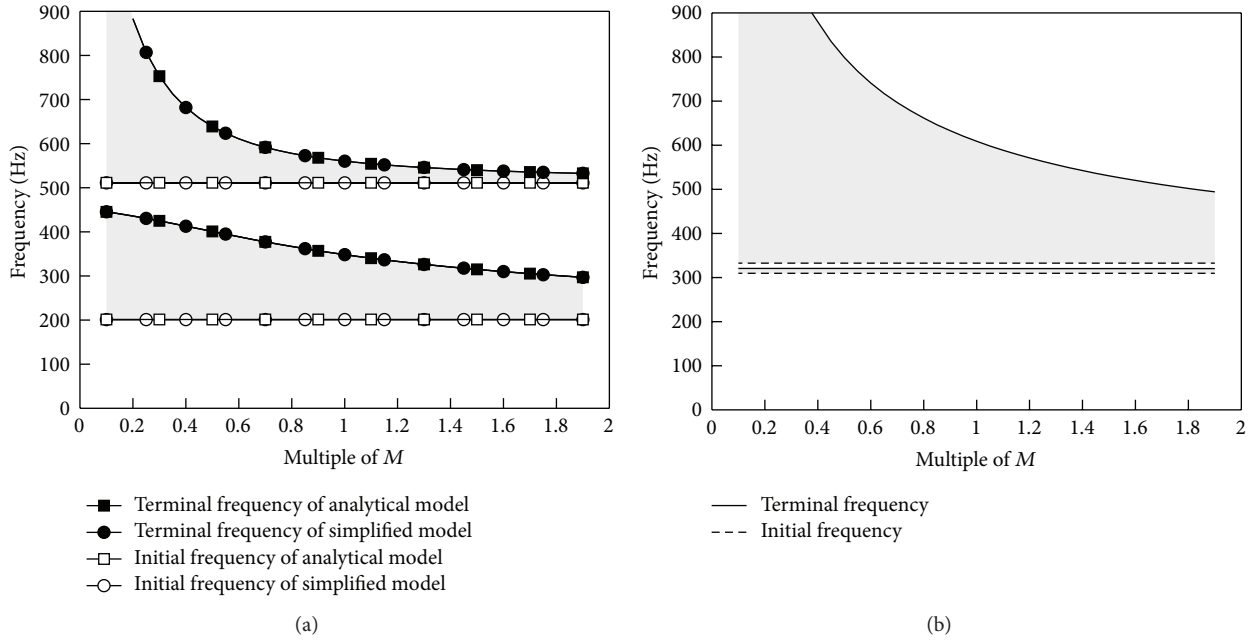


FIGURE 9: Variation of the band gaps as a function of the beam's mass and verification of the simplified models. (a) Model A, (b) Model B. ($m_1 = 0.0437$ kg, $m_2 = 0.0379$ kg, $M = 0.0312$ kg, and $K_1 = K_2 = 1.65 \times 10^5$ N/m).

the characteristics of the LR mechanism, which is helpful in the construction of new devices with LR band gaps.

By comparing the (a) subfigure with the (b) subfigure in Figures 7–9, it can be seen that the variation tendencies of Model A are similar to those of Model B. With the increase of the oscillators' mass as well as the beam's mass or with the reduction of the oscillators' stiffness, the frequencies of

the band gaps are decreased. However, there is usually a distance between the first two band gaps in Model A, and the band gaps that are widely separated can be obtained without large differences in the parameters of the oscillators. Thus, Model A has better regulation and control abilities in practical engineering. In addition, with the same material parameters, Model A clearly always has a lower initial

frequency and a wider first band gap than Model B and is able to provide a larger range of vibration reduction at low frequencies. To achieve lower frequencies, Model B should use a larger mass or a smaller stiffness, which is uneconomic in most engineering. In addition, although the total width of the gaps is larger, a narrow first band gap is almost inevitable in Model B. Furthermore, the band gaps with a frequency-multiplication relationship cannot be well derived in Model B; thus, this model is not appropriate for vibration damping or noise reduction in the frequency-multiplication ranges. In general, Model A has specific abilities and can be more reasonably and feasibly applied to practical structures because of the advantages of lower frequencies, frequency-multiplication relationships, and material costs.

5. Conclusions

In this paper, a new Timoshenko beam structure with periodically attached multioscillators is proposed to obtain band gaps in the frequency-multiplication ranges based on the LR mechanism of PCs. Explicit matrix formulations are derived for the calculation of wave band structures of the new beam by using the transfer matrix method. The gap characteristics of the beam are confirmed by calculating the FRF of the corresponding finite structure. The numerical calculations of the band structures and the analysis of the model parameters demonstrate that the beams with periodically attached multioscillators have more abundant gap characteristics than those with only one oscillator in a unit cell. By using common materials and an uncomplicated beam structure, multiple resonance-type band gaps with large wave-attenuation and frequency-multiplication ranges, together with the wider and lower first band gap, are derived in the new beam; this result was not illustrated in any of the previous studies on LR PC beams. In addition, simplified models are proposed to deduce accurate estimation formulae for the initial and terminal frequencies of the band gaps in the new beam. The simplified models will also contribute to enhanced understanding of the LR mechanism of PCs and will facilitate the analysis of similar structures.

The research findings presented in this paper provide suggestions for future studies of small-size PCs with low frequencies and multiple resonance-type band gaps. Moreover, the results can be employed to create new devices that reduce vibration and mitigate noise in the frequency-multiplication ranges for aerospace and civil structures.

Acknowledgment

This work is supported by the National Nature Science Foundation of China under Grant nos. 51079127, 51179171, and 51279180.

References

- [1] E. I. Rivin, *Passive Vibration Isolation*, ASME Press, New York, NY, USA, 2003.

- [2] M. M. Sigalas and E. N. Economou, "Elastic and acoustic wave band structure," *Journal of Sound and Vibration*, vol. 158, no. 2, pp. 377–382, 1992.
- [3] M. S. Kushwaha, P. Halevi, L. Dobrzynski, and B. Djafari-Rouhani, "Acoustic band structure of periodic elastic composites," *Physical Review Letters*, vol. 71, no. 13, pp. 2022–2025, 1993.
- [4] X. S. Wen, J. H. Wen, D. L. Yu et al., *Phononic Crystals*, National Defense, Industry Press, Beijing, China, 2009.
- [5] D. Yu, Y. Liu, G. Wang, H. Zhao, and J. Qiu, "Flexural vibration band gaps in Timoshenko beams with locally resonant structures," *Journal of Applied Physics*, vol. 100, no. 12, Article ID 124901, 2006.
- [6] J. H. Sun, C. W. Lan, C. Y. Kuo, and T. T. Wu, "A ZnO/silicon Lamb wave filter using phononic crystals," in *Proceedings of the IEEE International Frequency Control Symposium*, pp. 1–4, Baltimore, Md, USA, May 2012.
- [7] K. M. Ho, C. K. Cheng, Z. Yang, X. X. Zhang, and P. Sheng, "Broadband locally resonant sonic shields," *Applied Physics Letters*, vol. 83, no. 26, pp. 5566–5568, 2003.
- [8] Z. Liu, X. Zhang, Y. Mao et al., "Locally resonant sonic materials," *Science*, vol. 289, no. 5485, pp. 1734–1736, 2000.
- [9] C. Goffaux, J. Sánchez-Dehesa, A. L. Yeyati et al., "Evidence of Fano-like interference phenomena in locally resonant materials," *Physical Review Letters*, vol. 88, no. 22, Article ID 225502, 4 pages, 2002.
- [10] P. Sheng, X. X. Zhang, Z. Liu, and C. T. Chan, "Locally resonant sonic materials," *Physica B*, vol. 338, no. 1–4, pp. 201–205, 2003.
- [11] J. S. Jensen, "Phononic band gaps and vibrations in one- and two-dimensional mass-spring structures," *Journal of Sound and Vibration*, vol. 266, no. 5, pp. 1053–1078, 2003.
- [12] M. Hirsekorn, "Small-size sonic crystals with strong attenuation bands in the audible frequency range," *Applied Physics Letters*, vol. 84, no. 17, pp. 3364–3366, 2004.
- [13] G. Wang, D. Yu, J. Wen, Y. Liu, and X. Wen, "One-dimensional phononic crystals with locally resonant structures," *Physics Letters A*, vol. 327, no. 5–6, pp. 512–521, 2004.
- [14] Z. Liu, C. T. Chan, and P. Sheng, "Analytic model of phononic crystals with local resonances," *Physical Review B*, vol. 71, no. 1, Article ID 014103, 8 pages, 2005.
- [15] H. H. Huang and C. T. Sun, "Wave attenuation mechanism in an acoustic metamaterial with negative effective mass density," *New Journal of Physics*, vol. 11, Article ID 013003, 2009.
- [16] H. H. Huang, C. T. Sun, and G. L. Huang, "On the negative effective mass density in acoustic metamaterials," *International Journal of Engineering Science*, vol. 47, no. 4, pp. 610–617, 2009.
- [17] G. Wang, X. Wen, J. Wen, and Y. Liu, "Quasi-one-dimensional periodic structure with locally resonant band gap," *Journal of Applied Mechanics*, vol. 73, no. 1, pp. 167–170, 2006.
- [18] D. Yu, Y. Liu, G. Wang, L. Cai, and J. Qiu, "Low frequency torsional vibration gaps in the shaft with locally resonant structures," *Physics Letters A*, vol. 348, no. 3–6, pp. 410–415, 2006.
- [19] Y. Xiao, J. H. Wen, and X. S. Wen, "Longitudinal wave band gaps in metamaterial-based elastic rods containing multi-degree-of-freedom resonators," *New Journal of Physics*, vol. 14, no. 3, Article ID 033042, 2012.
- [20] D. Yu, Y. Liu, H. Zhao, G. Wang, and J. Qiu, "Flexural vibration band gaps in Euler-Bernoulli beams with locally resonant structures with two degrees of freedom," *Physical Review B*, vol. 73, no. 6, pp. 1–5, 2006.

- [21] Y. Liu, D. Yu, L. Li, H. Zhao, J. Wen, and X. Wen, "Design guidelines for flexural wave attenuation of slender beams with local resonators," *Physics Letters A*, vol. 362, no. 5-6, pp. 344–347, 2007.
- [22] L. Liu and M. I. Hussein, "Wave motion in periodic flexural beams and characterization of the transition between Bragg scattering and local resonance," *Journal of Applied Mechanics*, vol. 79, no. 1, Article ID 011003, 17 pages, 2012.
- [23] Y. Xiao, J. H. Wen, and X. S. Wen, "Broadband locally resonant beams containing multiple periodic arrays of attached resonators," *Physics Letters A*, vol. 376, no. 16, pp. 1384–1390, 2012.
- [24] Q. H. Wen, S. G. Zuo, and H. Wei, "Locally resonant elastic wave band gaps in flexural vibration of multi-oscillators beam," *Acta Physica Sinica*, vol. 61, no. 3, Article ID 034301, 2012.
- [25] D. Yu, J. Wen, H. Zhao, Y. Liu, and X. Wen, "Vibration reduction by using the idea of phononic crystals in a pipe-conveying fluid," *Journal of Sound and Vibration*, vol. 318, no. 1-2, pp. 193–205, 2008.
- [26] M. Oudich, Y. Li, B. M. Assouar, and Z. Hou, "A sonic band gap based on the locally resonant phononic plates with stubs," *New Journal of Physics*, vol. 12, Article ID 083049, 2010.
- [27] J. C. Hsu, "Local resonances-induced low-frequency band gaps in two-dimensional phononic crystal slabs with periodic stepped resonators," *Journal of Physics D*, vol. 44, no. 5, Article ID 055401, 2011.
- [28] Y. Xiao, J. H. Wen, and X. S. Wen, "Flexural wave band gaps in locally resonant thin plates with periodically attached spring-mass resonators," *Journal of Physics D*, vol. 45, no. 19, Article ID 195401, 2012.
- [29] W. T. Thomson, "Transmission of elastic waves through a stratified solid medium," *Journal of Applied Physics*, vol. 21, no. 2, pp. 89–93, 1950.
- [30] R. Esquivel-Sirvent and G. H. Coccoletzi, "Band structure for the propagation of elastic waves in superlattices," *Journal of the Acoustical Society of America*, vol. 95, no. 1, pp. 86–90, 1994.
- [31] R. A. Méndez-Sánchez, A. Morales, and J. Flores, "Experimental check on the accuracy of Timoshenko's beam theory," *Journal of Sound and Vibration*, vol. 279, no. 1-2, pp. 508–512, 2005.
- [32] T. Kaneko, "On Timoshenko's correction for shear in vibrating beams," *Journal of Physics D*, vol. 8, no. 16, pp. 1927–1936, 1975.
- [33] C. S. Zhao and S. J. Zhu, "Study on the static stiffness characteristics of rubber-metal ring," *China Mechanical Engineering*, vol. 15, no. 11, pp. 962–964, 2004.

Research Article

Warped Wigner-Hough Transform for Defect Reflection Enhancement in Ultrasonic Guided Wave Monitoring

**Luca De Marchi,¹ Emanuele Baravelli,¹ Giampaolo Cera,¹
Nicolò Speciale,¹ and Alessandro Marzani²**

¹ Department of Electronics, Information and Computer Systems (DEIS), University of Bologna,
40136 Bologna, Italy

² Department of Civil, Environmental and Materials Engineering (DICAM), University of Bologna,
40136 Bologna, Italy

Correspondence should be addressed to Alessandro Marzani, alessandro.marzani@unibo.it

Received 27 August 2012; Revised 19 October 2012; Accepted 20 October 2012

Academic Editor: Zhongqing Su

Copyright © 2012 Luca De Marchi et al. This is an open access article distributed under the Creative Commons Attribution License, which permits unrestricted use, distribution, and reproduction in any medium, provided the original work is properly cited.

To improve the defect detectability of Lamb wave inspection systems, the application of nonlinear signal processing was investigated. The approach is based on a Warped Frequency Transform (WFT) to compensate the dispersive behavior of ultrasonic guided waves, followed by a Wigner-Ville time-frequency analysis and the Hough Transform to further improve localization accuracy. As a result, an automatic detection procedure to locate defect-induced reflections was demonstrated and successfully tested by analyzing numerically simulated Lamb waves propagating in an aluminum plate. The proposed method is suitable for defect detection and can be easily implemented for real-world structural health monitoring applications.

1. Introduction

In recent years, ultrasonic guided waves (GWs) have received a great deal of attention among nondestructive tests community due mainly to the ability to travel long distances without substantial attenuation and to employ multimode/-frequency examination for defect classification and sizing. Among the various techniques based on GWs, the detection of defects in plates-like structures by means of Lamb waves has been, and is still, widely investigated [1–6] due to the variety of potential applications. Since the propagation characteristics are directly related to both the inherent structure and mechanical properties of the medium, the dispersiveness of GWs can reveal important information for structural

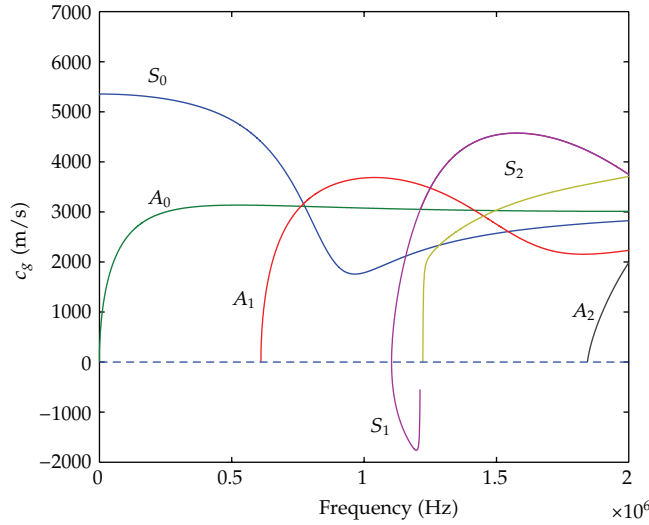


Figure 1: Group velocity dispersion curves for the Lamb waves propagating in a 2.54 mm thick aluminum plate (Young modulus $E = 69$ GPa, Poisson's coefficient $\nu = 0.33$, and density $\rho = 2700$ kg/m³).

health monitoring purposes. Unfortunately, several different modes appear simultaneously in the signal. These modes overlap in both time and frequency domains, and simple Fourier analysis techniques are not able to separate them.

Thus, identification of Lamb modes is a challenging step in the process of damage detection. However, recent works in the area of time-frequency representations (TFRs) [7, 8] show great potential for applications in nondestructive evaluation and material characterization. Specifically, TFRs can provide an effective tool for the interpretation of GWs, whose multimodal and dispersive nature make them an extremely complicated class of ultrasonic signals.

This work proposes a time-frequency (TF) energy density function approach that makes use of known dispersion characteristics for a propagating wave mode in order to compensate for the effect of dispersion and locate defects in plate-like structures. Our approach will be illustrated through a relevant case study, in which defects are to be located on an aluminum plate where Lamb waves are excited.

2. Numerical Simulation of Lamb Wave Propagation

Let us consider an aluminum plate of thickness is $h = 2.54$ mm, Young's modulus $E = 69$ GPa, and Poisson's ratio $\nu = 0.33$. The proposed processing requires the computation of the group velocity dispersion curves for the plate. For such task, today several formulations and tools are available. For instance, in uniform waveguides the group velocity $c_g(f)$ can be estimated by means of analytical-based formulations [9], semianalytical finite element (SAFE) simulations [10], and by using standard finite element codes [11]. Recent developments allow the computation of the dispersion curves also in the case of irregular waveguides [12]. The results shown in Figure 1 were obtained by a using free-SAFE-based tool that can be downloaded at <http://www.guiguw.com/> [10].

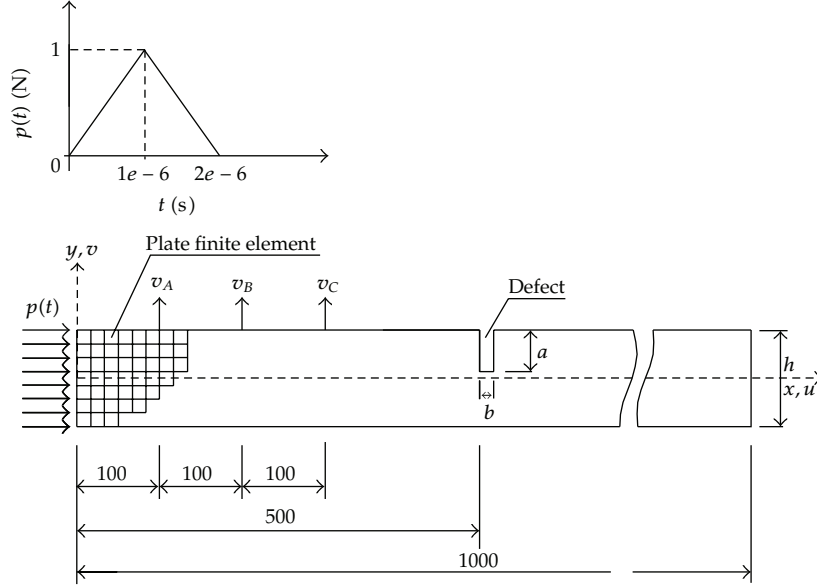


Figure 2: Schematic representation of the damaged aluminum plate used in the time-transient FEM simulations (plate dimensions are in mm). The spatial distribution and time-amplitude shape of the actuation pulse is also shown.

As a second step, time waveforms related to Lamb waves propagating in the aluminum plate were obtained numerically by means of dedicated Finite Element (FEM) simulations using Abaqus explicit [13]. Thanks to the Lamb problem symmetry, a x - y plane strain condition was assumed, as shown in Figure 2. A notch of width $b = 0.25$ mm and depth a was considered, such that $a/h = 0.3$. The assumed notch location was on the top side at the center of the plate ($x = 500$ mm). Lamb waves were excited by applying an impulsive force $p(t)$ to the left edge of the plate towards the positive x -direction: this mainly stimulates the symmetric S_0 mode. The force was shaped in time as a triangular window with a total duration of $2 \mu\text{s}$ (see the top left of Figure 2) in order to excite consistent Lamb waves up to 500 kHz.

For instance, a similar excitation was obtained in [14] by focusing, through conventional optics, a laser beam to a straight line acting along the plate edge. It is shown in such work that the S_0 mode can be excited by means of such experimental setup.

To ensure accuracy to the time-transient finite element simulations [15], the plate domain was discretized with elements of maximum side length $L_{\max} = 0.125$ mm, and the time integration step was kept $\Delta t < 1e-8$ sec.

Time-dependent out-of-plane displacements $v(t)$ were recorded at three points on the top side of the plate ($y = h/2$), namely, A, B, and C, respectively, located at $x_A = 100$ mm, $x_B = 200$ mm, and $x_C = 300$ mm. The recorded waveforms are shown in Figure 3. The leftmost peak in each signal corresponds to the passage of the excited S_0 mode through the recording position (path 1, in Figure 4), while oscillations in the central part of the waveforms are due to defect-induced reflections (path 2, in Figure 4), which also excite the slower A_0 mode. Spreading of these oscillations clearly reveals the effect of dispersion. Finally, further reflections from the plate edges (path 3, in Figure 4) are responsible for the complicated behaviour observed in the rightmost part of the signals.

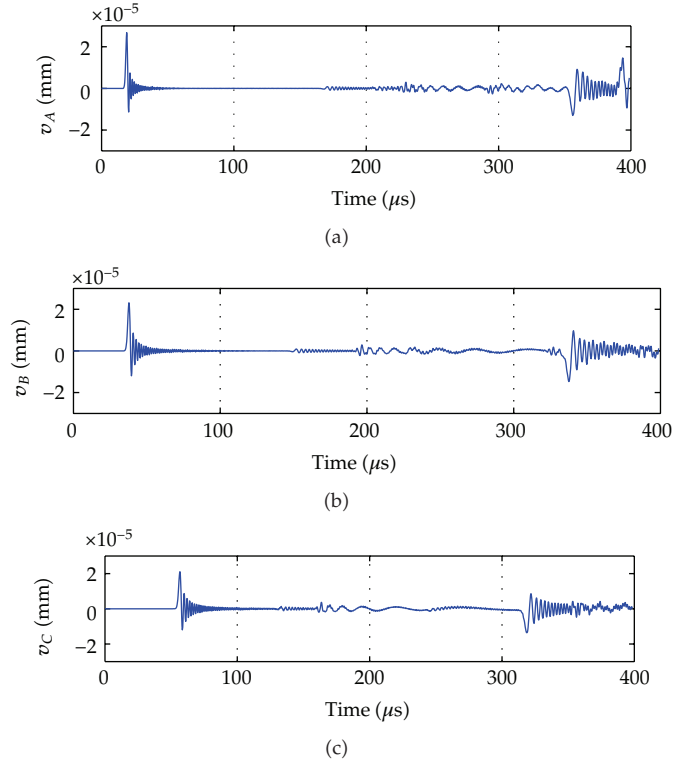


Figure 3: Time-dependent out-of-plane displacements recorded on the top side ($y = h/2$) of the plate at (a) $x_A = 100$ mm, (b) $x_B = 200$ mm, and (c) $x_C = 300$ mm.

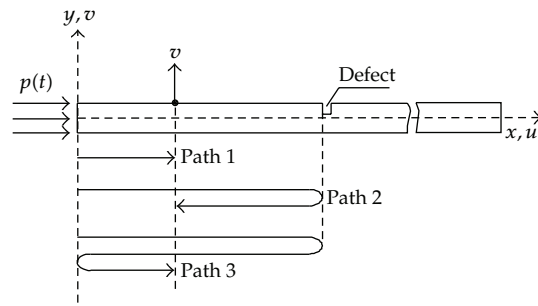


Figure 4: Schematic representation of the multiple paths traveled by the waves detected in a given acquisition point.

3. Mathematical Tools

The defect location procedure can be divided in three steps: (i) Warped Frequency Transform to remove the dispersive behaviour of the S_0 mode; (ii) equalization procedure to enhance weak reflections; (iii) Wigner-Hough Transform to distinguish S_0 reflections from other interfering waves. Such steps are detailed in the following subsections.

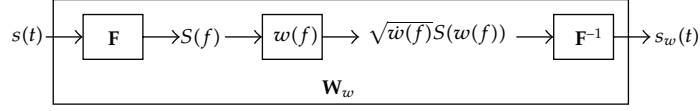


Figure 5: Computational flow of the frequency warping operator \mathbf{W}_w . \mathbf{F} and \mathbf{F}^{-1} are the direct and inverse Fourier Transform operators, respectively, while $w(f)$ and $\dot{w}(f)$ are the warping map and its first derivative.

3.1. The Warped Frequency Transform (WFT)

The WFT is a unitary time-frequency transformation that produces a flexible sampling of the time-frequency domain [16].

Given a generic signal $s(t)$ whose Fourier Transform (FT) is $S(f)$, the frequency warping operator \mathbf{W}_w transforms the original waveform into a warped version $s_w(t)$ by reshaping the frequency domain through a properly designed *warping map* $w(f)$. The procedure is depicted in Figure 5.

The WFT can be used to compensate dispersion in GWs [17] by defining the warping map through the following relationship:

$$K \frac{dw^{-1}(f)}{df} = \frac{1}{c_g(f)}. \quad (3.1)$$

Equation (3.1) relates the functional inverse $w^{-1}(f)$ of the map to the inverse of the group velocity curve, that is, $1/c_g(f)$, of the wave that we want to consider. K is a normalization parameter selected so that $w^{-1}(0.5) = w(0.5) = 0.5$. As shown in Figure 1, for acoustic emission below 500 kHz, only the two fundamental waves A_0 and S_0 can propagate through the plate. It is assumed that mostly S_0 is actuated, therefore the group velocity curve of S_0 has been used to build $w(f)$.

If $s(t)$ is an undamped guided wave at a traveled distance D from the actuator, its FT is given by $S(f) = S_0(f) \cdot e^{-j2\pi \int_0^f \tau(\alpha) d\alpha}$ where $S_0(f)$ is the FT of the actuated wave (incipient pulse) and $\tau(f) = D/c_g(f)$ represents the frequency-dependent group delay of S_0 in this case. Using (3.1), $S(f)$ can be rewritten as

$$\begin{aligned} S(f) &= S_0(f) \cdot e^{-j2\pi D \int_0^f (1/c_g(\alpha)) d\alpha} \\ &= S_0(f) \cdot e^{-j2\pi w^{-1}(f) KD}. \end{aligned} \quad (3.2)$$

By applying warping and exploiting the invertibility property of the map, that is, $w^{-1}[w(f)] = f$, yields to a signal $s_w(t)$ whose spectrum is

$$\mathbf{F}\mathbf{W}_w\{s(t)\} = \left[\sqrt{\dot{w}(f)} S_0(w(f)) \right] \cdot e^{-j2\pi f KD}. \quad (3.3)$$

The linear dependence on the *warped* frequency in this equation shows that the dispersive effect is converted in a simple *warped* time-delay (KD) proportional to the distance. Dispersion is therefore compensated, and the resulting signal s_w can be equivalently plotted

as a function of the distance from the source, thus allowing to locate defects of the excited waveguide by detecting the corresponding reflected waves.

It is worth noticing that, despite the different formalism, the processing described above is substantially analogous to the ones presented in [18, 19]. However, in many practical applications such dispersion compensation is not sufficient to ensure a reliable estimation of wave traveled distance, due to the weakness of reflections and to the interfering presence of different modes. For these reasons, necessary further processing steps are introduced in this work, as will be shown in the following sections.

3.2. Wave Equalization

By means of the warping procedure described in the previous section, a realignment of the time-frequency content of S_0 waves in vertical lines is produced. However, in general the energy of the waves scattered by defects is much lower than the energy of the incident wave, especially for small defects. To overcome this problem, the energy of incident and reflected waves in the acquired signal can be conveniently equalized. Such task can be accomplished with a simple but effective procedure based on a local averaging of the acquired signal. Indicating with $LA(|s_w(x)|)$ the local average of $|s_w(x)|$ in the neighborhood of x , the equalized signal $s_{we}(x)$ is obtained as

$$s_{we}(x) = \frac{s_w(x)}{\max\{LA(|s_w(x)|), T\}}, \quad (3.4)$$

where T is a given threshold, set as the 5% of the maximum value of $|s_w(x)|$, which is used to avoid the undesired amplification of numerical noise when the signal is absent. In experimental data, the value of T must be set according to the SNR of the acquisition setup.

The warped and equalized versions of the signal in Figure 3(a) are plotted in Figures 6(a) and 6(c), respectively. The equalization factor $\max\{LA(|s_w(x)|), T\}$ is depicted in Figure 6(b).

3.3. The Wigner-Hough Transform (WHT)

After equalization, defect detection can be performed automatically with a further processing of the signal $s_{we}(x)$. It is worth noticing that the energy of spurious contribution (caused by multimodal propagation or mode conversion) is quite high in the equalized signal compared to the energy of compensated S_0 waves. In the example of Figure 6(c), the peak related to the S_0 wave reflected by the defect (indicated as S_0 path 2) is just about twice as high as the peak in the following mode-converted wave (A_0). Therefore it is quite difficult to implement simple thresholding procedures capable of distinguishing different wave modes in this representation.

However, defect-induced reflections of the analyzed mode (S_0 in this example) appear in the compensated waveform as well-localized spikes, thus producing vertical maxima lines in a TF representation, whose (warped) time location can be directly converted to the defect position. On the contrary, spurious contributions related to different modes (A_0 in this example) show a peculiar frequency modulation due to a different group velocity curve from the one of S_0 . This can be clearly observed in a simple TFR of $s_{we}(t)$, provided by the short-time Fourier transform (STFT), shown in Figure 7.

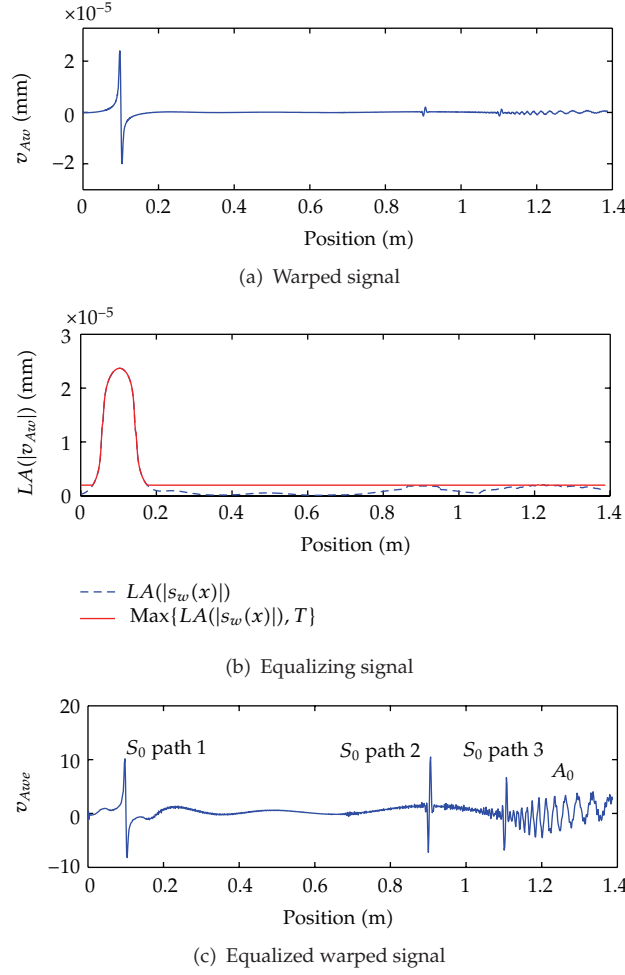


Figure 6: (a) Warped version v_{Aw} of the signal v_A represented in Figure 3(a). (b) Equalization factor for the same signal. (c) Equalized warped signal v_{Awe} as a result of the equalization procedure.

Other energy distributions, such as the Wigner-Ville distribution (WVD), defined as

$$W_{s_{we}}(t, f) = \int_{-\infty}^{+\infty} s_{we}\left(t + \frac{\tau}{2}\right) s_w^*\left(t - \frac{\tau}{2}\right) \cdot e^{-j2\pi f\tau} d\tau \quad (3.5)$$

can be used to further improve the effectiveness of the representation. In fact, WVD provides optimal energy localization of linear chirp signals in the time-frequency plane [20]. It follows that applying vertical line detection algorithms to the WVD of the compensated signals provides an asymptotically optimal detector of wave propagating distances.

In particular, automatical detection of the desired lines of energy maxima can be performed by applying the Hough Transform (HT) [21] to the WVD, resulting in the so-called Wigner-Hough Transform (WHT) [22]. Generally speaking, the HT is an image processing tool that performs an integration on all the possible lines of a given image I and maps the value of each integral to a (ρ, θ) plane corresponding to the polar parametrization of

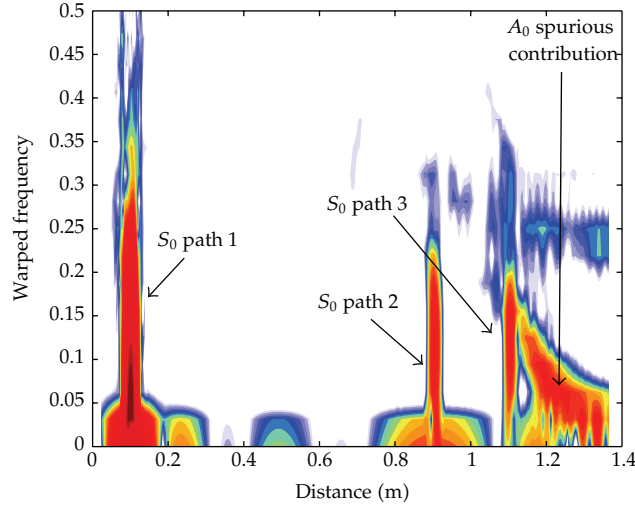


Figure 7: Spectrogram of the equalized waveform v_{Awe} represented in Figure 6(c).

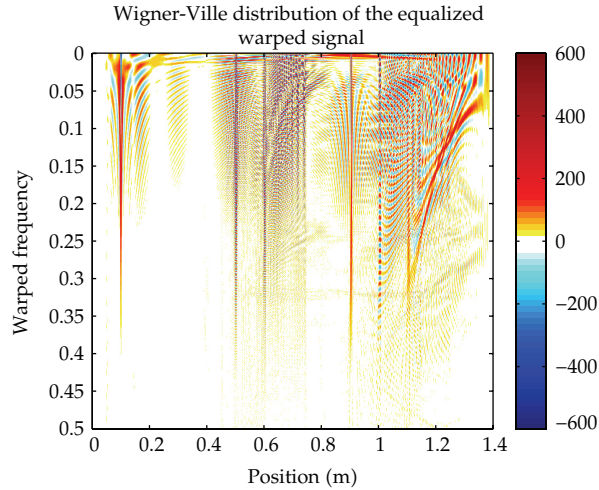


Figure 8: Wigner-Ville distribution (WVD) of the equalized waveform v_{Awe} represented in Figure 6(c).

the lines. High-intensity pixels concentrated on straight lines on I will therefore produce peaks in the (ρ, θ) domain. In the Wigner-Hough Transform, the input image corresponds to the WVD of the considered signal and, in our approach, emphasis is placed in finding vertical lines, located at $\theta = \{\pi/2, 3\pi/2\}$. Therefore, in the WHT, the portion which corresponds to these angles is isolated, and the ρ value corresponding to detected peaks represents the distance traveled by the wave. One of the major limitations of the WVD is the presence of interference terms between different spectral components of the analyzed waveform induced by the WVD. However, it is worth noticing that this inconvenience is largely compensated through the integration performed by the Hough operator, as these undesired components appear as alternating positive peaks and negative valleys in the TF plane.

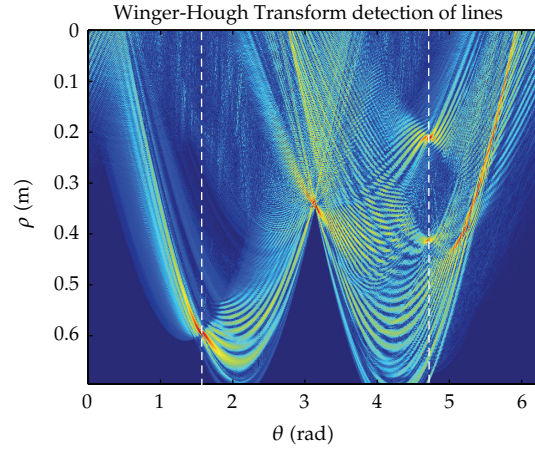


Figure 9: Hough Transform of the Wigner-Ville distribution (WHT) represented in Figure 8. Peaks at $\theta = \{\pi/2, 3\pi/2\}$ (dashed lines) correspond to vertical lines in Figure 7; ρ coordinates provide the distance from the center of the analyzed image.

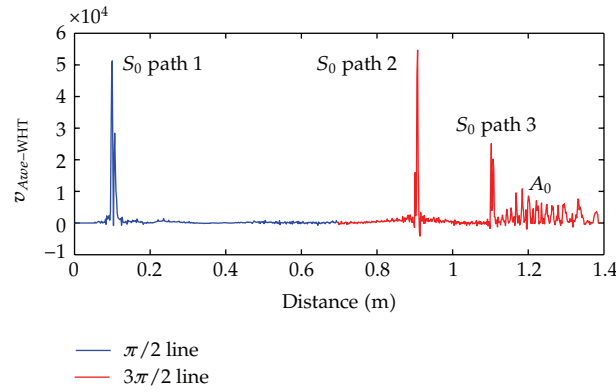


Figure 10: $v_{Ave-WHT}$ extracted for the values of $\theta = \pi/2$ and $3\pi/2$ from the WHT of Figure 9, computed for the signal v_{Ave} represented in Figure 8.

4. Procedure of the Method

The mathematical tools detailed in the previous section can be efficiently implemented by the following processing steps.

- (i) The discrete WFT can be computed with the approach described in [23]. In essence, the warped signal is obtained by performing a nonuniform Fourier Transform [24] followed by an inverse Fourier Transform. Fast-Fourier algorithms can be exploited to compute both the direct nonuniform and the inverse transforms.
- (ii) In the second step, warped signals are equalized in amplitude, according to (3.4). The local averaging window applied in the right hand term of the same equation is about 9 cm in length (it is worth recalling that, in the warped domain, time intervals are related to distances).

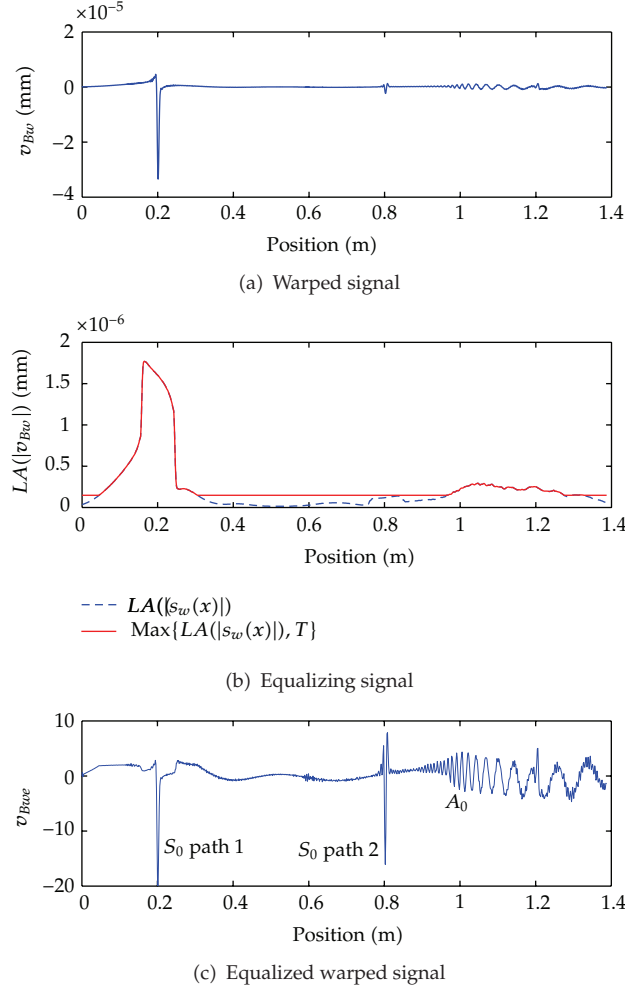


Figure 11: (a) Warped version v_{Bw} of the signal v_B presented in Figure 3(b). (b) Equalization factor for the same signal. (c) Equalized warped signal v_{Bwe} as a result of the equalization procedure.

- (iii) The software (Time-Frequency Toolbox—TFTB) which computes the Wigner-Ville distribution adopted in this study is available for academic use at <http://tftb.nongnu.org/>. In the same tool, also the code for Hough Transform computation is provided. However, for wave propagating distance estimation, the calculation of the Hough Transform coefficients in the whole (ρ, θ) plane is redundant, as described in Section 3.3. For this reason, in our approach such calculation is simplified with a simple integration of WVD coefficients across frequencies.

5. Numerical Results

The WVD of the equalized warped signal in Figure 6 is depicted in Figure 8. As it can be seen, two vertical lines appears in correspondence to the actual traveled distances of the incident

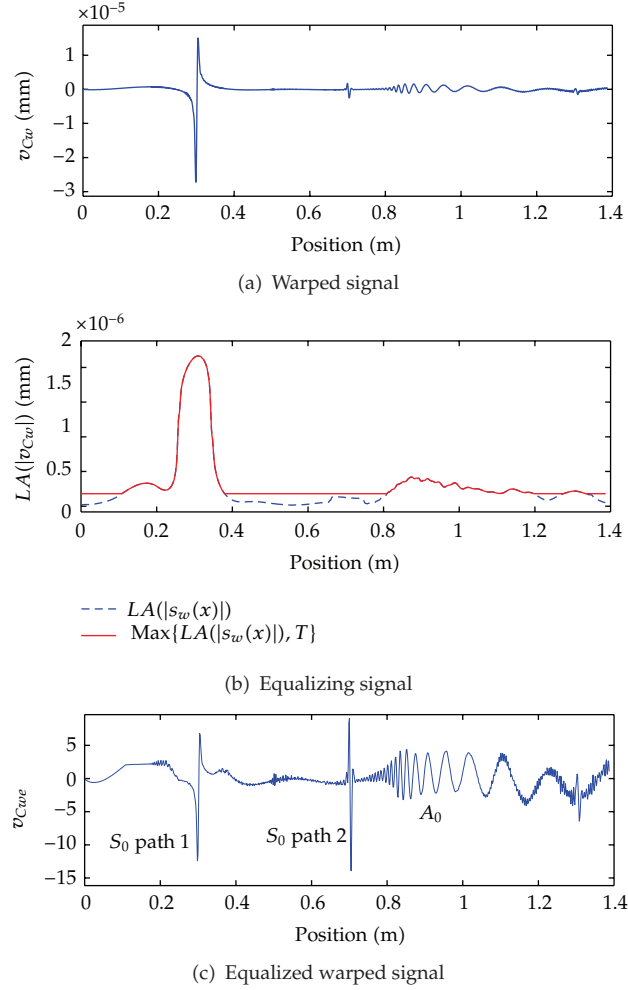


Figure 12: (a) Warped version v_{Cw} of the signal v_C presented in Figure 3(c). (b) Equalization factor for the same signal. (c) Equalized warped signal v_{Cwe} as a result of the equalization procedure.

and scattered wave (at 0.1 and 0.9 m, resp.) together with spurious contribution due to different modes of propagation and interference terms.

The computation of the WHT, that is, the Hough Transform on the WVD, produces the image depicted in Figure 9, where three peaks can be associated with $\theta = \pi/2$ and $3\pi/2$. The peaks ordinates represent the difference between the effective distance of propagation of a given wave and a reference distance of propagation of 0.7 m, which corresponds to the half of the maximum considered propagation distance in the analyses of 1.4 m.

By extracting the values related to $\theta = \pi/2$ and $3\pi/2$ in the WHT and reordering them according to the distance from the origin, a novel signal s_{we-WHT} is obtained. In such signal, depicted in Figure 10, the peaks related to the actual traveled distances of S_0 waves clearly emerge with respect to the spurious contribution due to mode-converted waves, thus greatly simplifying the definition of automated distance estimation procedures. In particular, the amplitude of the peak related to the reflected S_0 (path 2) is about 10 times higher than

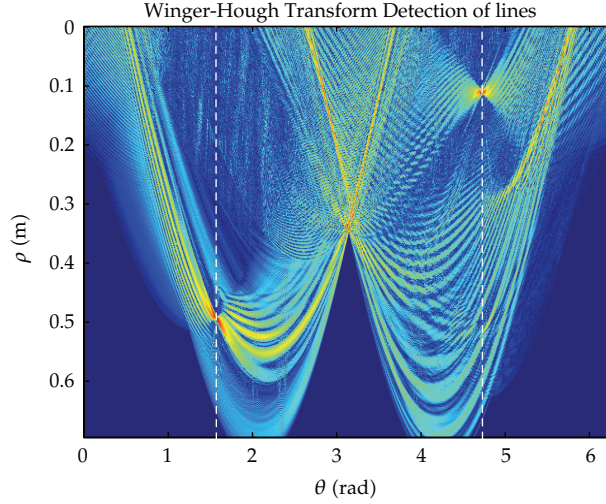


Figure 13: Wigner-Hough Transform (WHT) of the equalized warped signal v_{Bwe} represented in Figure 11(c). Peaks at $\theta = \{\pi/2, 3\pi/2\}$ (dashed lines) correspond to vertical lines in the Wigner-Ville distribution; ρ coordinates provide the distance from the center of the analyzed domain.

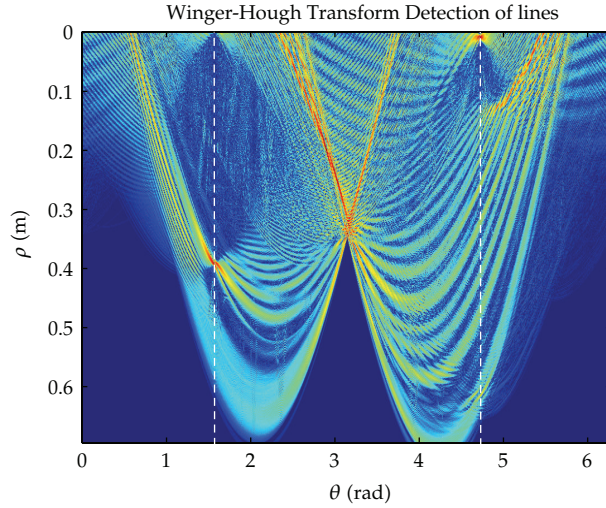


Figure 14: Wigner-Hough Transform of the equalized warped signal v_{Cwe} represented in Figure 12(c). Peaks at $\theta = \{\pi/2, 3\pi/2\}$ (dashed lines) correspond to vertical lines in the Wigner Ville distribution; ρ coordinates provide the distance from the center of the analyzed domain.

the maximum values of spurious contribution, that is, five times more with respect to the dispersion compensated wave of Figure 6. Similar results have been obtained by processing the signals v_B and v_C represented in Figures 3(b) and 3(c).

Also for these signals, in fact, it can be seen that the path followed by the compensated mode S_0 can be tracked by observing local peaks in the warped signals, as illustrated in Figures 11(a) and 12(a), and the location of the defect can be inferred by the position of reflected peaks. However, the amplitude of the reflected S_0 peak, at 0.8 m in Figure 11(a) and 0.7 m in Figure 12(a), is much smaller compared to that on the incident S_0 mode and

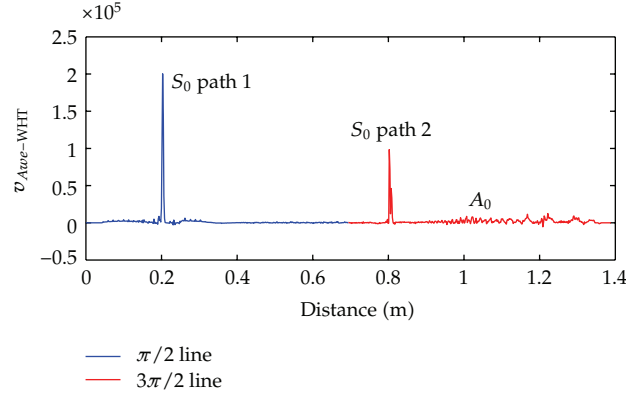


Figure 15: $v_{Bwe}\text{-WHT}$ extracted for the values $\theta = \pi/2$ and $3\pi/2$ from the WHT of v_{Bwe} represented in Figure 13.

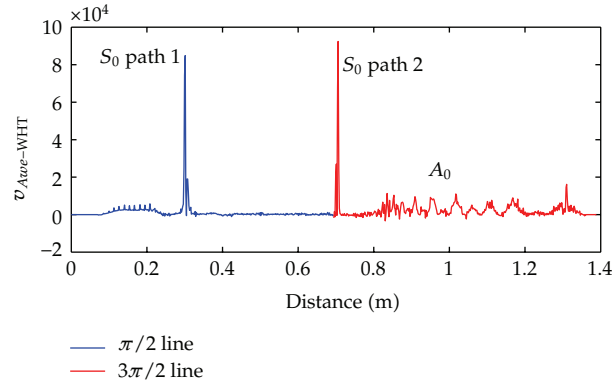


Figure 16: $v_{Cwe}\text{-WHT}$ extracted for the values $\theta = \pi/2$ and $3\pi/2$ from the WHT of v_{Cwe} represented in Figure 14.

comparable to that of the reflected spurious A_0 wave. It follows that the location of defects by exploiting only warped signals could be difficult in real noisy applications. As for the first case discussed, the proposed robust and automated approach involves first an equalization of the warped signal to emphasize the amplitude of reflection-induced peaks and next the detection of vertical maxima lines in a space-frequency representation (WHT) of the equalized warped signals.

The Wigner-Hough Transform, in fact, appears as a suitable tool to isolate S_0 components and locate defect-induced reflections, as it can be seen from Figures 13 and 14, where the WHT of the equalized warped signals v_{Bwe} and v_{Cwe} , respectively, are displayed.

Local maxima at $\theta = \pi/2$ and $\theta = 3\pi/2$ can be easily detected, and the corresponding ρ coordinates provide the distance traveled by the incident and reflected S_0 waveform components, respectively.

From the extraction of peak coordinates in the waveforms $s_{we}\text{-WHT}$ depicted in Figures 10, 15, and 16, the defect responsible for reflections is located at $x = 503$ mm, $x = 502$ mm, and $x = 502$ mm, respectively. Errors with respect to the actual defect position ($x = 500$ mm) are thus below 3 mm, which roughly corresponds to the minimum wavelength associated with

the excited Lamb waves. Similar good results were found by considering different defect depths and positions, not shown here for the sake of brevity.

6. Conclusions

The work described the application of a Warped Wigner-Ville analysis to improve defect detectability of conventional Lamb wave inspection systems. The proposed equalization approach effectively enhances the amplitude of relevant peaks in warped signals, where dispersion for a GW mode of interest has been removed. This procedure may encounter limitations in the presence of especially noisy signals, as spurious components might be erroneously amplified. However, several alternatives are possible, including more sophisticated preprocessing algorithms under investigation and the averaging of multiple acquisitions.

The Wigner-Ville distribution of the equalized signal is then computed. The presence of interference terms is largely compensated through the integration of the time-frequency decomposition performed by the Hough operator.

In the resulting Winger-Hough Transform representation, vertical lines associated with relevant acoustic events can be detected. This allows for the separation of overlapping Lamb waves. In particular, it was shown with numerical examples that the contribution of S_0 can be highlighted and the one due to interfering terms (such as A_0 wave) deeply attenuated.

Finally, with simple thresholding procedures, the information about the distance traveled by the incident and reflected components of a monitored wave can be easily recognized. Thanks to its very high precision the developed tool could pave the way for a new class of procedures to locate defects in waveguides.

References

- [1] T. Ghosh, T. Kundu, and P. Karpur, "Efficient use of Lamb modes for detecting defects in large plates," *Ultrasonics*, vol. 36, no. 7, pp. 791–801, 1998.
- [2] J. L. Rose, *Ultrasonic Waves in Solid Media*, Cambridge University Press, New York, NY, USA, 1999.
- [3] Y. Lu, L. Ye, Z. Su, and C. Yang, "Quantitative assessment of through-thickness crack size based on Lamb wave scattering in aluminium plates," *NDT and E International*, vol. 41, no. 1, pp. 59–68, 2008.
- [4] L. De Marchi, M. Ruzzene, B. Xu, E. Baravelli, and N. Speciale, "Warped basis pursuit for damage detection using Lamb waves," *IEEE Transactions on Ultrasonics, Ferroelectrics, and Frequency Control*, vol. 57, no. 12, pp. 2734–2741, 2010.
- [5] E. Dehghan Niri and S. Salamone, "A probabilistic framework for acoustic emission source localization in plate-like structures," *Smart Materials and Structures*, vol. 21, no. 3, Article ID 035009, 2012.
- [6] T. Kundu, H. Nakatani, and N. Takeda, "Acoustic source localization in anisotropic plates," *Ultrasonics*, vol. 52, no. 6, pp. 740–746, 2012.
- [7] R. Benz, M. Niethammer, S. Hurlbauss, and L. J. Jacobs, "Localization of notches with Lamb waves," *Journal of the Acoustical Society of America*, vol. 114, no. 2, pp. 677–685, 2003.
- [8] A. Leger and M. C. Deshamps, *Ultrasonic Wave Propagation in Non Homogeneous Media*, Springer, New York, NY, USA, 2009.
- [9] M. J. S. Lowe, "Matrix techniques for modeling ultrasonic waves in multilayered media," *IEEE Transactions on Ultrasonics, Ferroelectrics, and Frequency Control*, vol. 42, no. 4, pp. 525–542, 1995.
- [10] P. Bocchini, A. Marzani, and E. Viola, "Graphical user interface for guided acoustic waves," *Journal of Computing in Civil Engineering*, vol. 25, no. 3, pp. 202–210, 2011.
- [11] F. Chen and P. D. Wilcox, "The effect of load on guided wave propagation," *Ultrasonics*, vol. 47, no. 1–4, pp. 111–122, 2007.
- [12] L. De Marchi, A. Marzani, N. Speciale, and E. Viola, "Prediction of pulse dispersion in tapered waveguides," *NDT and E International*, vol. 43, no. 3, pp. 265–271, 2010.

- [13] "Abaqus—release 6.12," 2012, <http://www.simulia.com/>.
- [14] M. Sale, P. Rizzo, and A. Marzani, "Semi-analytical formulation for the guided waves-based reconstruction of elastic moduli," *Mechanical Systems and Signal Processing*, vol. 25, no. 6, pp. 2241–2256, 2011.
- [15] I. Bartoli, F. Lanza Di Scalea, M. Fateh, and E. Viola, "Modeling guided wave propagation with application to the long-range defect detection in railroad tracks," *NDT and E International*, vol. 38, no. 5, pp. 325–334, 2005.
- [16] S. Caporale, L. De Marchi, and N. Speciale, "Frequency warping biorthogonal frames," *IEEE Transactions on Signal Processing*, vol. 59, no. 6, pp. 2575–2584, 2011.
- [17] L. De Marchi, A. Marzani, N. Speciale, and E. Viola, "A passive monitoring technique based on dispersion compensation to locate impacts in plate-like structures," *Smart Materials and Structures*, vol. 20, no. 3, Article ID 035021, 2011.
- [18] R. Sicard, J. Goyette, and D. Zellouf, "A numerical dispersion compensation technique for time recompression of Lamb wave signals," *Ultrasonics*, vol. 40, no. 1–8, pp. 727–732, 2002.
- [19] P. D. Wilcox, "A rapid signal processing technique to remove the effect of dispersion from guided wave signals," *IEEE Transactions on Ultrasonics, Ferroelectrics, and Frequency Control*, vol. 50, no. 4, pp. 419–427, 2003.
- [20] E. Chassande-Mottin and P. Flandrin, "On the time-frequency detection of chirps1," *Applied and Computational Harmonic Analysis*, vol. 6, no. 2, pp. 252–281, 1999.
- [21] L. Shapiro and G. Stockman, *Computer Vision*, Prentice Hall, New York, NY, USA, 2001.
- [22] S. Barbarossa, "Analysis of multicomponent LFM signals by a combined Wigner-Hough transform," *IEEE Transactions on Signal Processing*, vol. 43, no. 6, pp. 1511–1515, 1995.
- [23] S. Caporale, L. De Marchi, and N. Speciale, "Fast computation of frequency warping transforms," *IEEE Transactions on Signal Processing*, vol. 58, no. 3, pp. 1110–1121, 2010.
- [24] L. Greengard and J.-Y. Lee, "Accelerating the nonuniform fast fourier transform," *SIAM Review*, vol. 46, no. 3, pp. 443–454, 2004.

Research Article

Finite Element Modelling Tuned on Experimental Testing for the Structural Health Assessment of an Ancient Masonry Arch Bridge

G. Castellazzi, S. De Miranda, and C. Mazzotti

DICAM Department, University of Bologna, Viale Risorgimento 2, 40136 Bologna, Italy

Correspondence should be addressed to G. Castellazzi, giovanni.castellazzi@unibo.it

Received 22 August 2012; Accepted 30 August 2012

Academic Editor: Ivan Bartoli

Copyright © 2012 G. Castellazzi et al. This is an open access article distributed under the Creative Commons Attribution License, which permits unrestricted use, distribution, and reproduction in any medium, provided the original work is properly cited.

This paper presents the structural health assessment of a railway ancient masonry arch bridge located in Bologna, Italy. A three-dimensional finite element model of the entire bridge, tuned on in situ experimental tests, has been used for the assessment. In particular, the finite element model has been employed to evaluate the structural health of the bridge both in its actual state and in the hypothesis of a structural strengthening intervention.

1. Introduction

The train loads and the train traffic amount increased tremendously in this last century. Nevertheless, many railway masonry arch bridges built in the nineteenth and twentieth centuries are still in service. For this reason and due to the continuous exposure to environmental aggressive conditions, a good number of these bridges suffer important mechanical deteriorations. The definition of an effective process of assessment of the actual structural health of these fundamental infrastructures is thus becoming more and more important (see, e.g., [1–5] and the references therein).

In the present paper, the procedure applied for the structural health assessment of the railway masonry arch bridge crossing the Reno river in Bologna (Italy), see Figure 1, is presented, together with the obtained results. Some preliminary results have been presented in [6]. The procedure is based on the combined use of three-dimensional finite element modelling [7–10] and in situ experimental testing. A number of experimental tests have been carried out in order to find out both the material properties of the masonry constituting the arches and the piers and the structural behavior of the bridge or of portions of it. In particular, accurate static and dynamic load tests have been performed on some arches whereas simplified dynamic tests have been repeated on all the spans of the bridge in order



Figure 1: (a) Longitudinal view of the multi-span masonry arch bridge as appears today and (b) view of a construction phase, presumably dated around 1852.

to verify the homogeneity of their structural behavior. The experimental findings have been used to tune a three-dimensional finite element model of the whole bridge, able to describe the static and dynamic behavior of the structure under service conditions (train traffic). In particular, a part of the experimental outcomes have been used to calibrate the finite element model and a part to validate it. A very good agreement between experimental and numerical results has been obtained, so confirming the accuracy of the assumptions made in setting up the finite element model. Then, the tuned finite element model has been used for the evaluation of the structural health of the bridge both in its actual state and in the hypothesis of a structural strengthening intervention.

The paper is organized as follows. The three-dimensional finite element model is presented in Section 2. Section 3 is devoted to the description of the in situ experimental tests. The tuning of the finite element model is presented in Section 4 and its use for the structural health assessment of the bridge in Section 5. Some concluding remarks end the paper (Section 6).

2. The Three-Dimensional Finite Element Model

The bridge, built in 1852, has 15 arch spans and an overall length of 360 m. Arches have a 20 m free span, and piers are 2 m thick and 10 m high (Figure 2). The bridge was originally designed for two railway tracks, with a barrel width of 9 m (older part/bridge in the following). Later, the bridge was enlarged building a second, 6 m width, barrel (newer part/bridge in the following) in order to increase the number of tracks (Figure 2). Visual inspection of the intrados reveals that the barrels seem to be separated (percolation from the rail deck is visible along all the arches), so slips between the two parts are possible. The evaluation of the degree of collaboration of the two parts is one of the key aspects of the investigation.

A three-dimensional finite element model of the whole bridge, able to describe its static and dynamic behaviors, has been set up (Figure 3). The model, developed using the commercial code Abaqus [11], has been defined starting from the existing historical drawings and encompasses details discovered during the on-site inspection. Fine description of all the geometry's components is given (Figure 4) along with the subdivision of material

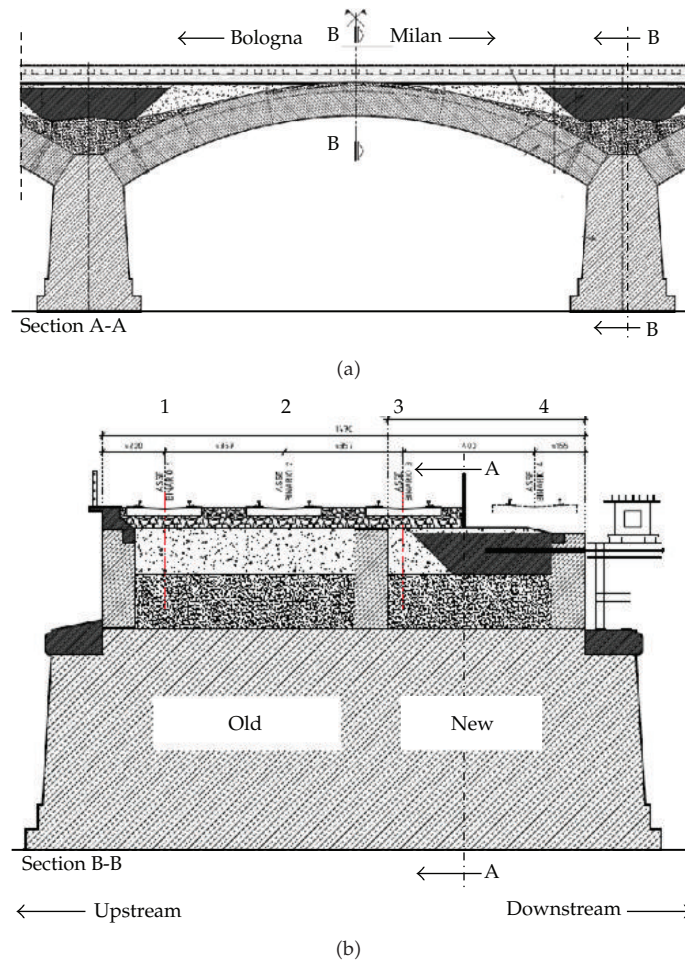


Figure 2: (a) Longitudinal and (b) transverse cross sections of the typical bridge span with indication of different materials.

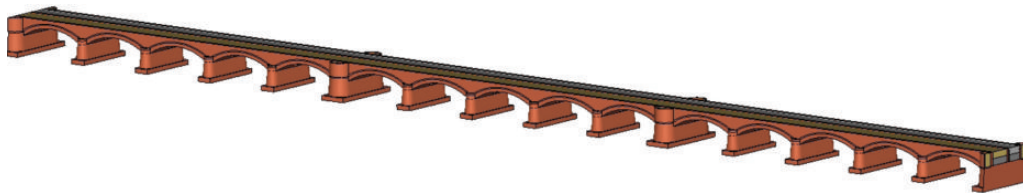


Figure 3: Full view of the 3D finite element model.

layers: masonry, filling material, and so on (Figure 5). Hexahedral 8-node linear elements (Abaqus C3D8) [11] have been employed together with the reduction to 6-node linear triangular prism elements (Abaqus C3D6) and the 4-node linear tetrahedral element (Abaqus C3D4). These elements are general purpose linear brick elements, fully integrated ($2 \times 2 \times 2$ integration points) and sensitive to extreme mesh distortions [12], which tend to give stiffer dynamic response for coarse meshes. Being the model intended to assess the structural health under service conditions, all materials have been assumed to work in the linear range thus

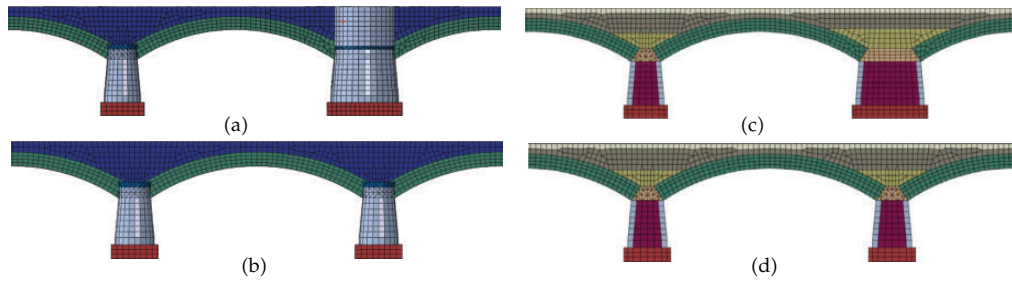


Figure 4: Partial views and sections of the 3D finite element model: representation of material properties subdivision.

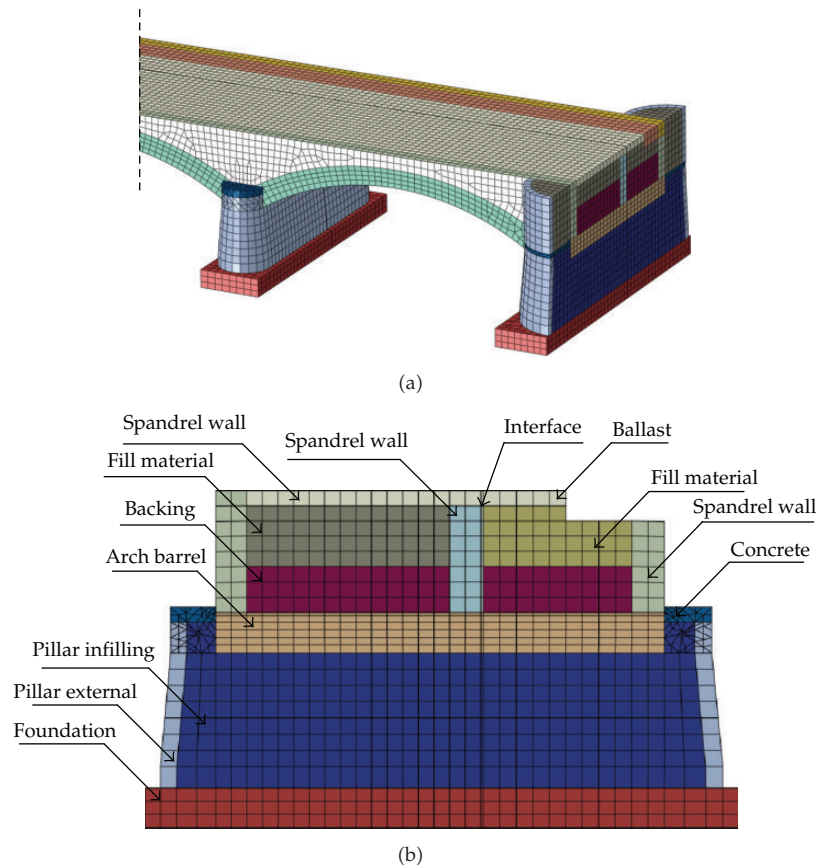


Figure 5: (a) View of a portion of the 3D finite element model of the structure with the representation of material properties subdivision and (b) section view using a cutting plane on the principal pillar.

producing a linear elastic model. Moreover, the materials have been assumed isotropic except for the material used to model the interface connecting the old bridge and the new bridge. This part has been modeled using an orthotropic material: in-plane directions are weak directions (sliding with friction), and the orthogonal direction to this plane possesses full stiffness as the masonry material (contact). Perfectly clamped boundary conditions at the base of the piles and at the abutments have been assumed.

3. In Situ Dynamic and Static Tests

In this section, the dynamic and static tests carried out to investigate the structural behavior of the railway bridge under service loading are described. Loads generated by trains have been used in both cases.

3.1. Dynamic Tests

The purpose of dynamic tests is to identify the main natural frequencies and the mode shapes of the bridge. After verifying that all the spans of the bridge have a similar dynamic behavior (by means of simplified dynamic tests not reported here), a comprehensive dynamic test has been carried on a single span only (the 4th span, hereinafter called C4). The structure has been dynamically excited by means of the regular transit of trains.

3.1.1. Instrumentation

To measure the acceleration produced by the riding of the train on the bridge, twelve piezo-electric accelerometers have been used. They have a sensitivity of 10 V/g and they have been placed at the arch intrados at midspan and at quarters of the arch freespan; six accelerometers measure the accelerations of the older part of the arch span while the other six measure the accelerations of the newer part (Figure 6(a)). All instruments have been mechanically clamped to the bridge in a direction orthogonal to the arch intrados (Figure 6(b)). Data have been acquired by using a 16-bit DAQ board and stored in a PC for further processing.

3.1.2. Measurements and Dynamic Identification

During the transit of trains on the bridge a number of acceleration time histories have been recorded. Figure 7(a) shows an example of time history recorded by accelerometer A7 (see Figure 6(a)) during a high velocity train transit. From the acceleration, power spectral density has been evaluated for each position and time history; an example of PSD corresponding to the acceleration of Figure 7(a) is reported in Figure 7(b).

Since the dynamic excitation applied to the bridge by the train during the riding is unknown, in order to identify the natural frequencies and mode shapes of the arch bridge an output-only identification technique has to be used. In particular, the Enhanced Frequency Domain Decomposition (EFDD) technique is applied at the present case [13]. It considers the dynamic force generated by the train like a white noise, and the PSD matrix of the problem is decomposed in order to obtain, starting from an n -DoF dynamic system, an n -SDoF systems. The PSD of the obtained systems is identified by classical SDoF techniques (peak picking) see [14] for further details. The first four natural frequencies identified are $f_1 = 9.12$ Hz, $f_2 = 9.62$ Hz, $f_3 = 11.21$ Hz, and $f_4 = 14.10$ Hz. The corresponding mode shapes are reported in Figure 8. The first two modes are both mainly flexural modes, but in the first case the older arch is more deflected than the newer one, confirming possible slips between arches. The opposite happens for the second mode shape. The third mode (Figure 8(c)) describes the deflection of the two arches with opposite signs, and also an appreciable torsional behavior can be found. Finally, the fourth mode (Figure 8(d)) is similar to a beam second flexural mode with almost null deflection at midspan for both arches.

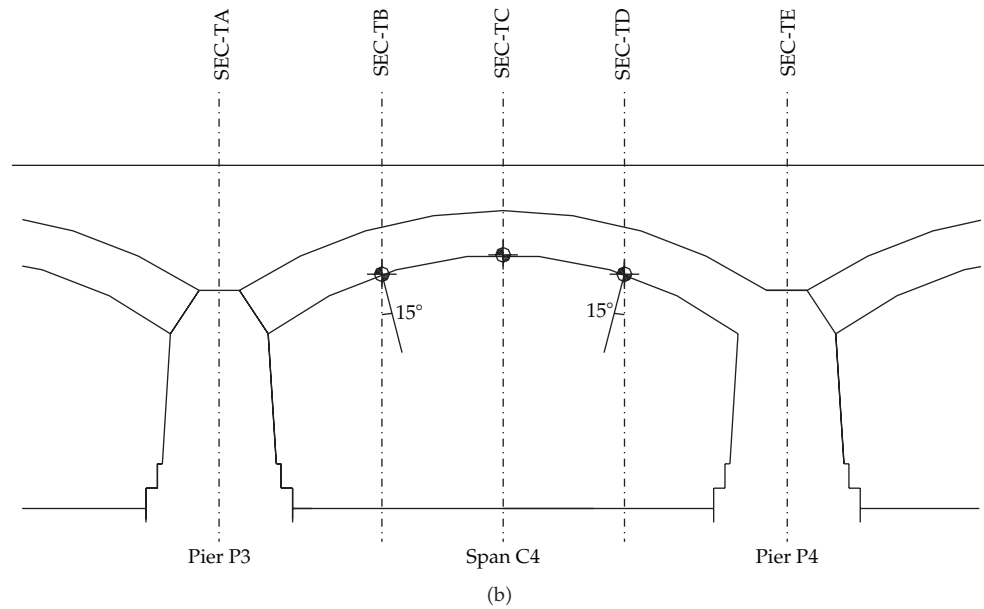
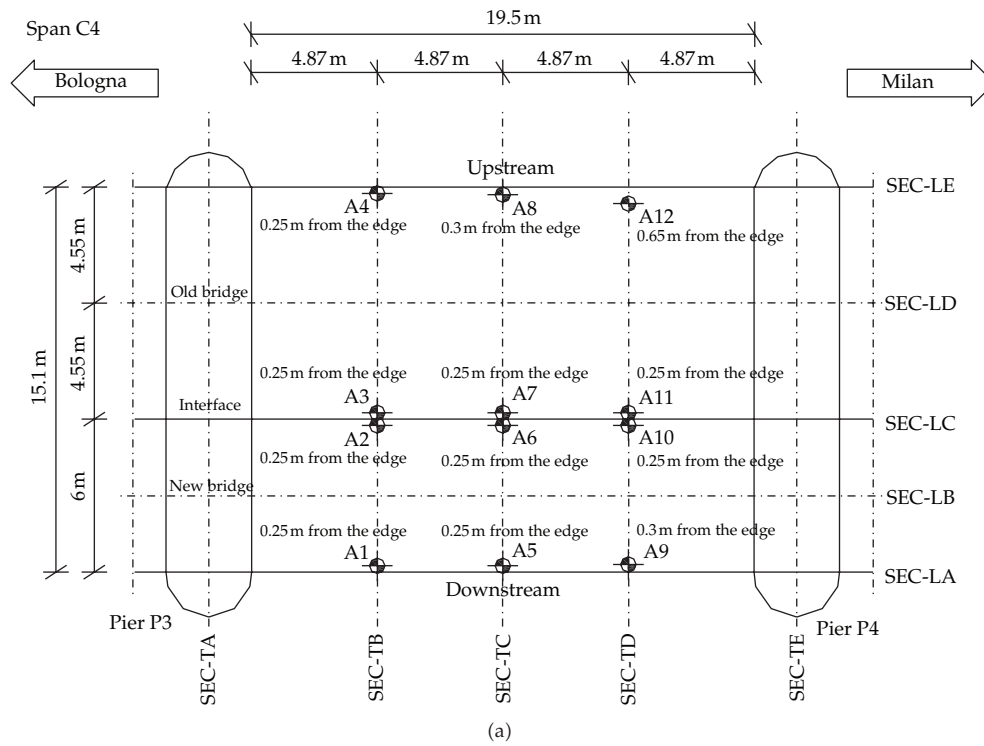


Figure 6: (a) Plan and (b) lateral view of the 4th span (C4) of the arch bridge with positions of accelerometers.

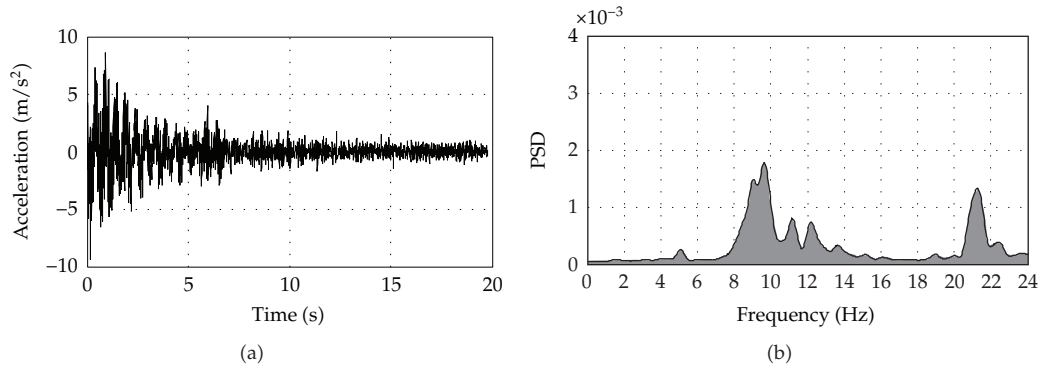


Figure 7: (a) Example of acceleration recorded during the pas-sage of a train on the bridge and (b) corresponding power spectral density.

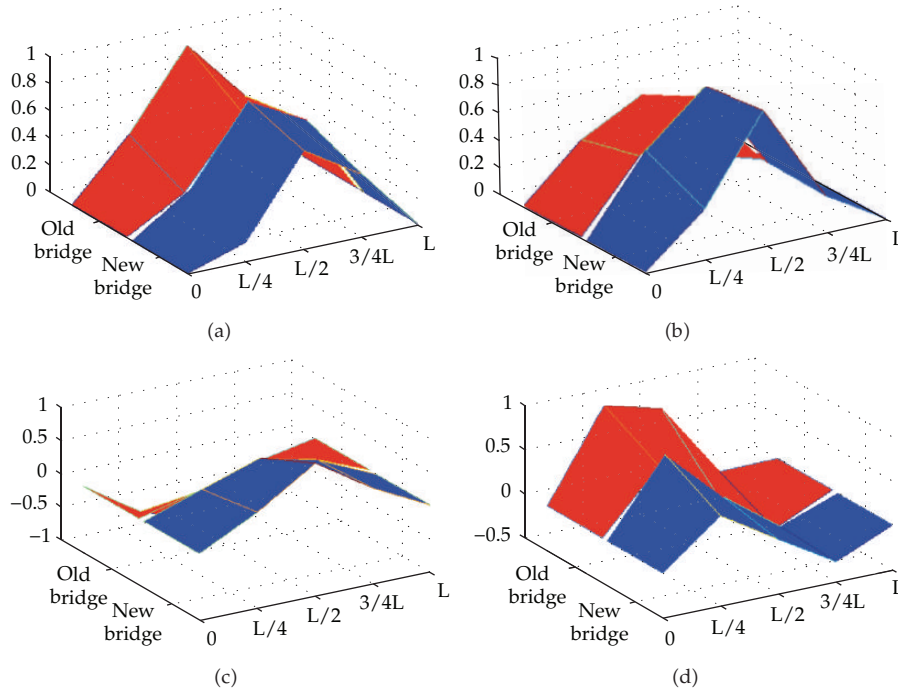


Figure 8: (a) Modal shapes of one arch span identified from dynamic tests.

3.2. Static Test

The same bridge span (C4) as before has been also tested under static loads. In particular, three locomotives have been used to apply the desired load combinations. In this way, a better investigation of the possible slips between the two arches (older and newer) has been performed.

3.2.1. Instrumentation

Vertical displacements of the arches intrados during the test have been measured by using nine LVDT displacement transducers (L1–L7 and F1–F2 of Figure 9(a)). They have been

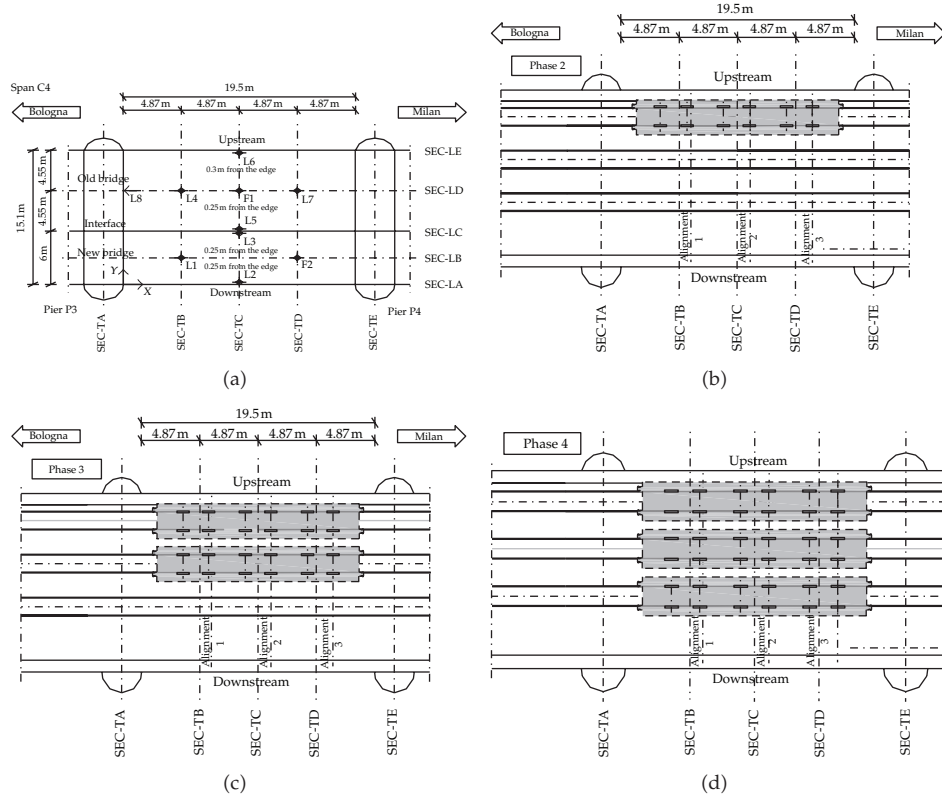


Figure 9: (a) Plan of the 4th span (C4) of the arch bridge with positions of displacement transducers and (b–d) phases 2 to 4 of static loadings.

positioned at midspan and at quarter-span of the arches. The vertical displacement of the piers is considered very small, and, consequently, they have been neglected.

3.2.2. Load Combinations and Measurement

The three available locomotives have been positioned in a number of different load combinations on the considered bridge span. In this way, it has been possible to investigate not only the overall flexural behavior but also the torsional effects and the degree of mechanical coupling between the two adjacent arches built in following periods. Locomotives positioned along tracks 1 and 2 weighted 106 t while the third locomotive, moving on track 3, weighted 120 t.

For the sake of brevity, only a part of the load combinations realized are shown in the paper. In particular, the torsional behavior has been investigated by placing one to three locomotives at midspan along tracks one to three (Figures 9(b), 9(c), and 9(d)). Figure 10(a) shows the corresponding results in terms of vertical displacements: an appreciable slip between the two arches can be observed even though their cross-sections remain substantially plane. In phase 4 the torsional rotation is smaller because of the position of track 3, crossing the two arches. The flexural deflection of arches has been studied by positioning the three locomotives along tracks 1 to 3 progressively closer to midspan (see phases 6, 7, and 4 described resp. in Figures 11(a), 11(b), and 9(c)). The corresponding vertical displacements

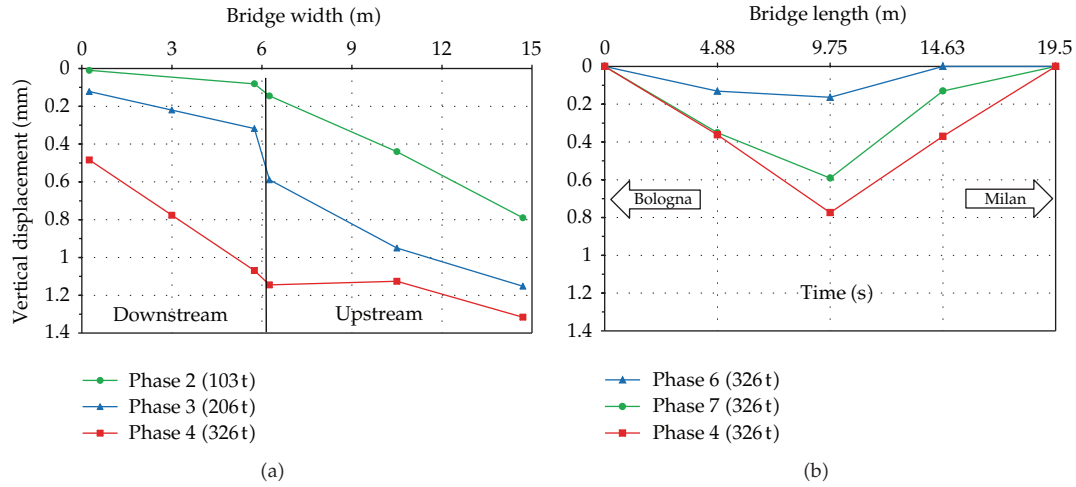


Figure 10: (a) Vertical displacement of midspan cross-section during loading phases 2–4; (b) vertical displacements along the longitudinal axis of the newer part of the instrumented arch-span during loading phases 6, 7, and 4.

along the longitudinal axis of the newer arch (Figure 10(b)), as expected, show a deflected shape moving from the left pier (phase 6) toward midspan (phase 4). Finally, another loading condition (phase 12) has been applied to the bridge span, where the three locomotives were placed along the tracks shifted one with respect to the other ones (Figure 12). In this way the torsional effect has been applied not only at midspan but also along the whole span. Obtained results are shown later compared to numerical results.

3.3. Material Characterization

Together with the structural identification, the mechanical properties of masonry constituting the arch bridge have been also investigated [15]. Portions of masonry have been taken from five bridge spans (Figure 13(a)) in order to obtain several brick and mortar specimens. After proper geometrical regularization, brick specimens have been subjected to compression test while mortar specimens to double punching shear test (Figure 13(b)). Following procedure suggested in Eurocode 6 [16], from the results of single materials the masonry characteristic compressive strength $f_{mk} = 8.2 \text{ MPa}$ has been obtained.

4. Tuning of the Finite Element Model

Usually, when experimental measurements are performed to validate numerical models, they do not coincide with the expected numerical results. These discrepancies originate from the uncertainties in simplifying assumptions of structural geometry, materials, as well as inaccurate boundary conditions. In the present case, most of the numerical simplification lies into the assumption of linear behavior for the materials. The problem of how to modify the numerical model taking into account the experimental results, essential for the reliability of the model, is known as model updating; see, for instance [17, 18].

Model updating procedure aims at minimizing the differences between the analytical and experimental results by changing uncertainty parameters such as material properties and

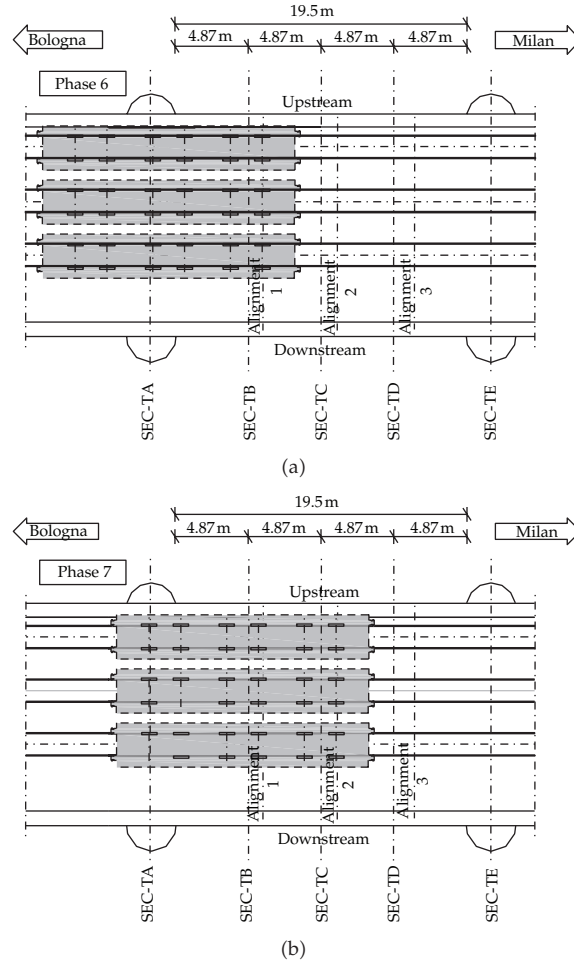


Figure 11: Phases (a) 6 and (b) 7 of static loadings.

boundary conditions. The model updating process typically consists of tuning some variables by using optimization algorithms and then automatic model updating using specialized software. Alternatively, manual tuning involves manual changes of the model geometry and modeling parameters by trial and error, guided by engineering judgment. Only manual tuning has been considered here since the model is linear elastic, and only few parameters have been tuned.

In order to apply this procedure, the structure has been subdivided into two substructures: one acting as main structure and the other acting as secondary structure useful only to distribute and transmit external loads to the main structure. Arches, stacks, abutments, and infilling of the piers (made of good-quality concrete) have been considered as structural parts (see Figure 5 for the different parts of the geometric model considered).

4.1. The Masonry

Mechanical properties of structural masonry have been evaluated by means of experimental tests (see Section 3.3). Therefore, during the model tuning, the values obtained in the above

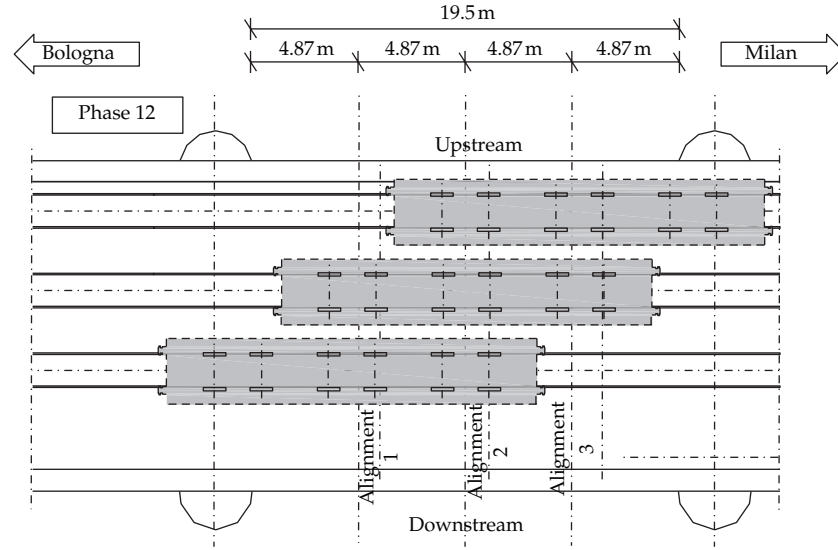


Figure 12: Phase 12 of static loading.

Table 1: Material properties.

Material	Young's modulus (MPa)	Poisson's ratio	Density (kg/m ³)
Structural parts			
Concrete	30000	0.20	2400
Masonry	8200	0.20	1800
Pillar infilling	20000	0.20	2400
Abutment	8200	0.20	2200
Nonstructural parts			
Infilling	100	0.20	1800
Ballast	100	0.20	2000
Masonry	820	0.20	1800
Interface	$E_1 = 8200$	—	—
	$E_2 = 820$	—	—
	$E_3 = 820$	—	—
	$G_{12} = 50$	—	—
	$G_{13} = 50$	—	—
	$G_{23} = 50$	—	—

tests have been used. In particular, a Young's modulus $E = 1000f_{mk} = 8.2 \text{ GPa}$ has been assumed, as suggested by Italian standards [19] starting from the experimental value of its compressive strength [15]. Other properties such as Poisson ratio and density have been introduced in the model by using conventional values taken from the literature, as well as for other materials not tested during the in situ survey (Table 1).

4.2. Model Calibration

The model calibration has been then performed according to results obtained during the static load tests and, in particular, using the load phase 4 (see Figure 9). Material properties of

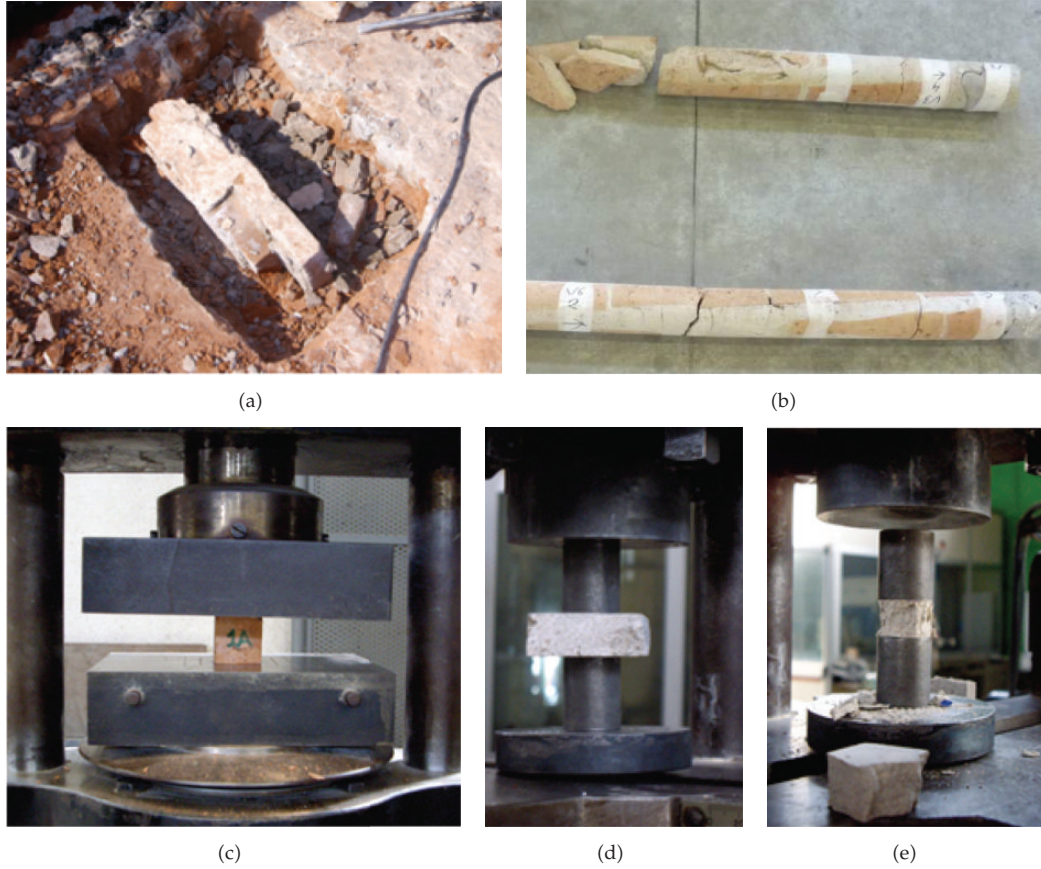


Figure 13: Sampling of a masonry portion from (a) the bridge arch barrel and from (b) the pillar; testing of (c) brick and (d)-(e) mortar specimens.

concrete and pillar infilling of the structural parts have been selected according to classical values from the literature (Table 1). Nonstructural parts have had the elasticity modulus selected according to their secondary role so that they cannot effectively contribute to the equilibrium of stresses produced by vertical loads. For this reason, the elasticity modulus has been chosen low enough to engender the quasilimitation of tensile stresses in these parts; see Table 1. Moreover, as anticipated in Section 2, much attention has been posed in the modelling of the interface between the newer and older parts of the bridge. In particular, the interface has been modelled using an orthotropic material whose mechanical properties are collected in Table 1 where “1” denotes the direction orthogonal to the contact surface between the two parts of the bridge and “2” the vertical direction. The results provided by the updated model are reported in Figure 14(a), where the comparison of the computed and measured vertical deflections is shown at the instruments locations.

4.3. Model Validation

Results provided by the other static load phases have been used to verify the reliability of the numerical model once updated. For the sake of brevity, only two load phases are reported here: results corresponding to load phases 3 and 12 are reported in Figures 14(b) and 14(c),

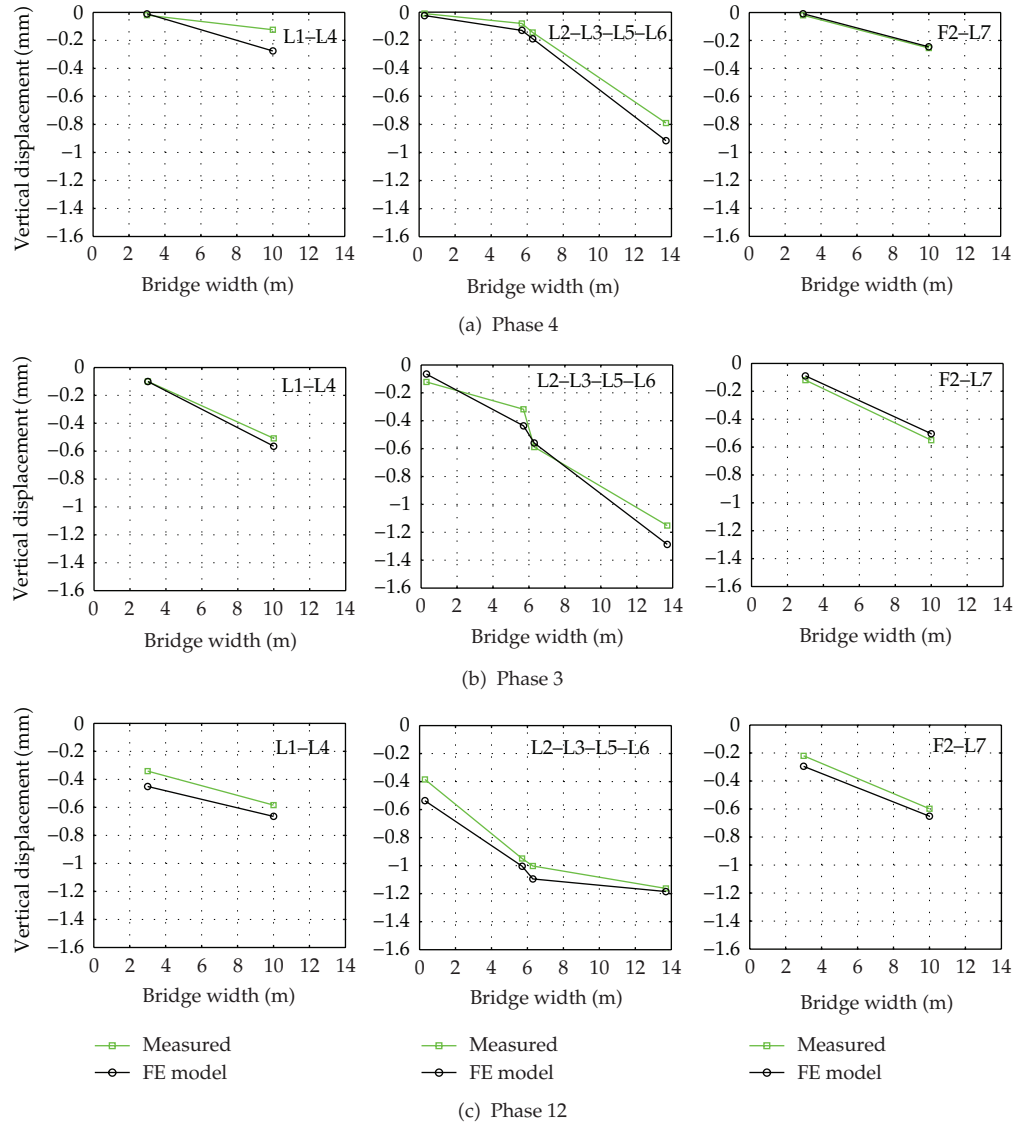


Figure 14: Comparison of the computed and measured vertical deflections at the LVDT locations.

respectively. Comparison shows a very good agreement between the numerical results and the experimental findings.

Moreover, as for the dynamic behavior of the structure, a modal analysis has been performed on the three-dimensional finite element model previously used for the static analysis. Characterization of the structural masses has been done by means of the data provided by the in situ survey and using data from the literature. Block Lanczos mode extraction method has been used to solve the eigenvalue problem [11]. Seventy mode shapes have been extracted and considered for the comparison. The first and fourth computed mode shapes are reported in Figures 15(a) and 15(b), respectively, along with the corresponding mode shapes identified by the in situ dynamic tests. Figures refer to the same span (the 4th span, C4) where experimental tests have been carried out.

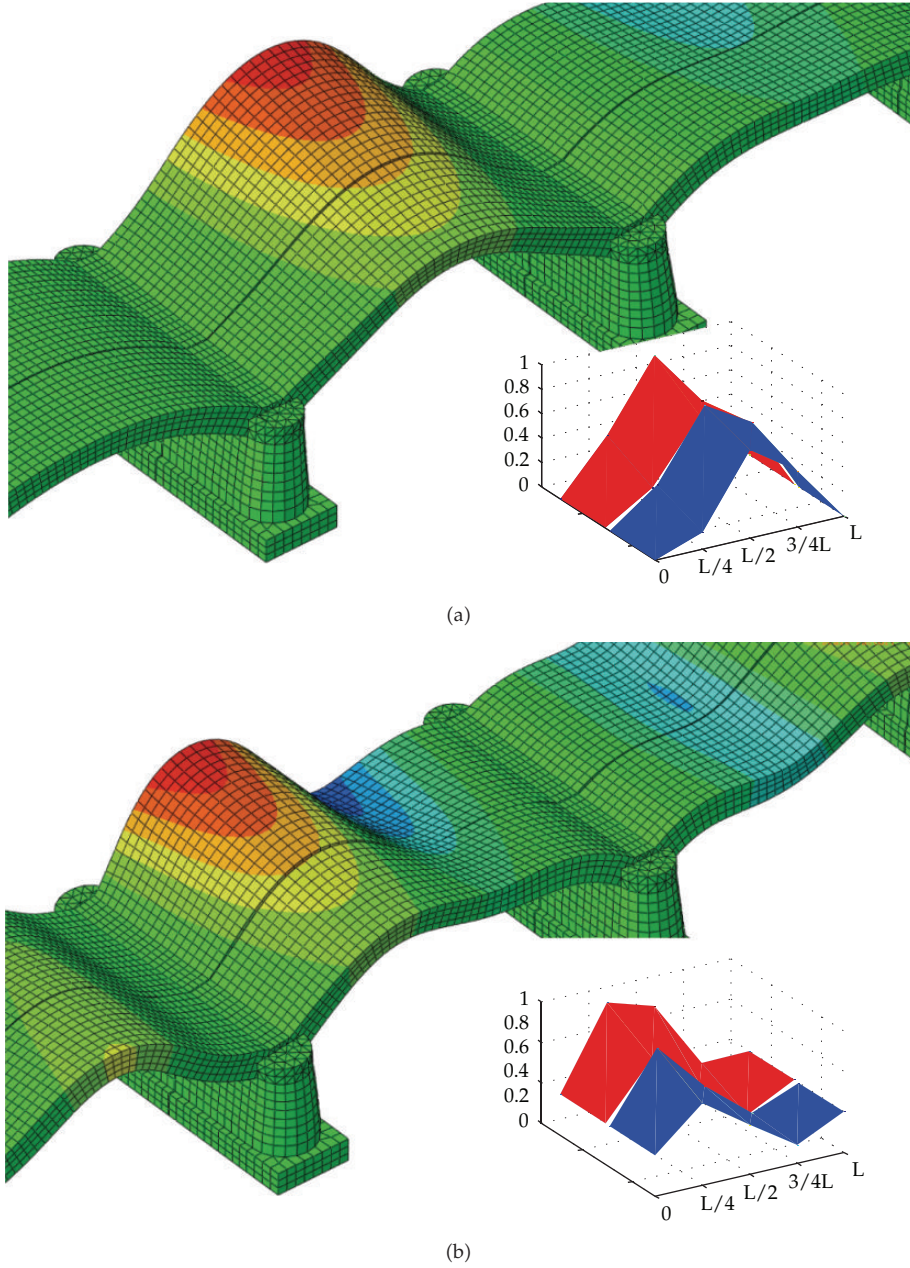


Figure 15: (a) First mode shape: freq = 9.35 Hz (numerical model), freq = 9.12 Hz (dynamic test); (b) Fourth mode shape: freq = 13.70 Hz (numerical model), freq = 14.1 Hz (dynamic test).

Colormap refers to the vertical displacement, as measured in situ. The numerical results are in very good agreement with the experimental ones although no model updating has been done on the structural masses.

The very good agreement between numerical and experimental results, obtained both in static and dynamic analyses, shows that the finite element model is reliable and could be employed to assess the structural health of the bridge.

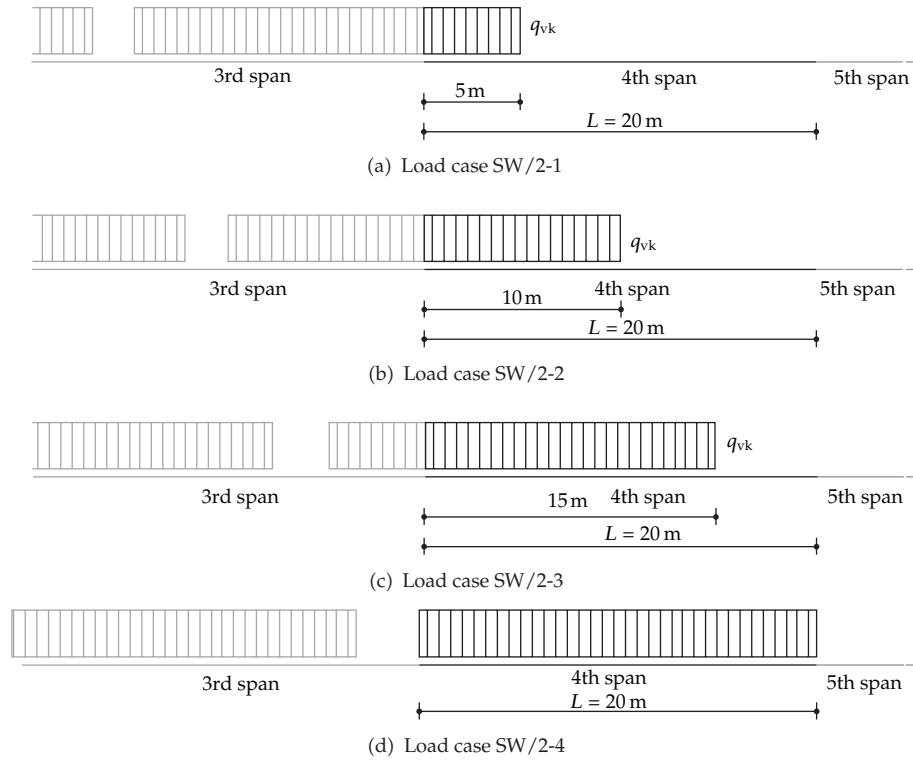


Figure 16: Load cases according to SW/2, $q_{vk} = 15 \text{ t/m}$.

Table 2: Material properties of the lightweight concrete.

Young's modulus (MPa)	Poisson's ratio	Density (kN/m^3)
23600	0.2	18

5. Bridge Structural Health Assessment

The finite element model described in the previous sections has been used to assess the structural health of the bridge both in its actual state and in the hypothesis of an intervention of structural strengthening. In particular, the strengthening intervention consists in the substitution of the actual fill material of the newer bridge (noncohesive) with lightweight concrete. The material properties for the lightweight concrete have been selected according to destructive experimental tests done on specimens; see Table 2. Indeed, the strengthening intervention is aimed at anchoring some tie rods to avoid the overturning of the spandrel wall. However, it can be interesting to evaluate its effect on the health of the whole structure.

The two railtracks on the newer part of the bridge (the part interested by the strengthening intervention, rails 3 and 4 in Figure 2) are loaded according to the load condition SW/2 (see par-5.2.2.3.1.2 of [19]). This load condition schematically represents the static effects due to heavy trains. In particular, four load cases are considered, corresponding to various phases of the passage of the trains on the 4th span; see Figure 16. Maximum values of the stress for the different load cases and for both the bridge in the actual state and in the hypothesis of the structural strengthening are collected in Table 3. Moreover, with reference to

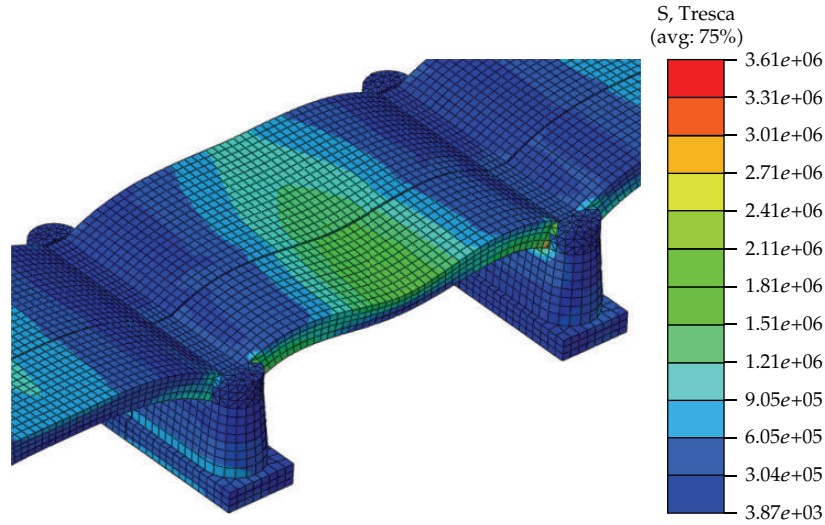


Figure 17: Resulting Tresca stress due to the load case SW/2-4 applied considering the actual state of the bridge.

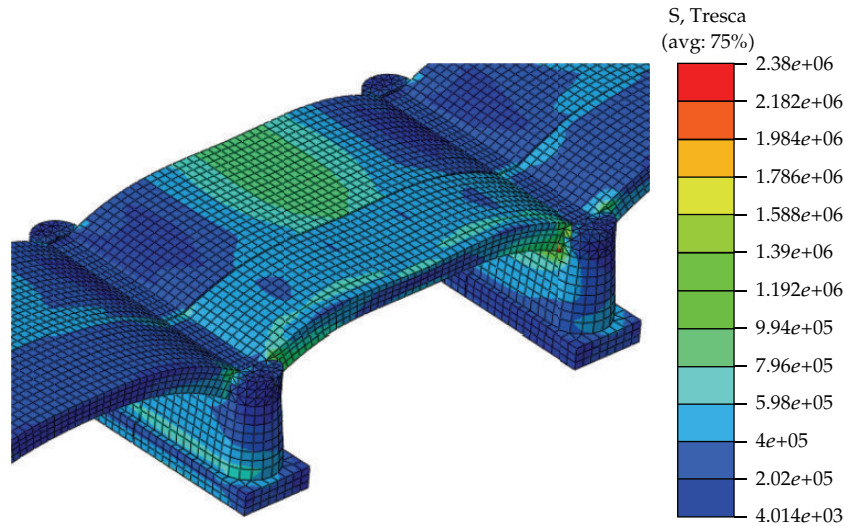


Figure 18: Resulting Tresca stress due to the load case SW/2-4 applied considering the structural strengthening of the bridge.

the load case SW/2-4, Figures 17 and 18 show the maps of the Tresca stress on the 4th span for the bridge in its actual state and in the hypothesis of the structural strengthening, respectively. Stress maps are obtained by means of standard shape functions, but values in Table 3 have been collected using the *quilt* visualization (one average value per element) in order to avoid the nonrealistic stress peaks that, in a displacement-based finite element model, characterize the stress distribution obtained via the elastokinematic relationship. A better evaluation of the stress distribution could be obtained by employing advanced postprocessing techniques [20, 21]. As it can be noted, in the actual state the stress level is quite low and far from the maximum strength of the masonry. Accordingly, the hypothesis of linear material behaviour done in setting up the finite element model can be considered reliable. Moreover, the low

Table 3: Maximum values of the stresses in the actual state and after the structural strengthening (MPa).

Load case	Actual state			After strengthening			
	Tresca	Min	Principal Max	Tresca	Min	Principal Max	Max
SW/2-1	1.81	−2.02	0.45	1.65	−1.85	0.50	
SW/2-2	2.62	−2.93	0.54	2.00	−2.24	0.65	
SW/2-3	2.95	−3.31	0.61	2.32	−2.60	0.80	
SW/2-4	3.00	−3.35	0.54	2.39	−2.69	0.79	

stress level indicates the absence of specific structural health alerts concerning the actual state of the bridge. Comparing the results of the actual state and after the strengthening intervention it is possible to observe that, as could be expected, the consolidation intervention engenders a lowering of the stress level. In particular, an average lowering of about 20% is obtained. In the presence of cyclic actions, like those due to the passages of the trains, this lowering of the stresses could have beneficial effects on the long-term structural health of the bridge [22].

6. Conclusions

The structural health assessment of the fifteen-span railway masonry arch bridge spanning over the Reno river in the city of Bologna Italy by finite element modelling and experimental testing has been presented. In particular, the finite element model has been tuned using the results of an experimental campaign involving static and dynamic load tests performed on the structure accompanied by some material testing performed on portions of masonry taken from the bridge. A part of the outcomes of the experimental campaign have been used to calibrate the finite element model and a part to validate it. A very good agreement between numerical and experimental results has been obtained, so confirming the underlying assumptions made in setting up the finite element model. Then, the finite element model has been used to evaluate the structural health of the bridge both in its actual state and in the hypothesis of a structural consolidation intervention. In all, the paper shows that the combination of experimental and numerical results is essential to reach a good level of knowledge when dealing with this kind of structures. Further developments regard the introduction of material nonlinearities in the finite element model, in order to evaluate the structural behavior also when ultimate limit state conditions occur. In this case, also seismic vulnerability analysis could be performed and a complete safety assessment developed.

References

- [1] A. Brencich and D. Sabia, "Experimental identification of a multi-span masonry bridge: the Tanaro Bridge," *Construction and Building Materials*, vol. 22, no. 10, pp. 2087–2099, 2008.
- [2] A. Brencich and U. De Francesco, "Assessment of multispan masonry arch bridges—I: simplified approach," *Journal of Bridge Engineering*, vol. 9, no. 6, pp. 582–590, 2004.
- [3] D. M. Armstrong, A. Sibbald, C. A. Fairfield, and M. C. Forde, "Modal analysis for masonry arch bridge spandrell wall separation identification," *NDT and E International*, vol. 28, no. 6, pp. 377–386, 1995.
- [4] C. Melbourne, T. G. Hughes, M. J. Blackler, and M. Gilbert, "A review of the UK masonry arch assessment methods. discussion," *Proceedings of the ICE*, vol. 134, no. 3, pp. 287–289, 1999.
- [5] A. Thavalingam, N. Bicanic, J. I. Robinson, and D. A. Ponniah, "Computational framework for discontinuous modelling of masonry arch bridges," *Computers and Structures*, vol. 79, no. 19, pp. 1821–1830, 2001.

- [6] C. Mazzotti, S. deMiranda, G. Castellazzi, and F. Carrea, "Structural assessment of the railway masonry arch bridge crossing the Reno river in Bologna," in *Proceedings of the 6th International Conference on Bridge Maintenance, Safety and Management*, pp. 1078–1085, 2012.
- [7] P. J. Fanning and T. E. Boothby, "Three-dimensional modelling and full-scale testing of stone arch bridges," *Computers and Structures*, vol. 79, no. 29-30, pp. 2645–2662, 2001.
- [8] P. J. Fanning, L. Sobczak, T. E. Boothby, and V. Salomoni, "Load testing and model simulations for a stone arch bridge," *Bridge Structures*, vol. 1, no. 4, pp. 367–378, 2005.
- [9] A. Bayraktar, A. C. Altuniik, F. Birinci, B. Sevim, and T. Türker, "Finite-element analysis and vibration testing of a two-span masonry arch bridge," *Journal of Performance of Constructed Facilities*, vol. 24, no. 1, pp. 46–52, 2010.
- [10] B. Sevim, A. Bayraktar, A. C. Altuniik, S. Atamtürkür, and F. Birinci, "Finite element model calibration effects on the earthquake response of masonry arch bridges," *Finite Elements in Analysis and Design*, vol. 47, no. 7, pp. 621–634, 2011.
- [11] Hibbitt Inc., *Abaqus Theory Manual*, Karlsson & Sorensen, 1998.
- [12] G. Castellazzi, "On the performances of parametric finite elements when geometry distortions occur," *Finite Elements in Analysis and Design*, vol. 47, no. 12, pp. 1306–1314.
- [13] R. J. Allemang and D. L. Brown, "A unified matrix polynomial approach to modal identification," *Journal of Sound and Vibration*, vol. 211, no. 3, pp. 301–318, 1998.
- [14] D. J. Ewins, *Modal Testing: Theory, Practice and Application*, Wiley, 2nd edition, 2001.
- [15] E. Sassoni and C. Mazzotti, "The use of small diameter cores for assessing the compressive strength of clay brick masonries," *Journal of Cultural Heritage*. In press.
- [16] Eurocode 6, "Part 1-1, General Rules for reinforced and unreinforced masonry, including lateral loading," 2009.
- [17] C. Gentilini, L. Govoni, S. de Miranda, and G. Gottardi, "Three-dimensional numerical modelling of falling rock protection barriers," *Computers and Geotechnics*, vol. 44, pp. 58–72, 2012.
- [18] L. Govoni, S. de Miranda, C. Gentilini, G. Gottardi, and F. Ubertini, "Modelling of falling rock protection barriers," *International Journal of Physical Modelling in Geotechnics*, vol. 11, pp. 126–137, 2011.
- [19] NTC 2008, "Norme Tecniche per le Costruzioni," D.M. 14/01/08, 2008.
- [20] G. Castellazzi, S. de Miranda, and F. Ubertini, "Adaptivity based on the recovery by compatibility in patches," *Finite Elements in Analysis and Design*, vol. 46, no. 5, pp. 379–390, 2010.
- [21] S. de Miranda, L. Patruno, and F. Ubertini, "Transverse stress profiles reconstruction for finite element analysis of laminated plates," *Composite Structures*, vol. 94, no. 9, pp. 2706–2715, 2012.
- [22] C. Carloni, K. V. Subramaniam, M. Savoia, and C. Mazzotti, "Experimental determination of FRP-concrete cohesive interface properties under fatigue loading," *Composite Structures*, vol. 94, no. 4, pp. 1288–1296, 2012.

Research Article

Fractal Dimension Analysis of Higher-Order Mode Shapes for Damage Identification of Beam Structures

**Runbo Bai,^{1,2} Maosen Cao,^{2,3} Zhongqing Su,⁴
Wiesław Ostachowicz,³ and Hao Xu⁴**

¹ Department of Engineering Mechanics, College of Water-Conservancy and Civil Engineering, Shandong Agricultural University, Taian 271000, China

² Department of Engineering Mechanics, Hohai University, Nanjing 210098, China

³ Institute of Fluid Flow Machinery, Polish Academy of Sciences, 80-952 Gdańsk, Poland

⁴ Department of Mechanical Engineering, The Hong Kong Polytechnic University, Hung Hom, Kowloon, Hong Kong

Correspondence should be addressed to Maosen Cao, mmcao@imp.gda.pl

Received 23 April 2012; Accepted 27 June 2012

Academic Editor: Ivan Bartoli

Copyright © 2012 Runbo Bai et al. This is an open access article distributed under the Creative Commons Attribution License, which permits unrestricted use, distribution, and reproduction in any medium, provided the original work is properly cited.

Fractal dimension analysis is an emerging method for vibration-based structural damage identification. An unresolved problem in this method is its incapability of identifying damage by higher-order mode shapes. The natural inflexions of higher-order mode shapes may cause false peaks of high-magnitude estimates of fractal dimension, largely masking any signature of damage. In the situation of a scanning laser vibrometer (SLV) providing a chance to reliably acquire higher-order (around tenth-order) mode shapes, an improved fractal dimension method that is capable of treating higher-order mode shapes for damage detection is of important significance. This study proposes a sophisticated fractal dimension method with the aid of a specially designed affine transformation that is able to obviate natural inflexions of a higher-order mode shape while preserving its substantial damage information. The affine transformed mode shape facilitates the fractal dimension analysis to yield an effective damage feature: fractal dimension trajectory, in which an abruptly rising peak clearly characterizes the location and severity of the damage. This new fractal dimension method is demonstrated on multiple cracks identification in numerically simulated damage scenarios. The effectiveness of the method is experimentally validated by using a SLV to acquire higher-order mode shapes of a cracked cantilever beam.

1. Introduction

Structure health monitoring and damage detection using vibrational characteristics have been a research topic in the aerospace, mechanical, and civil fields for last decades [1, 2]. In this area of research, various damage detection methods have been developed from modal

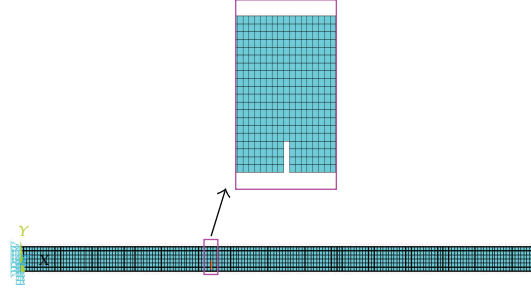


Figure 1: Numerical model of a cantilever beam with a single-edge crack described by $a = 0.2$ and $\beta = 0.4$ (Damage Scenario I).

parameters [3] such as natural frequency, mode shape [4], and mode damping. Among these parameters, it is commonly acknowledged that natural frequency has low sensitivity to small damage, mode damping is fairly difficult to acquire, and mode shape has the best potential to characterize damage [5]. Based on mode shape and its derivatives, a series of damage methods have been developed, most typically modal assurance criterion (MAC) [2], modal curvature and strain energy mode shape [6]. Nevertheless, some limitations in methods based on mode shapes have gradually been recognized; the most noteworthy of which is the lack of appropriate means to extract quantitative damage features from mode shapes [7]. In recent years, several new mathematical theories, for example, wavelet transform [8] and fractal dimension (FD) analysis [9] have been used to cope with mode shapes for identifying features of damage. In particular, FD analysis has attracted much attention in the field of structural damage detection.

FD analysis has become a burgeoning tool to provide insight into mode shapes for detecting damage [10–13]. The underlying principle of treating damage can be described as [10] follows: damage induces changes to the dynamic properties of a structure, consequently causing irregularity of local mode shape; moreover, this irregularity can be characterized by an abrupt peak composed of high-magnitude estimates of FD, with the position and magnitude of the peak indicating the location and severity of the damage in a quantitative fashion. The efficacy of FD damage detection has been proved in many investigations. Hadjileontiadis et al. [10] utilized a moving window to successively cover the fundamental mode shape of a cantilever beam and calculate FD from the sampling points covered by the window, leading to a pointwise FD trajectory along the mode shape. In the trajectory, an abnormal peak composed of high-magnitude FD estimates reflects an irregularity of the local mode shape, indicating the location and severity of the damage. Li et al. [11] applied the FD to the first mode shape of simply supported steel beams with saw-cut cracks at different locations, and the results show the cracks were rightly identified. Shi et al. [12] implemented the FD analysis on the static deformation profile of one-crack and two-crack cantilever beam-type specimens and got satisfactory results of crack identification. The patulous application of the method to the fundamental two-dimensional (2D) mode shape of a simply supported cracked rectangular plate was investigated for damage identification by [5], where a 2D FD surface rather than a FD trajectory was available, and the peak in the surface predicted the location and quantification of the crack in the plate [14].

Most existing studies of FD damage detection are related to the fundamental mode shapes of beam-type structures due to their slight fluctuation in configuration and ease of measurement, but the application of the method to higher-order mode shapes is an interesting

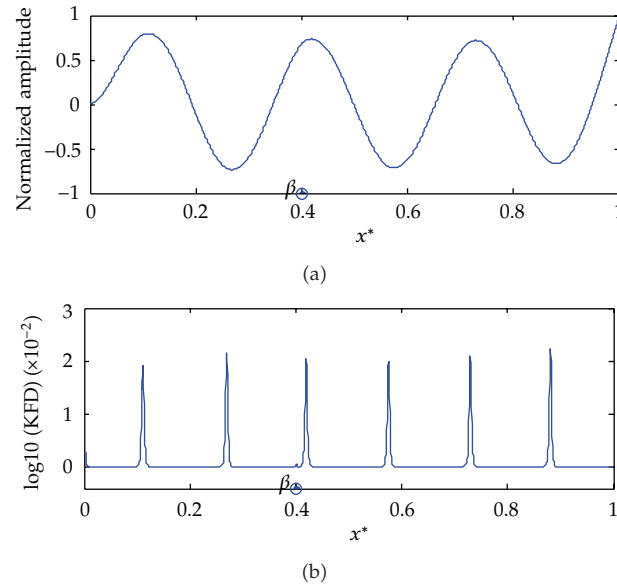


Figure 2: Seventh-order mode shape (a) and associated KFD trajectory (b) for Damage Scenario I (where x^* denotes the normalized x -coordinate).

Table 1: Damage scenarios used in simulation.

Damage Scenario	I	II	III	IV
Order of mode	7th	9th	11th	13th
Crack severity	$a = 0.2$	$a = 0.2$	$a = 0.2$	$a = 0.2$
Crack location	$\beta = 0.4$	$\beta = 0.75$	$\beta_1 = 0.3, \beta_2 = 0.7$	$\beta_1 = 0.2, \beta_2 = 0.6, \beta_3 = 0.8$

issue that is still unresolved well [15]. Several studies have addressed the limitations of FD in treating higher-order mode shapes to reveal damage [16, 17]. The crucial point is that natural inflexions in a higher-order mode shape, as identified by the zero values of slope at those points, can create prominent false peaks in the FD trajectory [15], easily distorting the results of damage identification. Some studies have attempted to circumvent this problem that has been frustrating the use of FD in structural damage detection. Typically, Wang and Qiao [16] proposed a generalized fractal dimension method (GFD) with a flexible parameter to exaggerate the values of the x -coordinate of beam length, capable of detecting damage from the first three mode shapes of a cantilever beam. Qiao and Cao [17] proposed an approximate waveform capacity dimension (AWCD) and developed a regime of topological isomorphism to enable AWCD to reveal damage relying on the first three mode shapes of cantilever beams. Unfortunately, these methods have some imperfections in coping with higher-order mode shapes largely beyond the first three mode shapes. These higher-order mode shapes are hereinafter referred to as “around tenth-order” mode shapes. When encountering such a mode shape, these methods are usually inadequate to eliminate inflexion-induced false peaks in FD trajectory, and these false peaks are likely to mask any signature of damage.

Nowadays, it has become important to improve FD for damage detection on the basis of higher-order mode shapes. There are three reasons: (1) fractal theory has enormous potential to quantitatively characterize local irregularities or abnormalities of a mode shape;

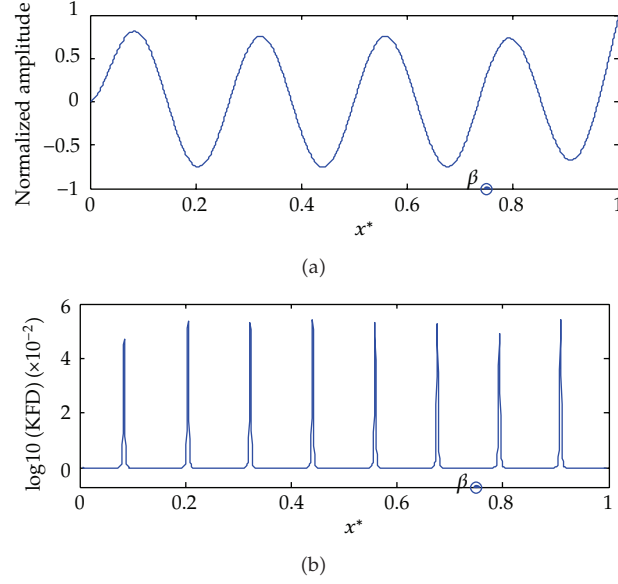


Figure 3: Ninth-order mode shape (a) and associated KFD trajectory (b) for Damage Scenario II (where x^* denotes the normalized x -coordinate).

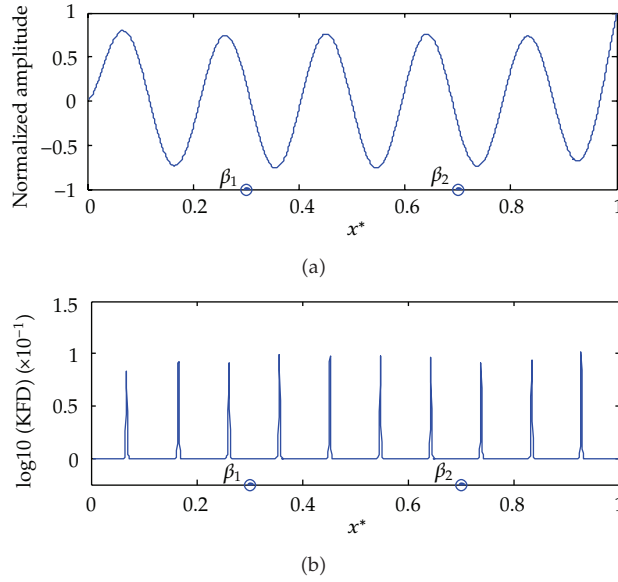


Figure 4: Eleventh-order mode shape (a) and associated KFD trajectory (b) for Damage Scenario III (where x^* denotes the normalized x -coordinate).

(2) acquisition of around tenth-order mode shapes can be accurately achieved by modern experimental equipments, for example, scanning laser vibrometer (SLV); (3) higher-order mode shapes potentially convey richer damage information than lower-order ones. Given these conditions, this study aims to explore a sophisticated FD method that is capable of

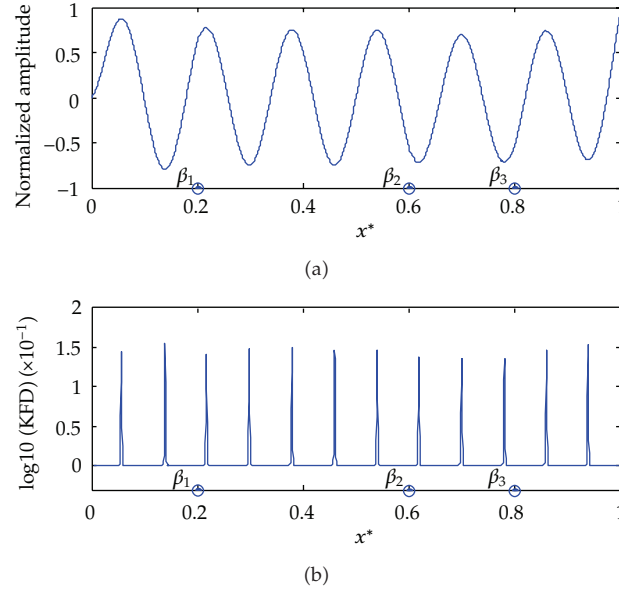


Figure 5: Thirteenth-order mode shape (a) and associated KFD trajectory (b) for Damage Scenario IV (where x^* denotes the normalized x -coordinate).

tackling higher-order mode shapes for damage identification by overcoming the drawbacks of existing methods.

The organization of this paper is as follows. After this introduction, Section 2 examines the major deficiencies in existing FD methods for dealing with higher-order mode shapes to reveal damage. Section 3 presents a specially elaborated affine transformation that can convert a higher-order mode shape to a renascent one by preserving the substantial topological properties while eliminating the inflexions of the original mode shape. Section 4 provides a new FD method based on affine transform that is capable of characterizing damage using higher-order mode shapes. The proof-of-concept validation of the proposed method is given in Section 5, following which its effectiveness in damage identification in actual structures is experimentally investigated by using SLV to acquire the higher-order mode shapes.

2. Fundamentals

2.1. Fractal Dimension

The fractal dimension can be seen as a measure of the complexity of signals [18]. As a particular fractal dimension, the waveform fractal dimension is appropriate for characterizing the complexity of two-dimensional waveform signals [9]. Among the various waveform fractal dimensions available [18–22], the Katz's fractal dimension (KFD) [9] is probably the most commonly used due to its simplicity of concept and facilitation in computer implementations. Without loss of generality, the KFD is adopted in this study, and the method developed is applicable to other waveform fractal dimensions, for example, AWCD in [17].

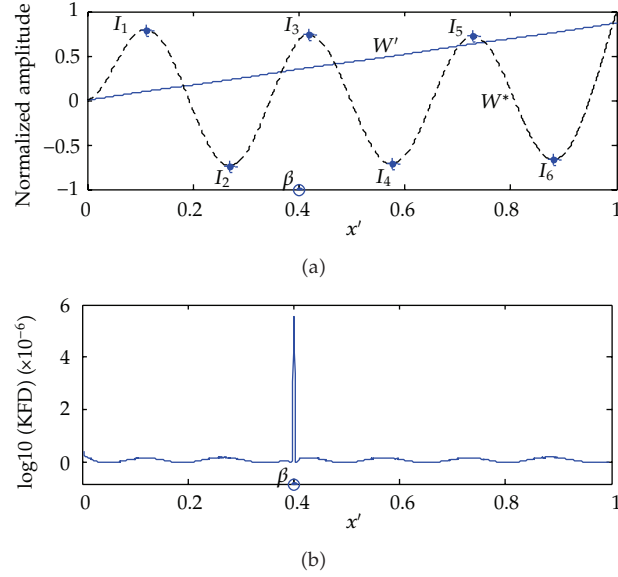


Figure 6: Effect of affine transformation on crack identification illustrated on the seventh-order mode shape for Damage Scenario I. (a) Affine transformed mode shape W' and its original counterpart W^* ; (b) KFD trajectory showing a singular peak attributed to the crack.

The KFD of a two-dimensional waveform signal is defined by [9]

$$\text{KFD} = \frac{\log_{10}(n)}{\log_{10}(n) + \log_{10}(d/L)}, \quad (2.1)$$

where n denotes the number of increments between adjacent sampling points of the signal under investigation, $d = \max \text{dist}(1, i)$, the maximum distance between the beginning point, and the i th point of the sampling sequence under investigation and L is the sum of distances between successive points.

Although the KFD has been successfully applied to lower-order mode shapes for damage identification, its application to higher-order mode shapes is still somewhat problematic. To facilitate description of the problems, a numerical model of a cantilever beam with various crack scenarios is given in the following.

2.2. A Cracked Beam Model

A beam, 1 m long (L), 0.02 m wide (B), and 0.02 m thick (H), is considered. The material data used are Young's modulus $E = 70 \text{ GPa}$ and density $\rho = 2700 \text{ kg/m}^3$. The numerical beam samples are built using 4-node 2D structural solid elements (PLANE42) in the commercial software ANSYS. The real constants are set by KEYOPT (3) = 3 to specify the width of the elements. The numerical model of beams consists of two-thousand finite elements. The crack is described by two parameters: relative depth ratio (RDR), $a = h_c/H$, and relative location ratio (RLR), $\beta = L_c/L$, with h_c and L_c being the crack depth and crack location away from

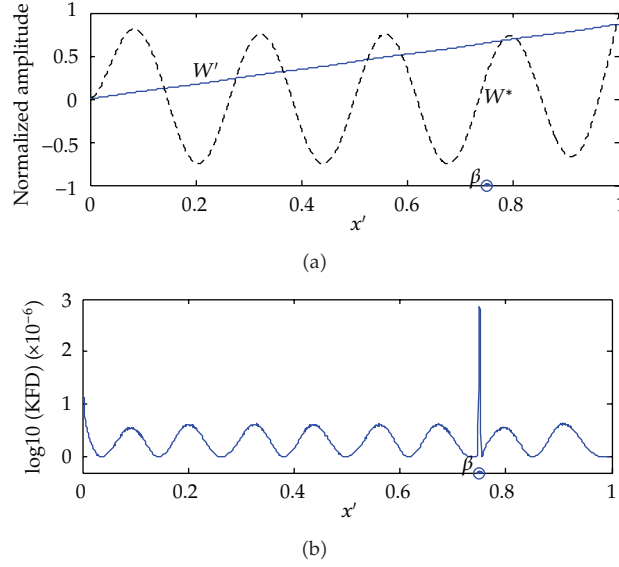


Figure 7: Crack identification on the ninth-order mode shape for Damage Scenario II. (a) Affine transformed mode shape W' and its original counterpart W^* ; (b) KFD trajectory showing a singular peak attributed to the crack.

the clamped end, respectively. Each crack is modeled by reducing the thickness of the cross-section of a tiny segment of the beam, and various crack scenarios elaborated by adjusting parameters RDR and/or RLR are listed in Table 1. Figure 1 illustrates the finite element mesh of the cracked beam for Damage Scenario I described by $a = 0.2$ and $\beta = 0.4$, for which the manipulation of modal analysis can be adopted to generate higher-order mode shapes.

2.3. Damage Feature: FD Trajectory

A mode shape of a beam can be viewed as a particular two-dimensional waveform signal. The general procedure for applying the FD to a mode shape for damage detection is summarized as follows. A window with a fixed size, commonly containing a few sampling points, is utilized to cover the mode shape, and from the sampling points covered, an estimate of FD is evaluated and assigned at the midpoint of the window. This estimate quantitatively indicates the complexity of the window-covered segment of the mode shape. As the window slides point by point from the left to the right-hand end of a mode shape, an FD trajectory made up of a sequential of estimates appears. This FD trajectory represents a profile of the pointwise complexities of the mode shape. Damage causes increased irregularity or complexity of a local mode shape, manifested by high-magnitude estimates of FD, so a peak arising abruptly in the FD trajectory can predict the location and quantification of the damage. Thus, the FD trajectory can serve as a damage feature indicating the location and severity of the damage.

In this study, according to combined effects of sampling density and noise intensity, the sliding window is set to satisfy the following condition: covering 12 sampling points for a numerical mode shape and containing 10 sampling points for an experimental mode shape.

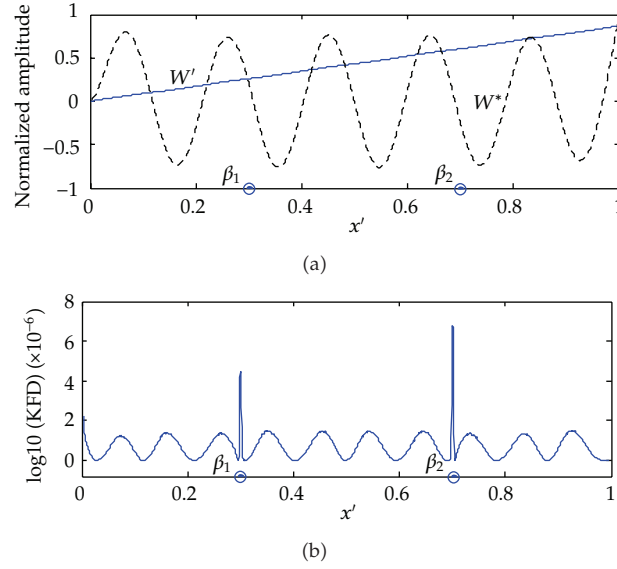


Figure 8: Crack identification on the eleventh-order mode shape for Damage Scenario III. (a) Affine transformed mode shape W' and its original counterpart W^* ; (b) KFD trajectory showing two singular peaks attributed to the cracks.

2.4. Deficiencies of FD with Higher-Order Mode Shapes

As aforementioned, most successful applications of FD, for example, KFD, GFD, and AWCD, in damage detection are related to lower-order mode shapes [10–12], but the use of FD with higher-order (around tenth-order) mode shapes poses a challenge for existing FD methods. The crucial problem is that the inflexions, as illustrated in Figure 2(a), of higher-order mode shapes can cause false peaks of high-magnitude FD estimates, regardless of damage, which masks the genuine peak attributed to damage. For instance, regarding the seventh-order mode shape of the cracked beam model for Damage Scenario I, the negative effect of inflexion-induced false peaks in the KFD trajectory on damage characterization is illustrated in Figure 2, where the logarithm of KFD to base 10 is used in the y -coordinate for clarity in presentation. Clearly, the false peaks inflexions almost overwhelm the real peak attributed to the damage. This example illustrates the common problem of applying FD to higher-order mode shapes for damage detection. To further address this point, similar results concerning ninth-, eleventh-, and thirteenth-order mode shapes associated to Damage Scenarios II, III, and IV are shown in Figures 3, 4, and 5, respectively. This inapplicability of FD to higher-order mode shapes for depicting damage limits the effectiveness of FD analysis in the field of structural damage detection.

3. Affine Transformation of Higher-Order Mode Shapes

3.1. Affine Transformation

An affine transformation [23] is mathematically defined as a transformation that preserves substantial topological properties such as collinearity (i.e., points on a line prior to the

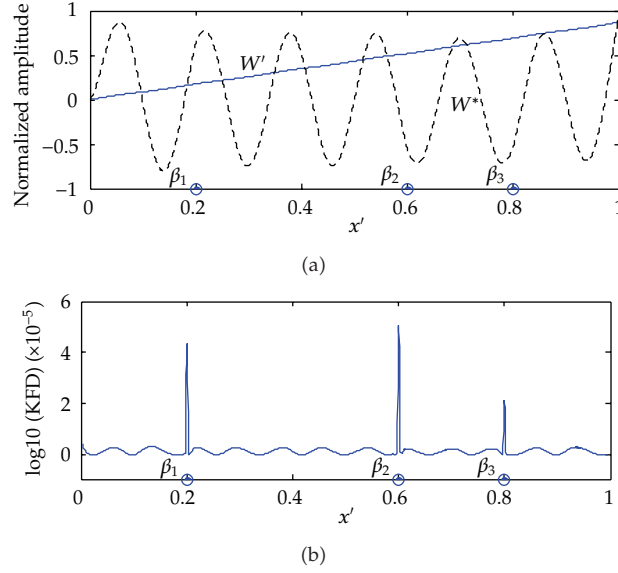


Figure 9: Crack identification on the thirteenth-order mode shape for Damage Scenario IV. (a) Affine transformed mode shape W' and its original counterpart W^* ; (b) KFD trajectory showing three singular peaks attributed to the cracks.

transformation will lie on the line after the transformation), ratios of distances (i.e., proportions in lines are conserved by the transformation), and intersections of lines (i.e., an intersection of several lines will remain an intersection after the transformation despite probably changed angles between any pair of lines). Translation, reflection, expansion, shear, geometric contraction, dilation, rotation, similarity transformations, and spiral similarities are all affine transformations, as are their combinations [24].

For a two-dimensional point (x, y) of an arbitrary waveform, its affine transformation can be carried out by means of premultiplying its homogeneous coordinates $(x, y, 1)$ by an affine transformation matrix \mathbf{A} , expressed as

$$\begin{Bmatrix} x' \\ y' \\ 1 \end{Bmatrix} = \mathbf{A} \begin{Bmatrix} x \\ y \\ 1 \end{Bmatrix}, \quad \mathbf{A} = \begin{bmatrix} c_{11} & c_{12} & c_{13} \\ c_{21} & c_{22} & c_{23} \\ 0 & 0 & 1 \end{bmatrix}. \quad (3.1)$$

In matrix \mathbf{A} , c_{11} and c_{22} are the scaling coefficients, c_{12} and c_{21} the shear coefficients, and c_{13} and c_{23} the translation coefficients. The affine transformation of a higher-order mode shape as a particular waveform gives rise to a resurgent mode shape that preserves collinearity, ratios of distances and intersections but might alter the configuration of the original mode shape. Such properties of preservation and alteration of affine transformation are useful to retain damage content while obviating the inflexions of the original mode shape.



(a) Experimental setup

(b) Zoomed-in section showing excitation using an electromechanical shaker

Figure 10: Experimental measurement of mode shapes of cracked cantilever beam using SLV.

3.2. Normalization of Higher-Order Mode Shapes

In general, a higher-order mode shape is in the form of a sampling sequence, $\mathbf{W} = \{x_i, y_i\}_{i=1}^n$, where x_i is the i th sampling abscissa along the beam length, y_i the amplitude of the mode shape at x_i , and n the number of samplings. In physics, mode shape is a dimensionless quantity such that $\mathbf{W}^c = \{x_i, cy_i\}$, with c being an arbitrary nonzero constant, has the same physical implication as \mathbf{W} ; in contrast, in geometry \mathbf{W}^c is a distinctive waveform from \mathbf{W} such that it has different FD estimate from the latter, and hence there are probably nonunique FD characteristics for the same damage. It is necessary, therefore, to normalize a mode shape to reach a sole waveform, resulting in a unique FD characteristic to reflect damage. The method of normalization is expressed as

$$x_i^* = \frac{x_i}{\max(\{x_i\}_{i=1}^n)}, \quad y_i^* = \frac{y_i}{\max(\{|y_i|\}_{i=1}^n)}, \quad (3.2)$$

where x_i^* is the i th sampling abscissa of the normalized mode shape and y_i^* is the amplitude at x_i^* . After normalization, the original mode shape \mathbf{W} yields a normalized mode shape $\mathbf{W}^* = \{x_i^*, y_i^*\}_{i=1}^n$.

3.3. Affine Transformation for Higher-Order Mode Shapes

To obviate the inflexions of $\mathbf{W}^* = \{x_i^*, y_i^*\}_{i=1}^n$, a specific affine transformation matrix, \mathbf{A}' , should be activated. The matrix \mathbf{A}' is built by using the elements $c_{11} = 1$, $c_{21} = \sin \theta$,

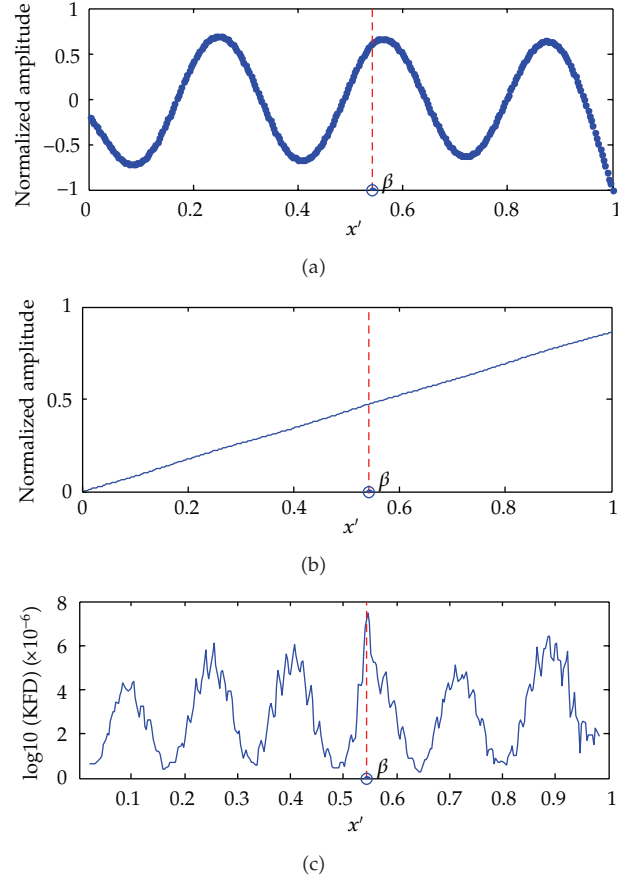


Figure 11: Experimental crack identification from SLV-measured seventh-order mode shape of cracked cantilever beam. (a) Normalized seventh-order mode shape; (b) affine transformed mode shape; (c) KFD trajectory showing a singular peak attributed to the crack.

$c_{22} = (\cos \theta)/k$, $c_{12} = c_{13} = c_{23} = 0$ to specialize the ordinary affine transformation matrix, \mathbf{A} , in (3.1), giving:

$$\begin{Bmatrix} x'_i \\ y'_i \\ 1 \end{Bmatrix} = \mathbf{A}' \begin{Bmatrix} x_i^* \\ y_i^* \\ 1 \end{Bmatrix}, \quad \mathbf{A}' = \begin{bmatrix} 1 & 0 & 0 \\ \sin \theta & (\cos \theta)/k & 0 \\ 0 & 0 & 1 \end{bmatrix}. \quad (3.3)$$

In matrix \mathbf{A}' , $(\cos \theta)/k$ is the scaling coefficient for y_i^* , and $\sin \theta$ is the shear coefficient parallel to y_i^* . k and θ are adjustment parameters for the scaling and shear coefficients, respectively. There are wide definition domains for k and θ to satisfy the condition of obviating the inflexions of higher-order mode shapes. The flexibility in setting k and θ is a distinctive feature of this affine transformation that makes it superior to other types of transformation. In this study, $k = 100$ and $\theta = 60^\circ$ are arbitrarily assigned to frame a specific affine transformation adopted for all higher-order mode shapes arising from both numerical and experimental damage cases. Based on this affine transformation, the normalized mode shape \mathbf{W}^*

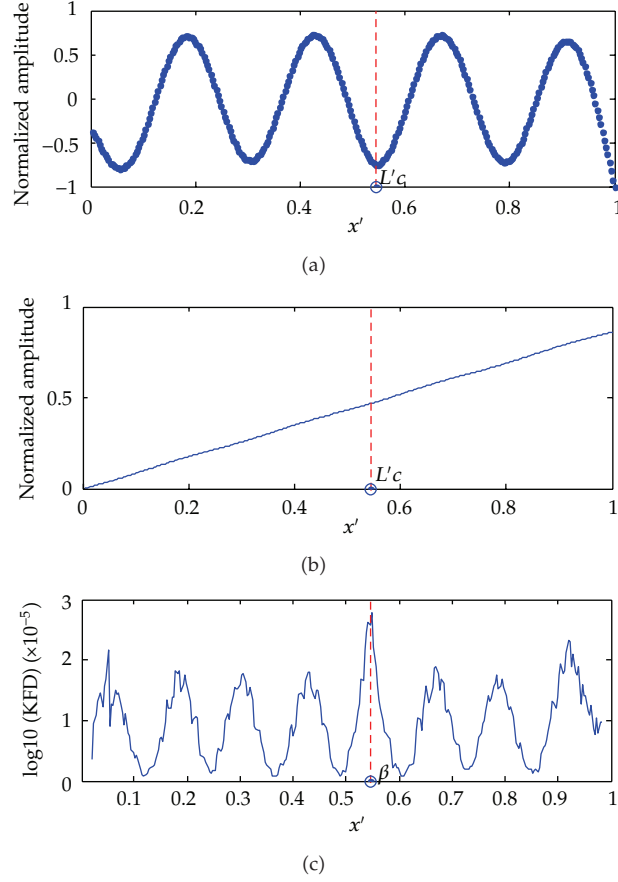


Figure 12: Experimental crack identification from SLV-measured ninth-order mode shape of cracked cantilever beam. (a) Normalized ninth-order mode shape; (b) affine transformed mode shape; (c) KFD trajectory showing a singular peak attributed to the crack.

creates a renascent mode shape $\mathbf{W}' = \{x'_i, y'_i\}_{i=1}^n$ that preserves the damage information but eliminates its inflexions in \mathbf{W}^* .

By way of illustration, the proposed affine transformation is applied to the seventh-order mode shape shown in Figure 2(a), and the result is presented in Figure 6(a). In the figure, the normalized mode shape, \mathbf{W}^* , indicated by a dotted line, gives rise to an affine transformed mode shape, \mathbf{W}' , designated by a solid line. It can be clearly observed that the six inflexions in \mathbf{W}^* from \mathbf{I}_1 to \mathbf{I}_6 are unavailable in \mathbf{W}' , and thus \mathbf{W}' can potentially serve as a reasonable alternative to \mathbf{W}^* for use in damage identification. After the KFD analysis is carried out on \mathbf{W}' , the resulting KFD trajectory shown in Figure 6(b) is produced. In the trajectory, a prominent peak, without interference from false peaks arising from inflexions, clearly indicates the location and severity of the crack. When the KFD trajectory in Figure 6(a) is compared to that from the original mode shape (Figure 2(b)), it can be concluded that the affine transformation significantly improves the performance of the FD methods for analyzing mode shapes for damage identification.

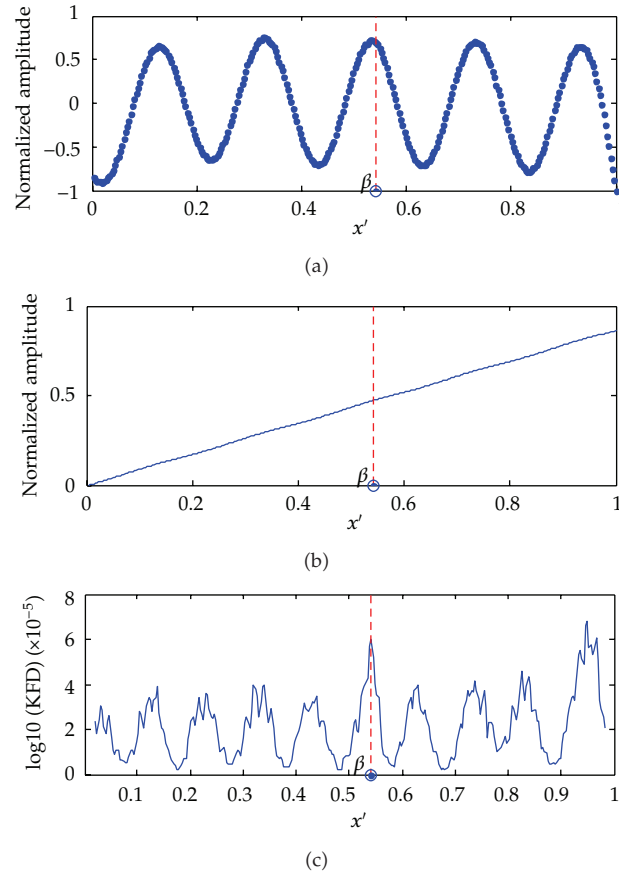


Figure 13: Experimental crack identification from SLV-measured eleventh-order mode shape of cracked cantilever beam. (a) Normalized eleventh-order mode shape; (b) affine transformed mode shape; (c) KFD trajectory showing a singular peak attributed to the crack.

4. Concept-of-Proof Validation

The previous analysis implies that the affine transformation-based FD analysis is a sophisticated method for detecting damage in beam-type structures. This method consists of three basic components: normalization, affine transformation, and FD analysis. The normalization described in (3.2) first runs on a higher-order mode shape acquired numerically or experimentally, giving rise to a normalized mode shape. Then the affine transformation given in (3.3) is employed to convert the normalized mode shape into a renascent mode shape, and finally the FD analysis is carried out on the renascent mode shape to yield an FD trajectory acting as a damage feature. The method is highlighted by the function of affine transformation to produce a new mode shape free of inflexions, offering a decent platform for the FD analysis to effectively reveal damage.

As a concept-of-proof validation, the proposed method is applied to Damage Scenarios II, III, and IV in Table 1, and the results are presented in Figures 7, 8, and 9, respectively. In Figures 7(a)–9(a), the normalized mode shapes and affine transformed mode shapes are marked by dotted and solid lines, respectively. In each figure, it is evident that the affine

transformation obviates the inflexions of higher-order mode shapes dramatically. After the KFD analysis on the affine transformed mode shapes, the KFD trajectories are obtained, as shown in Figures 7(b)–9(b), respectively. In each figure, the predominant peaks, free of interference, clearly indicate the location and quantification of the cracks. When Figures 2–5 are compared to Figures 6–9 for all Damage Scenarios listed in Table 1. It is concluded that the proposed method has strong capability to identify damage using higher-order mode shapes.

5. Experimental Investigations

The affine transformation-based FD analysis method for damage identification is experimentally investigated using a scanning laser vibrometer (SLV) to acquire higher-order mode shapes. A cantilever beam (aluminum 6061) of length (L) 543 mm, width (B) 30 mm, and height (H) 8 mm is considered, as shown in Figure 10. A through-width crack, 1.2 mm long (along beam span) and 2 mm deep ($a = 25\%$), located 293 mm ($\beta = 54\%$) away from the clamped end, is introduced into the beam. An out-of-plane monofrequency excitation at certain higher-order modal frequency, along z -direction at a point 525 mm from the clamped end, is applied by an electromechanical shaker (B&K 4809). The selection of excitation frequency is based on a preliminary frequency response function (FRF) analysis. In the beam, out-of-plane velocities at all measurement points along the central line of the beam (evenly distributed with a spacing interval of 2.3 mm) are captured from the intact surface of the beam, opposite to the surface where the damage is located, using an SLV (Polytec PSV-400). The experimental setup is photographed in Figure 10. The captured velocities are integrated to achieve the displacement responses of the beam using a FAST-SCAN function of the SLV.

To present a comprehensive insight into the capability of actual damage detection for the proposed method, the original experimental data free of any preprocessing, for example, denoising, are considered. The seventh-, ninth-, and eleventh- order mode shapes acquired by the SLV, after normalization, are presented in Figures 11(a), 12(a), and 13(a), respectively, and the associated affine transformed mode shapes are shown in Figures 11(b), 12(b), and 13(b), respectively. From the affine transformed mode shapes, the KFD trajectories are presented in Figures 11(c), 12(c), and 13(c) respectively. It can be observed from each KFD trajectory that the prominent peak of high-magnitude KFD values accurately indicates the location and quantification of the crack in the beam.

6. Conclusions

Fractal dimension (FD) analysis of mode shapes for damage identification is a new and potential research area. Despite the many advantages addressed in existing studies, the limitation of its inability to extract damage features from higher-order mode shapes is fairly noticeable. This fundamental study introduces an affine transformation to improve the existing FD method for damage identification, leading to a more sophisticated method. This method features the dramatic action of affine transformation in eliminating the inflexions of higher-order mode shapes, underpinning the FD analysis to competently reveal damage. The concept of proof of the method is demonstrated by numerical simulations; its effectiveness is further validated in experimental cases of cracked beams using a scanning laser vibrometer (SLV) to acquire higher-order mode shapes. The robustness against noise of the proposed method, the optimal selection of systematic parameters, and expansion to plate-type structures will be further investigated in future studies.

Acknowledgments

M. Cao and W. Ostachowicz are grateful to a Marie Curie Industry Academia Partnership and Pathways Grant (Grant no. 251309 STA-DY-WI-CO) within the 7th European community Framework Programme. R. Bai wishes to acknowledge the National Natural Science Foundation of China for a research grant (Grant no. 50978084).

References

- [1] F. K. Chang, "Introduction to health monitoring: context, problems, solutions, presentation," in *Proceedings of the 1st European Pre-workshop on Structural Health Monitoring*, Paris, France, 2002.
- [2] Y. J. Yan, L. Cheng, Z. Y. Wu, and L. H. Yam, "Development in vibration-based structural damage detection technique," *Mechanical Systems and Signal Processing*, vol. 21, no. 5, pp. 2198–2211, 2007.
- [3] C. R. Farrar and K. Worden, "An introduction to structural health monitoring," *Philosophical Transactions of the Royal Society A*, vol. 365, no. 1851, pp. 303–315, 2007.
- [4] O. S. Salawu, "Detection of structural damage through changes in frequency: a review," *Engineering Structures*, vol. 19, no. 9, pp. 718–723, 1997.
- [5] X. Jiang, Z. G. John Ma, and W. X. Ren, "Crack detection from the slope of the mode shape using complex continuous wavelet transform," *Computer-Aided Civil and Infrastructure Engineering*, vol. 27, no. 3, pp. 187–201, 2012.
- [6] M. Cao and P. Qiao, "Novel Laplacian scheme and multiresolution modal curvatures for structural damage identification," *Mechanical Systems and Signal Processing*, vol. 23, no. 4, pp. 1223–1242, 2009.
- [7] E. Sazonov and P. Klinkhachorn, "Optimal spatial sampling interval for damage detection by curvature or strain energy mode shapes," *Journal of Sound and Vibration*, vol. 285, no. 4-5, pp. 783–801, 2005.
- [8] M. Cao and P. Qiao, "Integrated wavelet transform and its application to vibration mode shapes for the damage detection of beam-type structures," *Smart Materials and Structures*, vol. 17, no. 5, Article ID 055014, pp. 2337–2453, 2008.
- [9] M. J. Katz, "Fractals and the analysis of waveforms," *Computers in Biology and Medicine*, vol. 18, no. 3, pp. 145–156, 1988.
- [10] L. J. Hadjileontiadis, E. Douka, and A. Trochidis, "Fractal dimension analysis for crack identification in beam structures," *Mechanical Systems and Signal Processing*, vol. 19, no. 3, pp. 659–674, 2005.
- [11] H. Li, Y. Huang, J. Ou, and Y. Bao, "Fractal dimension-based damage detection method for beams with a uniform cross-section," *Computer-Aided Civil and Infrastructure Engineering*, vol. 26, no. 3, pp. 190–206, 2011.
- [12] J. Shi, X. Xu, J. Wang, and G. Li, "Beam damage detection using computer vision technology," *Nondestructive Testing and Evaluation*, vol. 25, no. 3, pp. 189–204, 2010.
- [13] Y. H. An and J. P. Ou, "Experimental and numerical studies on damage localization of simply supported beams based on curvature difference probability method of waveform fractal dimension," *Journal of Intelligent Material Systems and Structures*, vol. 23, no. 4, pp. 415–4426, 2012.
- [14] L. J. Hadjileontiadis and E. Douka, "Crack detection in plates using fractal dimension," *Engineering Structures*, vol. 29, no. 7, pp. 1612–1625, 2007.
- [15] A. Katunin, "Fractal dimension-based crack identification technique of composite beams for on-line SHM systems," *Machine Dynamics Research*, vol. 34, no. 2, pp. 60–69, 2010.
- [16] J. Wang and P. Qiao, "Improved damage detection for beam-type structures using a uniform load surface," *Structural Health Monitoring*, vol. 6, no. 2, pp. 99–110, 2007.
- [17] P. Qiao and M. Cao, "Waveform fractal dimension for mode shape-based damage identification of beam-type structures," *International Journal of Solids and Structures*, vol. 45, no. 22-23, pp. 5946–5961, 2008.
- [18] R. Esteller, G. Vachtsevanos, J. Echauz, and B. Litt, "Comparison of fractal dimension algorithms using synthetic and experimental data," in *Proceedings of the 1999 IEEE International Symposium on Circuits and Systems (ISCAS '99)*, Orlando, Fla, USA, June 1999.
- [19] T. Higuchi, "Approach to an irregular time series on the basis of the fractal theory," *Physica D*, vol. 31, no. 2, pp. 277–283, 1988.
- [20] B. B. Mandelbrot, *The Fractal Geometry of Nature*, vol. 13, W. H. Freeman, San Francisco, Calif, USA, 1982.

- [21] F. Normant and C. Tricot, "Method for evaluating the fractal dimension of curves using convex hulls," *Physical Review A*, vol. 43, no. 12, pp. 6518–6525, 1991.
- [22] P. Paramanathan and R. Uthayakumar, "An algorithm for computing the fractal dimension of waveforms," *Applied Mathematics and Computation*, vol. 195, no. 2, pp. 598–603, 2008.
- [23] G. Stols and H. Bernitz, "Reconstruction of deformed bite marks using affine transformations," *Journal of Forensic Sciences*, vol. 55, no. 3, pp. 784–787, 2010.
- [24] R. W. Sharpe, *Differential Geometry*, vol. 166, Springer, New York, NY, USA, 1997.

Research Article

Application of Kernel Density Estimation in Lamb Wave-Based Damage Detection

Long Yu¹ and Zhongqing Su²

¹ School of Mechanics and Civil & Architecture, Northwestern Polytechnical University, Xi'an, Shaanxi 710129, China

² Department of Mechanical Engineering, The Hong Kong Polytechnic University, Hong Kong

Correspondence should be addressed to Long Yu, yulong@nwpu.edu.cn

Received 13 April 2012; Revised 15 June 2012; Accepted 20 June 2012

Academic Editor: Alessandro Marzani

Copyright © 2012 L. Yu and Z. Su. This is an open access article distributed under the Creative Commons Attribution License, which permits unrestricted use, distribution, and reproduction in any medium, provided the original work is properly cited.

The present work concerns the estimation of the probability density function (p.d.f.) of measured data in the Lamb wave-based damage detection. Although there was a number of research work which focused on the consensus algorithm of combining all the results of individual sensors, the p.d.f. of measured data, which was the fundamental part of the probability-based method, was still given by experience in existing work. Based on the analysis about the noise-induced errors in measured data, it was learned that the type of distribution was related with the level of noise. In the case of weak noise, the p.d.f. of measured data could be considered as the normal distribution. The empirical methods could give satisfied estimating results. However, in the case of strong noise, the p.d.f. was complex and did not belong to any type of common distribution function. Nonparametric methods, therefore, were needed. As the most popular nonparametric method, kernel density estimation was introduced. In order to demonstrate the performance of the kernel density estimation methods, a numerical model was built to generate the signals of Lamb waves. Three levels of white Gaussian noise were intentionally added into the simulated signals. The estimation results showed that the nonparametric methods outperformed the empirical methods in terms of accuracy.

1. Introduction

Structural health monitoring (SHM) is an emerging technology that merges with a variety of techniques related to diagnostics and prognostics. Monitoring the status of structural health can improve the safety and maintainability of critical structures in many fields, such as civil engineering, aerospace, and military industry. An ideal SHM system includes several subsystems in which the damage detection methodology is the key part. Therefore,

numerous damage-detection methods have been researched in years [1]. The method based on Lamb waves has the apparent advantages of high sensitivity to structural damage compared with methods based on the mode shapes [2] or structure dynamic responses [3]. It has been verified that the Lamb wave-based damage detection methods can detect crack, delamination, surface corrosion, penetrate holes, weld defect, and many other kinds of damage in plate and shell structure [4–6]. Consequently, the Lamb wave is widely acknowledged as one of the most encouraging tools for SHM. The relevant research has been conducted intensively since the 1980s [7].

The portion of the SHM process that has received the least attention in the technical literature is the development of statistical models for discrimination between features from the undamaged and damaged structures. The algorithms, which analyze statistical distributions of the measured or derived features to enhance the damage identification process, have been developed [8, 9]. The probability-based diagnostic methods have also been introduced in Lamb wave-based damage detection area in recent years [10, 11]. However, the statistical modes using in the existing Lamb wave-based methods are relatively simple. Despite a number of literatures had been published, which focused on the consensus algorithm of combining all the results of individual sensors, the p.d.f. of the measured data was empirically determined. As a key part of statistical model, it is obvious that the accuracy of the p.d.f. has a significant effect on the precision of damage-detecting result. Compared with the estimating results by empirical formula, the results of statistical methods will be more accurate and reliable. Hence, the study of using statistical methods to estimate the p.d.f. is necessary in Lamb wave-based damage detection.

Elementary parametric estimation method has been adopted under the assumption that the p.d.f. of the measured data is normal distribution [12]. However, the assumption in parametric method limits the application of this method. If the extra assumption is correct, the results produced by parametric method can be more accurate than the results given by empirical formula. While if the assumption is incorrect, parametric methods can be very misleading.

Since the type of p.d.f. of measured data from field experiments is varied and can hardly be predicted, more robust approach methods should be considered. The nonparametric statistic methods can give the parameters of distribution and do not rely on assumptions that the data are drawn from a given probability distribution. Therefore, introducing the nonparametric statistic methods is crucial in Lamb wave-based damage detection.

The aim of this paper is to demonstrate the necessity and feasibility of application of kernel density estimation, which is the most popular nonparametric estimation method in Lamb wave-based damage detection. Two kinds of kernel density estimation methods, the one based on the Gaussian approximation and the one based on the smoothing properties of linear diffusion processes, were briefly introduced in this paper. The signals of Lamb waves with different levels of white Gaussian noise were acquired by using numerical simulation. The framework of applying nonparametric estimation method in Lamb wave-based damage detection was demonstrated by using the simulated signals. The characteristics of noise-induced error in the arriving time of damage-scattered Lamb waves, which is the index used to locate damage, was analyzed. Based on this analysis, the outcomes of two kinds of kernel density estimation method as well as the parametric estimation methods were compared. The results show that the nonparametric methods outperform the parametric method in terms of accuracy and reliability.

2. Lamb Wave-Based Damage Detection

2.1. Background

Lamb waves are a kind of elastic waves propagates in thin plate and shell structure. With a high susceptibility to interference on a propagation path, for example, damage or a boundary, Lamb waves can travel over a long distance even in materials with a high attenuation ratio, and thus a broad area can be quickly examined [13].

Lamb waves are made up of a superposition of longitudinal and shear modes, and its propagation characteristics vary with entry angle, excitation, and structural geometry. A Lamb mode can be either symmetric or antisymmetric, formulated by

$$\frac{\tan(qh)}{\tan(ph)} = -\frac{4k^2qp}{(k^2 - q^2)^2} \quad \text{for symmetric modes,} \quad (2.1)$$

$$\frac{\tan(qh)}{\tan(ph)} = -\frac{(k^2 - q^2)^2}{4k^2qp} \quad \text{for antisymmetric modes,} \quad (2.2)$$

where $p^2 = \omega^2/c_L^2 - k^2$, $q^2 = \omega^2/c_T^2 - k^2$, $k = \omega/c_p$, and h , k , c_L , c_T , c_p , ω are the plate thickness, wavenumber, velocities of longitudinal and transverse modes, phase velocity, and wave circular frequency, respectively. Equations (2.1) and (2.2), correlating the propagation velocity with its frequency, imply that Lamb waves, regardless of its mode, are dispersive (velocity is dependent on frequency).

Lamb waves can be actively excited by a variety of means, such as ultrasonic probe, laser, interdigital transducer, and piezoelectric element. The piezoelectric element can also be used as sensor to collect signals of Lamb waves perfectly. The piezoelectric element is particularly suitable for integration into a host structure as an in situ generator/sensor, for their neglectable mass/volume, easy integration, excellent mechanical strength, wide-frequency responses, low power consumption and acoustic impedance, as well as low cost. Applications of piezoelectric element in Lamb wave-based damage detection are numerous.

Lamb mode selection is an important part for damage detection. The basic symmetric mode, S_0 , and the antisymmetric mode, A_0 , are normally used in practice. Although S_0 is preferred in many of studies [14], utilization of A_0 is increasing because that A_0 is the highly effective for detecting delamination and transverse ply cracks [15]. To implement the Lamb mode selection, a multielement transducer setup was proposed [16] to dominantly generate S_0 or A_0 .

The algorithms for Lamb wave-based damage identification can be roughly divided into two categories. The first category is the algorithms that identify and locate damage by observing the damage-reflected Lamb waves, such as Time-of-Flight (ToF) method [17–19], embedded ultrasonic structural radar [20], and time of difference method [21]. The second category is the algorithms that analyze the changes in the characteristics of Lamb waves caused by the damage in its propagation path, such as tomography method [22] and virtual-sensing paths method [23].

For the algorithms that focus on the damage-reflected waves, the arriving time of the Lamb waves is the key index used to locate damage. Since the signal of Lamb waves is wave packet in the form, several methods have been developed to measure the arriving time of Lamb waves, such as threshold method, correlation method, wavelet method [24],

and a novel cross-correlation analysis method based on a wavelet transform [25, 26]. Among those methods, the threshold method, which was adopted in this paper, has the advantage of simplicity. In threshold method, a threshold value V_t was firstly set up on basis of experience. Once the amplitude of one or several peaks exceed V_t , then the corresponding peaks were recorded. Depending on the magnitude of V_t , one or more peaks could be recorded for a wave packet. If only one peak was recorded, the arriving time was the time corresponding to that peak. If more than one peak were recorded, then the arriving time will be the average of all recorded time. Usually, the threshold value is selected to let several peaks belong to one wave packet can be recorded. The benefit of recording several peaks instead of only the strongest peak is that the averaging process itself can reduce noise to some extent.

2.2. Time of Flight Method

ToF, defined as the time lag from the moment when a sensor catches the damage reflected signal to the moment when the same sensor catches the incident signal, was widely used to locate damage [17–19].

Consider a sensor network consisting of N piezoelectric wafers denoted by s_i ($i = 1, 2, \dots, N$). For convenience of discussion, $s_m - s_n$ hereinafter stands for the sensing path in which s_m serves as the actuator and s_n as the sensor. The center of the damage, if any, is presumed to be (x, y) in coordinate system. Then, the ToF can be defined in (2.1) as T_{i-j} :

$$\frac{L_{A-D}}{V_{S_0}} + \frac{L_{D-S}}{V_{SH_0\text{-damage}}} - \frac{L_{A-S}}{V_{S_0}} = T_{i-j}, \quad (2.3)$$

In which L_{A-D} , L_{D-S} , and L_{A-S} represent the distance from the actuator s_i to the damage, from the damage to the sensor s_j , and from actuator s_i to the sensor s_j , respectively. $V_{SH_0\text{-damage}}$ and V_{S_0} are velocities of the damage-converted SH_0 mode and the incipient S_0 mode, respectively.

Because there are two unknown damage parameters, (x, y) , in (2.3), the solution of (2.3) will be a root locus, which implies the possible locations of the damage for a certain ToF value. In traditional approaches, the damage location is given by seeking the intersections of two or more loci. As shown in Figure 1(a), in the case of using three sensor pairs, there will be three loci, each exhibiting a time delay due to the existence of damage. The point with which all three loci intersect was considered as the location of damage, while the points with which only two loci intersect were considered as pseudodamage location.

There is a prerequisite in the traditional approach. That is all of the measured ToF values T_m were accurate. However, errors are always inevitable in any experimental result due to the reasons such as noises. Therefore, as shown in Figure 1(b), there is no point with which all three loci intersect if the loci were drawn based on noise contained T_m instead of the theoretical value T . It is suggested that the damage location can be given as the area where the density of intersections of two loci is relatively large. That leads to the research about the probability-based approach method, to give the precise damaged area based on the density of intersections.

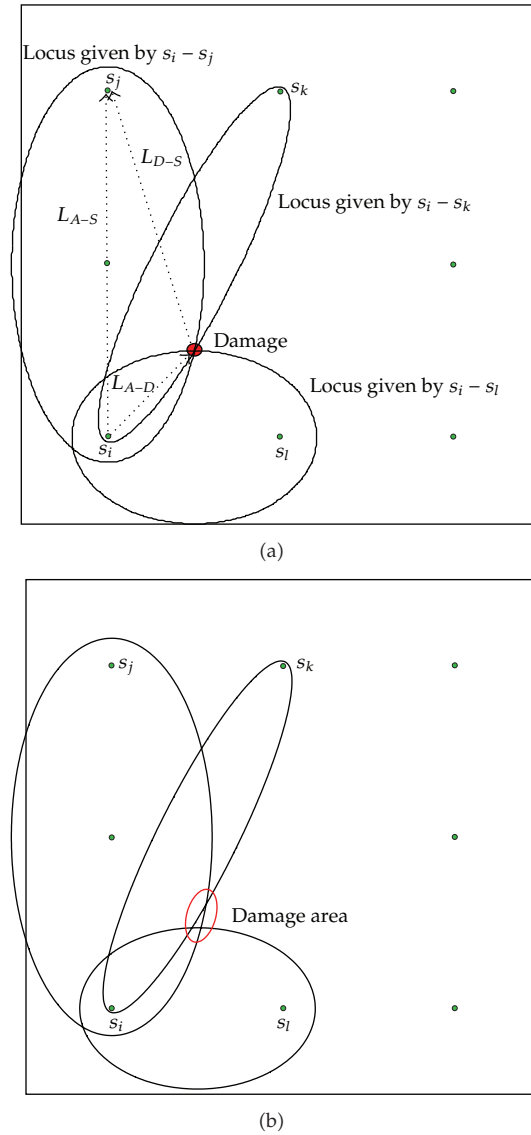


Figure 1: Damage localization using ToF method in a plate. (a) Locus based on accurate ToF value, (b) Locus based on ToF with error.

2.3. Probability-Based ToF Method

The concept of probability-based approach was introduced by Zhao et al. [27] to improve the performance of Lamb wave-based method, and then it was adopted by Su et al. [28] in ToF method. In traditional ToF method, only the points on loci are considered as possible damage location. Other points, regardless of its distance to the loci, will all be excluded outside the possible damage location. In fact, due to the existence of errors in T_m , the real damage may not be on the loci which were drawn based on T_m . Therefore, in probability-based approach method, the points absent in the loci are also considered as possible damage location. The possibility of damage occurrence in those points will be determined by its distance to

the loci. The mesh nodes right located on an above-established locus have the highest degree of probability of damage presence; for the others, the greater the distance to the locus, the lower the probability damage exists there. To quantify the probabilities at all nodes with regard to all loci, a function called as p.d.f. of damage occurrence was introduced. For each loci, a probability distribution map can be given for the detection target plant structure based on p.d.f. of damage occurrence. Combination of all the probability distribution maps can give the final damage detection result.

The main frame of data fusion-based method can be divided into two steps.

- (1) The inspection area of the structure was evenly meshed. For a certain measured ToF, each mesh node will be evaluated about its possibility for the presence of damage by using a probability density function.
- (2) All evaluated results for each measured ToF were combined to give the detection result in a matrix form. Each element of the matrix represents the probability of the presence of damage for one mesh node.

The detection result in matrix form can be illustrated in an image shown in Figure 2, where the lighter the greyscale, the greater the possibility of damage existing at that pixel (each pixel exclusively corresponds to a spatial point of the structure under inspection).

It is obvious that the p.d.f. of damage occurrence is the key part of probability based method. Su et al. [10] suggest the p.d.f. can be quantified in relation to the loci:

$$f(z_{ij}) = \left(\frac{1}{\sigma_{ij}} \sqrt{2\pi} \right) \exp \left[-\frac{z_{ij}^2}{2\sigma_{ij}^2} \right], \quad (2.4)$$

where $f(z_{ij})$ is the Gaussian distribution function, representing the p.d.f. of damage occurrence at node L_i ($i = 1, \dots, K \times K$ for the structure that is comprised of $K \times K$ mesh nodes), perceived by a sensor s_j ($j = 1, \dots, N$ for the sensor network consisting of N sensors). σ_{ij} is the standard deviation and

$$z_{ij} = \|\chi_i - \mu_{ij}\|, \quad (2.5)$$

where χ_i is the location vector of node L_i and μ_{ij} is the location vector of the point on the locus provided by sensor s_j that has the shortest distance to node L_i .

Satisfied results have been obtained by using this kind of p.d.f. But it should be noticed that the standard variance σ_{ij} was selected depending on experience.

The concept of probability-based approach was also adopted in some other Lamb wave-based damage detection methods rather than ToF method. Wang et al. [23] combine the concept of probability-based approach with virtual-sensing paths method. The p.d.f. in their work is an empirical formula and the parameters were given by experience.

There are mainly two disadvantages in the existing work. First, empirical formula usually are simpler to write down and faster to compute, but it depends heavily on the experimental environment. Any change which is inevitable in experiment may cause a big error in the estimated results. That is, the simplicity of empirical formula makes up for its nonrobustness. Since the data measurement work in the Lamb wave-based damage detection is not time consuming, it is reasonable that the density function should be estimated by using robust statistic method. Second, the p.d.f. used in existing work is the distribution

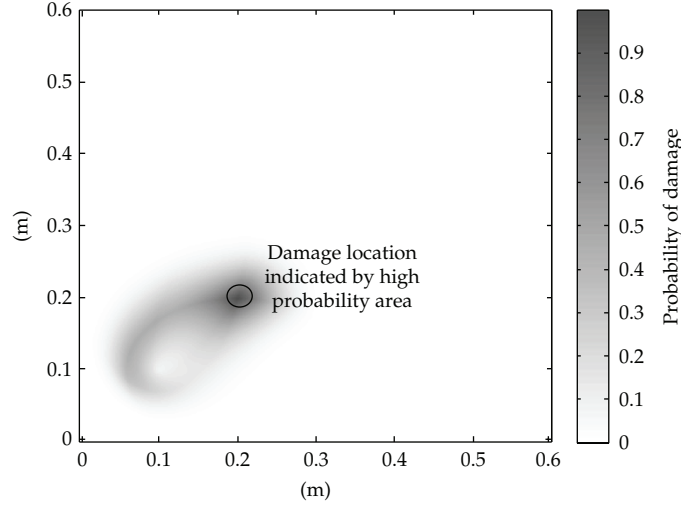


Figure 2: Damage localization result of probability-based method.

function about the location of damage in the plane $f_{D(T)}(s)$, where $s = |D(T) - D(T_m)|$, $D(T)$ and $D(T_m)$ are the damage location corresponding to T (the actual ToF data) and T_m (the experimental ToF data), respectively. It should be noticed that the damage location cannot be directly measured in experiment. Thus, estimating $f_{D(T)}(s)$ directly will be difficult. Based on the estimation of the function $f_{T_m}(t)$ about the distribution of experiment data T_m in time domain, estimating $f_{D(T)}(s)$ by using the mapping relationship defined in (2.3) should be a better method.

Therefore, probability density estimation methods will be introduced in Section 3. The advantages and feasibility of applying probability density estimation methods in ToF method will be demonstrated.

3. Probability Density Estimation

In statistic, density estimation is the method that estimates the parameters of a distribution based on the observed samples. Depending on whether a priori knowledge about the type of the distribution is required, the density estimation methods can be divided into two categories: parametric estimation and nonparametric estimation.

3.1. Parametric Estimation

Parametric estimation mainly includes point estimation and interval estimation. In statistics, point estimation is the use of sample data to calculate a single number of possible values of an unknown population parameter, in contrast to interval estimation, which is an interval. Most commonly used point estimation methods are method of moment estimation, maximum likelihood estimation, and Bayesian estimation. For instance, if it is known that the sample data come from a normal distribution, then the two parameters of normal distribution,

expectation and variance, can be calculated by using (3.1) and (3.2), which is derived by using maximum-likelihood estimation method:

$$\hat{\mu} = \frac{1}{N} \sum_{i=1}^N x_i, \quad (3.1)$$

$$\hat{\sigma}^2 = \frac{1}{N} \sum_{i=1}^N (x_i - \hat{\mu})^2, \quad (3.2)$$

where N is the number of samples.

3.2. Nonparametric Estimation

Nonparametric estimation is a method that estimates the parameters of an unknown distribution while does not rely on assumptions about the type of this distribution. Commonly, nonparametric estimation methods include histogram, nonparametric regression, and kernel density estimation, which is the most popular one.

3.2.1. Kernel Density Estimation Based on the Gaussian Approximation

Kernel density estimation is a nonparametric method to estimate the probability density function of a random variable. Kernel density estimation is a fundamental data smoothing problem where inferences about the population are made, based on a finite-data sample. In some fields such as signal processing and econometrics, kernel density estimation was also termed as the Parzen-Rosenblatt window method, after Emanuel Parzen and Murray Rosenblatt, who are usually credited with independently creating this method in its current form [29, 30].

Let (x_1, x_2, \dots, x_n) be an independent and identically distributed sample drawn from some distribution with an unknown density f . Estimating the shape of this function f is interested. Its kernel density estimator is

$$\hat{f}_h(x) = \frac{1}{n} \sum_{i=1}^n K_h(x - x_i) = \frac{1}{nh} \sum_{i=1}^n K_h\left(\frac{x - x_i}{h}\right), \quad (3.3)$$

where $K(\bullet)$ is the kernel, a symmetric but not necessary positive function that integrates to one; and h is positive and a smoothing parameter called the bandwidth. A kernel with subscript h is called as the scaled kernel and defined as $K_h(x) = (1/h)K(x/h)$. A range of kernel functions are commonly used: uniform, triangular, biweight, triweight, Epanechnikov, normal, and others. As with the kernel regression, the choice of kernel function is not crucial, but the choice of bandwidth is important.

The bandwidth of the kernel is a free parameter which exhibits a strong influence on the resulting estimate [31, 32]. The most common optimality criterion used to select this

parameter is the expected L_2 risk function, also termed as the Mean Integrated Squared Error (MISE);

$$\text{MISE}(h) = \mathbb{E} \int \left(\hat{f}_h(x) - f(x) \right)^2 dx. \quad (3.4)$$

Under weak assumptions on f and K [29, 30], $\text{MISE}(h) = \text{AMISE}(h) + o(1/(nh) + h^4)$, where o is the little o notation of the family of Bachmann-Landau notations. $o(1/(nh) + h^4)$ denotes the function family in which every function grows much slower than $(1/(nh) + h^4)$ [33]. The AMISE is the asymptotic MISE which consists of the two leading terms

$$\text{AMISE}(h) = \frac{R(K)}{nh} + \frac{1}{4} m_2(K)^2 h^4 R(f''), \quad (3.5)$$

where $R(g) = \int g(x)^2 dx$ for a function g , $m_2(K) = \int x^2 K(x) dx$, and f'' is the second derivative of f . The minimum of this AMISE is the solution to this differential equation:

$$\frac{\partial}{\partial h} \text{AMISE}(h) = -\frac{R(K)}{nh^2} + m_2(K)^2 h^3 R(f'') = 0 \quad (3.6)$$

or

$$h_{\text{AMISE}} = \frac{R(K)^{1/5}}{m_2(K)^{2/5} R(f'')^{1/5} n^{1/5}}. \quad (3.7)$$

Neither the AMISE nor the h_{AMISE} can be used directly since they involve the unknown density function f or its second derivative f'' . Therefore, a variety of automatic, data-based methods have been developed for selecting the bandwidth.

If the kernel function is normal and it is assumed that the distribution being estimated is Gaussian, then it can be derived from (3.7) that optimal choice for h is

$$h = \left(\frac{4\hat{\sigma}^5}{3n} \right)^{1/5} \approx 1.06\hat{\sigma}n^{-1/5}, \quad (3.8)$$

where $\hat{\sigma}$ is the standard deviation of the samples. This approximation is termed as the normal distribution approximation, Gaussian approximation, or Silverman's rule of thumb [32].

3.2.2. Kernel Density Estimation via Diffusion

Kernel density estimation is an ongoing research topic in statistics. Botev et al. [34] proposed an adaptive kernel density estimation method based on the smoothing properties of linear diffusion processes. This novel approach method includes two parts: first, a simple and intuitive kernel estimator with substantially reduced asymptotic bias and mean square error, and better boundary bias performance; second, an improved plug-in bandwidth selection method that completely avoids the Gaussian approximation. The new plug-in method is

thus genuinely “nonparametric,” since it does not require a preliminary normal model for the data.

(I) *The Diffusion Estimator*

Given N independent realizations $\chi_N \equiv \{X_1, \dots, X_N\}$ from an unknown continuous p.d.f. f on \mathcal{X} , the Gaussian kernel density estimator is defined as

$$\hat{f}(x; h) = \frac{1}{N} \sum_{i=1}^N \phi(x, X_i; h), \quad (3.9)$$

where

$$\phi(x, X_i; h) = \frac{1}{\sqrt{2\pi h}} e^{-(x-X_i)^2/(2h)} \quad (3.10)$$

is a Gaussian p.d.f. (kernel) with location X_i and scale \sqrt{h} . The scale is the bandwidth in kernel density estimation.

Chaudhuri and Marron [35] had found that there is a link between the Gaussian kernel density estimator and the well-known Fourier heat equation which is a diffusion partial differential equation (PDE). The link is the Gaussian kernel density estimator defined in (3.9) in fact is the unique solution to the Fourier heat equation:

$$\frac{\partial}{\partial t} \hat{f}(x; h) = \frac{1}{2} \frac{\partial^2}{\partial x^2} \hat{f}(x; h), \quad x \in \mathcal{X}, \quad h > 0, \quad (3.11)$$

with $\mathcal{X} \equiv \mathbb{R}$ and initial condition $\hat{f}(x; 0) = \Delta(x)$, where $\Delta(x) = \sum_{i=1}^N \delta(x - X_i)$ is the empirical density of the data χ_N and $\delta(x - X_i)$ is the Dirac measure at X_i . In the heat equation interpretation, the Gaussian kernel in (3.9) is the so-called Green’s function [36] for the diffusion PDE in (3.11). Thus, the Gaussian kernel density estimator $\hat{f}(x; h)$ can be obtained by evolving the solution of (3.11) up to h .

Because any bounded domain can be mapped onto $[0, 1]$ by a linear transformation, there is no loss of generality in assuming that the domain of the data is known as $\mathcal{X} \equiv [0, 1]$. Then, the analytical solution of PDE (3.11) with initial condition $\Delta(x)$ and the Neumann boundary condition in this case is

$$\hat{f}(x; h) = \frac{1}{N} \sum_{i=1}^N \kappa(x, X_i; h), \quad x \in [0, 1], \quad (3.12)$$

where the kernel k is given by

$$\kappa(x, X_i; h) = \sum_{k=-\infty}^{\infty} \phi(x, 2k + X_i; h) + \phi(x, 2k - X_i; h). \quad (3.13)$$

The Neumann boundary condition is

$$\left. \frac{\partial}{\partial x} \hat{f}(x; h) \right|_{x=1} = \left. \frac{\partial}{\partial x} \hat{f}(x; h) \right|_{x=0} = 0, \quad (3.14)$$

and the target of this boundary condition is to ensure that (3.12) satisfies the requirements of p.d.f., such as \hat{f} should be a nonnegative Lebesgue-integrable function and integrates to unity.

It has been proved that the estimator given in (3.12) arises as the solution of the diffusion PDE is better in boundary bias properties compared with the traditional estimator given in (3.9).

Therefore, motivated by the idea of acquiring the estimator from the solution of diffusion PDE, Botev proposed that the most general linear time-homogeneous diffusion PDE can be a starting point for the construction of a better kernel density estimator. The simple diffusion model described in (3.11) can be extended on the basis of the smoothing properties of the linear diffusion PDE:

$$\frac{\partial}{\partial h} g(x; h) = Lg(x; H), \quad x \in \mathcal{X}, \quad t > 0, \quad (3.15)$$

where the linear differential operator L is of the form $(1/2)(d/dx)(a(x)(d/dx)(\cdot/p(x)))$, and a and p can be any arbitrary positive function on \mathcal{X} with bounded second derivatives, and the initial condition is $g(x; 0) = \Delta(x)$.

The solution of (3.15) can be the diffusion kernel estimator and written as

$$g(x; h) = \frac{1}{N} \sum_{i=1}^N \kappa(x, X_i; h). \quad (3.16)$$

There is no analytical expression for the diffusion kernel satisfying (3.16), κ can be written in terms of a generalized Fourier series in the case that \mathcal{X} is bounded:

$$\kappa(x, X_i; h) = p(x) \sum_{k=0}^{\infty} e^{\lambda_k h} \varphi_k(x) \varphi_k(y), \quad (3.17)$$

where $\{\varphi_k\}$ and $\{\lambda_k\}$ are the eigenfunctions and eigenvalues of the Sturm-Liouville problem on $[0, 1]$:

$$\begin{aligned} L^* \varphi_k &= \lambda_k \varphi_k, \quad k = 0, 1, 2, \dots, \\ \varphi'_k(0) &= \varphi'_k(1) = 0, \quad k = 0, 1, 2, \dots, \end{aligned} \quad (3.18)$$

where L^* is of the form $(1/2p(y))(\partial/\partial y)(a(y)(\partial/\partial y)(\cdot))$; that is, L^* is the adjoint operator of L .

(II) Improved Plug-In Bandwidth Selection Method

The novel plug-in bandwidth selection method for the diffusion estimator defined in (3.16) proposed by Botev is based on the improved plug-in bandwidth selection method for the Gaussian kernel density estimator defined in (3.9).

Assuming that f'' is a continuous square-integrable function, the asymptotically optimal value of h for Gaussian kernel density estimator is the minimize of the first-order asymptotic approximation of MISE [37]

$$*_h = \left(\frac{1}{2N\sqrt{\pi}\|f''\|^2} \right)^{2/5}. \quad (3.19)$$

It is clear from (3.19) that to compute the optimal $*_h$, one needs to estimate the functional $\|f''\|^2$. Consider the problem of estimating $\|f^{(j)}\|^2$ for any arbitrary integer $j \geq 1$. The identity $\|f^{(j)}\|^2 = (-1)^j \mathbb{E}_f(f^{(2j)}(X))$ suggests two plug-in estimators:

$$\text{the first one is } (-1)^j \mathbb{E}_f(f^{(2j)}(X)) = \frac{(-1)^j}{N^2} \sum_{k=1}^N \sum_{m=1}^N \phi^{(2j)}(X_k, X_m; h_j), \quad (3.20)$$

$$\text{the second one is } \|\widehat{f^{(j)}}\|^2 := \|\widehat{f^{(j)}}(\cdot, h)\|^2 = \frac{(-1)^j}{N^2} \sum_{k=1}^N \sum_{m=1}^N \phi^{(2j)}(X_k, X_m; 2h_j).$$

For a given bandwidth, both estimators $(-1)^j \mathbb{E}_f(f^{(2j)}(X))$ and $\|\widehat{f^{(j)}}\|^2$ aim to estimate the same quantity $\|f^{(j)}\|^2$. Therefore, $*_h_j$ can be selected to make both estimators asymptotically equivalent in the mean square error sense:

$$*_h_j = \left(\frac{1 + 1/2^{j+1/2}}{3} \frac{1 \times 3 \times 5 \times \cdots \times (2j-1)}{N\sqrt{\pi/2}\|f^{(j+1)}\|^2} \right)^{2/(3+2j)}. \quad (3.21)$$

Computation of $*_h_j$ by using (3.21) involves $\|f^{(j+1)}\|^2$ which is unknown. Thus, each $*_h_j$ is estimated by

$$*_h_j = \left(\frac{1 + 1/2^{j+1/2}}{3} \frac{1 \times 3 \times 5 \times \cdots \times (2j-1)}{N\sqrt{\pi/2}\|\widehat{f^{(j+1)}}\|^2} \right)^{2/(3+2j)}. \quad (3.22)$$

Computation of $\|\widehat{f^{(j+1)}}\|^2$ requires the estimation of $*_h_{j+1}$, which in turn requires the estimation of $*_h_{j+2}$, and so on, as seen from (3.20) and (3.22). There is the problem of estimating the infinite sequence $\{*_h_{j+k}, k \geq 1\}$. However, for some $l > 0$, if $*_h_{l+1}$ can be given, then all $\{*_h_j, 1 \leq j \leq l\}$ can be estimated recursively. Based on this idea, the l -stage direct plug-in bandwidth selector [37] has been proposed.

Denote the functional dependence of ${}^*\hat{h}_j$ and ${}^*\hat{h}_{l+1}$ as

$${}^*\hat{h}_j = \gamma_j({}^*\hat{h}_{j+1}). \quad (3.23)$$

It is then obvious that ${}^*\hat{h}_j = \gamma_j(\gamma_{j+1}({}^*\hat{h}_{j+2})) = \gamma_j(\gamma_{j+1}(\gamma_{j+2}({}^*\hat{h}_{j+3}))) = \dots$. For simplicity of notation, the composition can be defined as

$$\gamma^{[k]}(h) = \gamma_1(\dots \gamma_{k-1}(\gamma_k(h))), \quad k \geq 1. \quad (3.24)$$

The estimate of *h satisfies

$${}^*\hat{h} = \xi {}^*\hat{h}_1 \gamma = \xi \gamma^{[1]}({}^*\hat{h}_2) = \xi \gamma^{[2]}({}^*\hat{h}_3) = \dots = \xi \gamma^{[l]}({}^*\hat{h}_{l+1}). \quad (3.25)$$

Then, for a given integer $l > 0$, the l -stage direct plug-in bandwidth selector consists of computing

$${}^*\hat{h} = \xi \gamma^{[l]}({}^*h_{l+1}), \quad (3.26)$$

where ${}^*h_{l+1}$ is estimated by assuming that f in $\|f^{(l+2)}\|^2$ is a normal density with mean and variance estimated from the data.

It is noticed that the assumption in the l -stage direct plug-in bandwidth selector method can lead to arbitrarily bad estimates of *h , when, for example, the true f is far from being Gaussian. Therefore, Botev proposed to find a solution to the nonlinear equation:

$$h = \xi \gamma^{[l]}(h), \quad (3.27)$$

for some l , using either fixed point iteration or Newton's method with initial guess $h = 0$. The fixed-point iteration version is formalized in the following Improved Sheather-Jones algorithm:

- (1) Given $l > 2$, initialize with $z_0 = \varepsilon$, where ε is machine precision, and $n = 0$;
- (2) Set $z_{n+1} = \xi \gamma^{[l]}(z_n)$;
- (3) if $|z_{n+1} - z_n| < \varepsilon$, stop and set ${}^*\hat{h} = z_{n+1}$; otherwise, set $n := n + 1$ and repeat from step (2);
- (4) Deliver the Gaussian kernel density estimator in (3.9) evaluated at ${}^*\hat{h}$ as the final estimator of f , and ${}^*\hat{h}_2 = \gamma^{[l-1]}(z_{n+1})$ as the bandwidth for the optimal estimation of $\|f''\|^2$.

It has been proved that the recommending setting for l is 5.

The above section explains how to estimate the bandwidth $\sqrt{*h}$ of the Gaussian kernel density estimator. Now, the algorithm that estimates the bandwidth $\sqrt{h^*}$ of the diffusion estimator will be introduced.

Assuming that f is as many times continuously differentiable as needed, then it has been proved that the square of the asymptotically optimal bandwidth is

$$h^* = \left(\frac{\mathbb{E}_f[\sigma^{-1}(x)]}{2N\sqrt{\pi}\|Lf\|^2} \right)^{2/5}. \quad (3.28)$$

Computation of h^* in (3.28) requires an estimate of $\|Lf\|^2$ and $\mathbb{E}_f[\sigma^{-1}(x)]$. The latter one can be estimated via the unbiased estimator $(1/N) \sum_{i=1}^N \sigma^{-1}(X_i)$. The identity $\|Lf\|^2 = \mathbb{E}_f L^* L f(x)$ suggests two possible estimators. The first one is

$$\mathbb{E}_f \widehat{L^* L f}(x) := \frac{1}{N} \sum_{i=1}^N \sum_{j=1}^N L^* L_\kappa(x, X_i; h_2)|_{x=X_j}. \quad (3.29)$$

The second one is

$$\|\widehat{Lf}\|^2 := \frac{1}{N} \sum_{i=1}^N \sum_{j=1}^N L^* L_\kappa(x, X_i; 2h_2)|_{x=X_j}. \quad (3.30)$$

Just like the way that $*h_2$ is derived for the Gaussian kernel density estimator, h_2^* is selected to make both estimators $\mathbb{E}_f \widehat{L^* L f}(x)$ and $\|\widehat{Lf}\|^2$ have the same asymptotic mean square error:

$$h_2^* = \left(\frac{8 + \sqrt{2}}{24} \frac{-3\sqrt{2}\mathbb{E}_f[\sigma^{-1}(X)]}{8\sqrt{\pi}N\mathbb{E}_f[L^* L^2 f(X)]} \right)^{2/7}. \quad (3.31)$$

Note that h_2^* has the same rate of convergence to 0 as $*h_2$. In fact, since the Gaussian kernel density estimator is a special case of the diffusion estimator when $p(x) = a(x) = 1$, the plug-in estimator equation (3.30) for the estimation of $\|Lf\|^2$ reduces to the plug-in estimator for the estimation of $(1/4)\|f''\|^2$. In addition, the h_2^* in (3.31) and $*h_2$ are identical when $p(x) = a(x) = 1$. Thus, the bandwidth for the diffusion estimator given in (3.16) can be selected by using the following algorithm:

- (1) Given the data X_1, \dots, X_N , run the Improved Sheather-Jones algorithm to obtain the Gaussian kernel density estimator defined in (3.9) evaluated at $*\hat{h}$ and the optimal bandwidth $\sqrt{*h_2}$ for the estimation of $\|f''\|^2$. This is the pilot estimation step.
- (2) Let $p(x)$ be the Gaussian kernel estimator from above step, and let $a(x) = p^\alpha(x)$ for some $\alpha \in [0, 1]$.
- (3) Estimate $\|Lf\|^2$ via the plug-in estimator given in (3.30) using $\hat{h}_2^* = *\hat{h}_2$

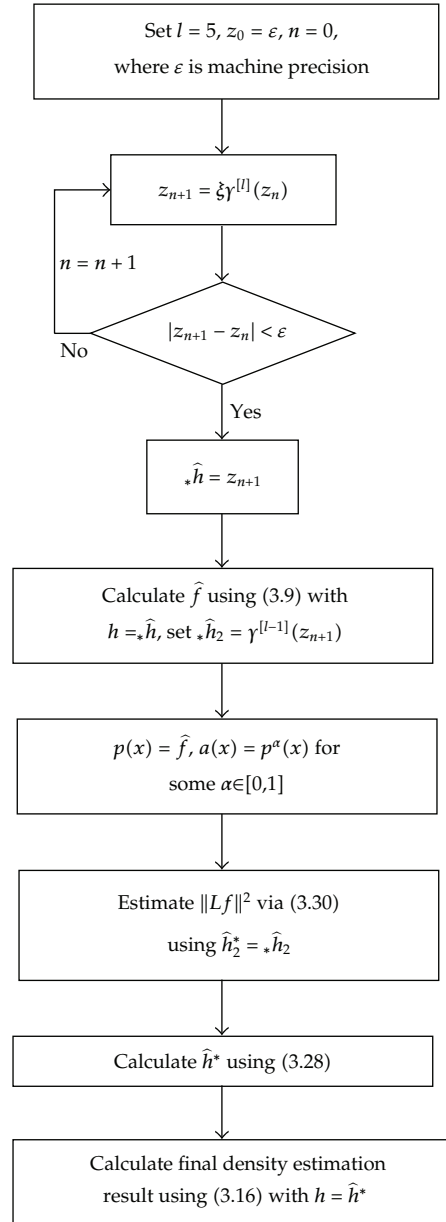


Figure 3: Flow chart of kernel density estimation via diffusion.

- (4) Substitute the estimate of $\|Lf\|^2$ into (3.28) to obtain an estimate for h^* .
- (5) Deliver the diffusion estimator in (3.16) evaluated at \hat{h}^* as the final density estimate.

The flow chart of the entire bandwidth selection algorithm was shown in Figure 3.

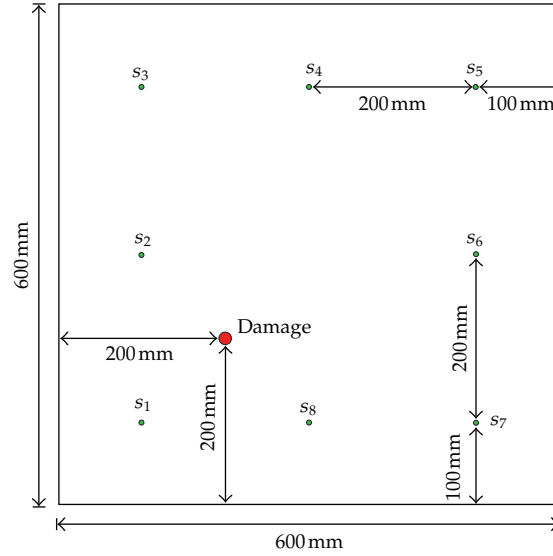


Figure 4: Schematic of numerical simulation mode.

4. Numerical Simulation

Feasibility of using the kernel density estimation method to estimate the p.d.f. of experiment results was demonstrated in a thin plate structure via finite-element (FE) simulation. Eight PZT wafers were surface installed at an aluminium plate. The aluminium plate was 600 mm \times 600 mm \times 1.5 mm in size, supported with all its four edges. The elastic modulus, poisson's ration, and density of the aluminium are 71e9GPa, 0.35, and 2711 Kg/m³, respectively. The thin plate was three dimensionally modeled using eight-node brick solid elements. To ensure simulation precision, the largest dimension of FE elements was less than 1 mm and the plate was divided into multilayer in thickness, guaranteeing that at least ten elements were allocated per wavelength of the incident diagnostic wave, which has been demonstrated sufficiently to portray the characteristics of elastic waves in the thin plate [19]. A through-thickness hole of 16 mm in diameter was assumed in the plate, 200 mm and 200 mm away from the left and low edges of the plate, respectively (Figure 4). The S_0 mode of Lamb waves was used to detect damage. Five-cycle Hanning window-modulated sinusoid tone bursts at a central frequency of 300 kHz were activated as the incident diagnostic wave signal. The speed of S_0 mode is 5159.5 m/s in this simulation.

Gaussian noise is statistical noise that has its probability density function equal to that of the normal distribution, which is also known as the Gaussian distribution. A special case is white Gaussian noise, in which the values at any pairs of times are statistically independent (and uncorrelated). It is well known that noise comes from many natural sources is Gaussian noise. Therefore, in order to simulate the environment noise, three signal-to-noise ration (SNR) levels (20 dB, 30 dB, and 40 dB) of white Gaussian noise were intentionally added into the numerical simulated Lamb waves signals.

In numerical model, four sensor pairs are used to locate the damage. The sensor pairs are s2-6 formed by sensor 2 and sensor 6; s4-8 by sensor 4 and 8; s3-7 by sensor 3 and 7; s3-5 by sensor 3 and 5. The process of adding three levels white Gaussian noise in the signals

captured by the four sensor pairs repeated 30 times. That is, there are 30 ToF results for each sensor pair under each level of noise.

5. Results and Discussion

5.1. The Characteristics of Noise-Induced Error in ToF

It can be expected in theory that the nonparametric estimation methods should have a better performance than parametric estimation method when deal with the distribution without a priori knowledge about its type. The advantage of kernel density estimation method will be demonstrated in this paper by estimating $f_{T_m}(t)$ of s4-8. In statistic, the performance of density estimation methods is usually verified through comparing the estimation results with the bona fide p.d.f of some well-known datasets. That is, in order to show the accuracy of estimation results, one needs to know the *real* p.d.f. of the distribution to be estimated. It is difficult to give the analytical expression of $f_{T_m}(t)$ about ToF measured by threshold method. However, partial understanding about the characteristics of noise-induced error in ToF still can be obtained by analyzing the process of threshold method. That will be helpful to prove the advantage of nonparametric estimation methods in ToF method.

ToF is given by comparing the arriving time of incident waves and damage-scattered waves. Since the incident waves is strong, the errors in arriving time of incident waves can be neglected. Without loss of generality, the errors in ToF was considered to be caused entirely by the errors in the arriving time of damage-scattered waves.

As mentioned in Section 2.1, the existence of wave packet is determined by whether the amplitude of signal is bigger than the threshold value. Once a wave packet is detected, the arriving time of entire wave packet is given by the time of recorded peaks. The process of threshold method suggests there are two kinds of noise-induced errors in ToF:

$$T_m = T + \varepsilon_1 + \varepsilon_2, \quad (5.1)$$

where ε_1 denotes the variance in the arriving time of single peak, ε_2 denotes the error caused by misidentification of peaks. While ε_1 is easy to understand, ε_2 is relatively complex. The signal received by s4-8 which shown in Figure 5 is taken as example to explain the existence of ε_2 . Noise not only can change the time of peaks, but also can change the relative magnitude relationship of peaks. That means the sequence of peaks on its magnitude may be changed by noise. If there were no noise and the arriving time was measured by recording the strongest peak, then the second peak of the damage-scattered waves shown in Figure 5 should be recorded. However, the strongest peak may change to other peaks, such as the third or the fourth peak, in noise-contaminated signals. The same problem exists in the method of recording several peaks. For example, if there is no noise and the arriving time is measured as the average of four peaks. Then, the first four peaks (the second, the third, the fourth, and the fifth in this case) should be recorded. However, the first peak in noise-contaminated signals is likely to become stronger than the fifth peak. That leads to the error ε_2 in ToF.

It is obvious that ε_2 is larger than ε_1 , but it appears only in strong noise environment.

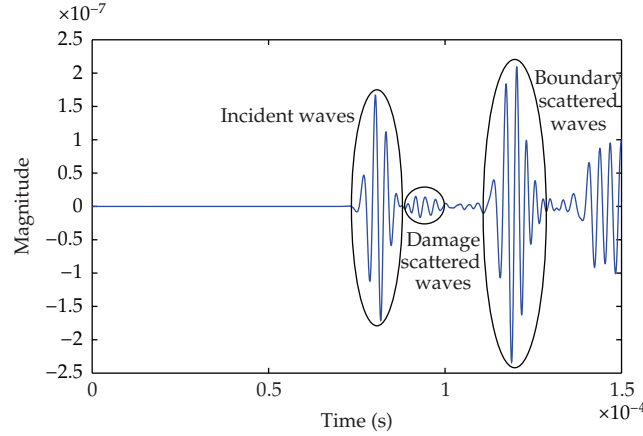


Figure 5: The signals of Lamb waves received by sensor 8.

5.2. Density Estimation Results

Parametric estimation method, the kernel density estimation based on the Gaussian approximation, and the adaptive kernel density estimation via diffusion were used to estimate $f_{T_m}(t)$. The sample data is ToF measured by s4-8 with three levels noise.

The estimation results for the signal with 40 dB SNR noise was shown in Figure 6. The symbol “+” in Figure 6 and the following Figures 7, 8, and 9 were used to give an intuitive understanding about the distribution of samples. Each “+” represented a sample. It could be seen that samples were distributed around the two values. Most of the samples (26 samples of total 30 samples) were distributed in the range from $1.1e-5$ second to $1.15e-5$ second. 4 samples were distributed in the range from $0.82e-5$ second to $0.87e-5$ second. The p.d.f. given by the kernel density estimation based on the Gaussian approximation and the adaptive kernel density estimation via diffusion was the functions with two peaks. The p.d.f. given by parametric estimation method was undeniably a normal density function. Based on the conclusion drawn in the above section about the characteristics of noise-induced errors in ToF, the distribution of samples could be easily understood. Because the noise was weak in this case, most of the samples, which were only affected by ε_1 , were distributed around the analytic value of ToF ($1.117e-5$ second). The other 4 samples which were relatively far from the analytic value were affected by both ε_1 and ε_2 . Therefore, it could be learnt that two kinds of kernel density estimation make correct estimating about the p.d.f. of T_m . Because the assumption about the type of distribution to be estimated was incorrect, parametric estimation method was very misleading in this case.

The fact that only 4 samples were affected by both ε_1 and ε_2 in this case could be utilized to learn the characteristic of ε_1 . Since these samples could be easily distinguished from the samples which were only affected by ε_1 , these samples could be excluded from the data set. Then, the density function was estimated with the refined dataset. The results were shown in Figure 7. It could be seen that the results of two kinds kernel density estimation methods were similar to normal distribution.

Lilliefors test was adopted to check whether the refined samples came from a normal distribution. In statistics, the Lilliefors test, named after Hubert Lilliefors, was an adaptation of the Kolmogorov-Smirnov test [38]. It was used to test the null hypothesis that data

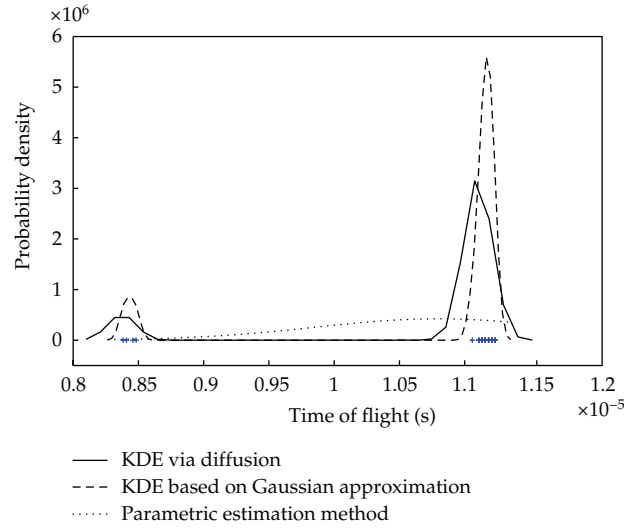


Figure 6: p.d.f. estimated results for samples from s4-8 with 40 dB noise.

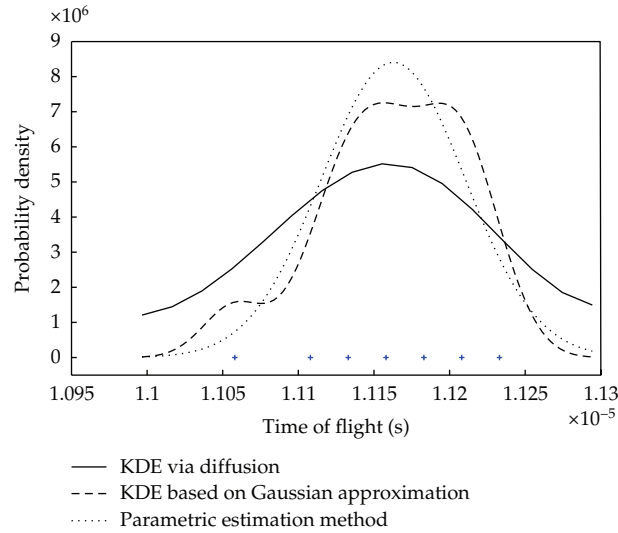


Figure 7: p.d.f. estimated results for refined samples from s4-8 with 40 dB noise.

came from a normally distributed population, when the null hypothesis did not specify which normal distribution; that is, it did not specify the expected value and variance of the distribution.

The calculated value from the Lilliefors test was 0.1373, which was less than the critical value 0.1699 corresponding to 5% significance level. The null hypothesis that the refined data came from a normally distributed population was accepted. It explained why the empirical formula given in the previous work was a normal distribution type and why the damage detection results based on the empirical formula was satisfied. Since the noise in previous

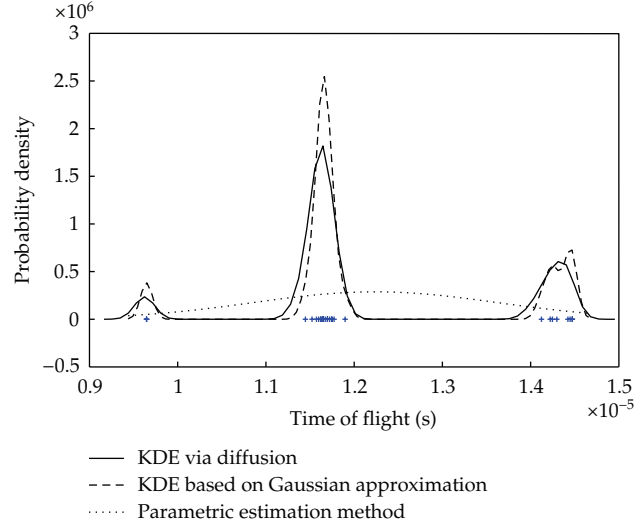


Figure 8: p.d.f. estimated results for samples from s4-8 with 30 dB noise.

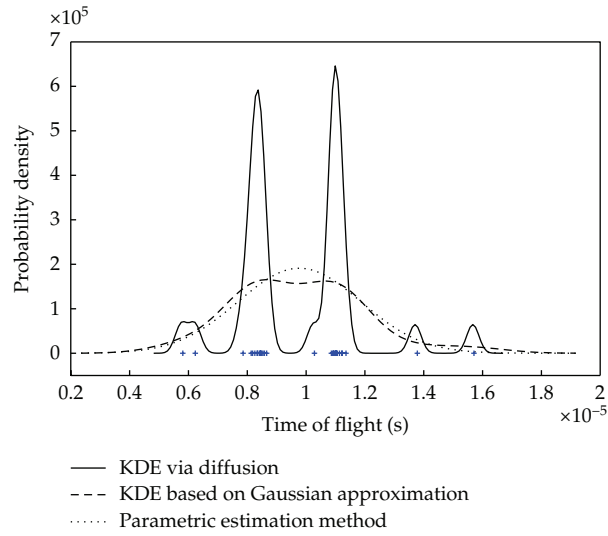


Figure 9: p.d.f. estimated results for samples from s4-8 with 20 dB noise.

work [12] was weak and the T_m data was only affected by ε_1 , its distribution was actually normal distribution.

The estimation results for the signals with 30 dB SNR noise were shown in Figure 8. It could be seen that as in the case of 20 dB SNR noise, parametric estimation method failed to give correct estimation.

The estimation results for the signals with 20 dB SNR noise were shown in Figure 9. It could be seen that, with the increase of noise level, the kernel density estimation based on the Gaussian approximation, which was traditional kernel density estimation, failed to give correct estimation. Only the novel and completely data-driven method, the kernel density estimation via diffusion-, could give correct estimation.

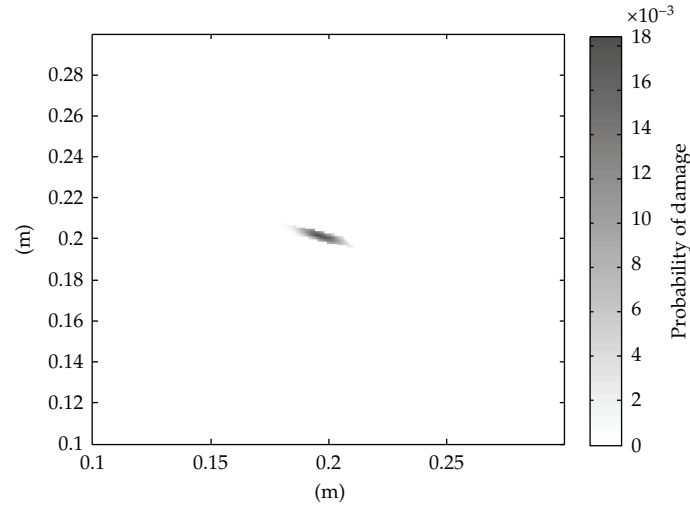


Figure 10: Damage localization result based on parametric estimate method (partial view).

5.3. Damage Detection Results

The damage localization under 20 dB noise environment was selected as the example to show that an accurate estimation was important for the localization result. The p.d.f. estimation results given by three kinds of density estimation methods introduced in Section 2 were used to calculate the location of damage. The results were shown in Figures 10, 11, and 12. It could be seen that the locating process which employed the kernel density estimation via diffusion has the most accurate localization result. This indicated that the an accurate estimation could ensure an better localization result.

6. Conclusion

The characteristics of noise-induced error in ToF data measured by using threshold method were analyzed.

The empirical formula method and the parametric estimation method presented in existing work had the same assumption that the experimental data came from a normal distribution. This assumption had been verified by real experiments and numerical simulation. The results in this paper revealed that the type of distribution of ToF data was related to the noise level. The empirical formula method and the parametric estimation method were developed in laboratory environment where the noise was weak. It had also been proved in this paper that the ToF data measured from high SNR signal ($\text{SNR} > 40 \text{ dB}$) were distributed normally. Therefore, the density estimation method with the normality assumption presented in existing work can work well in laboratory environment.

However, the signals of field experiment usually contained much more strong noise. The results in this paper showed that even for the signal with 40 dB SNR, the distribution of measured ToF data were not normal distribution. In this case, nonparametric estimation method must be employed to estimate the p.d.f. correctly. Further, investigating about the signals with 30 dB and 20 dB noise showed that, with the increasing noise, only the kernel

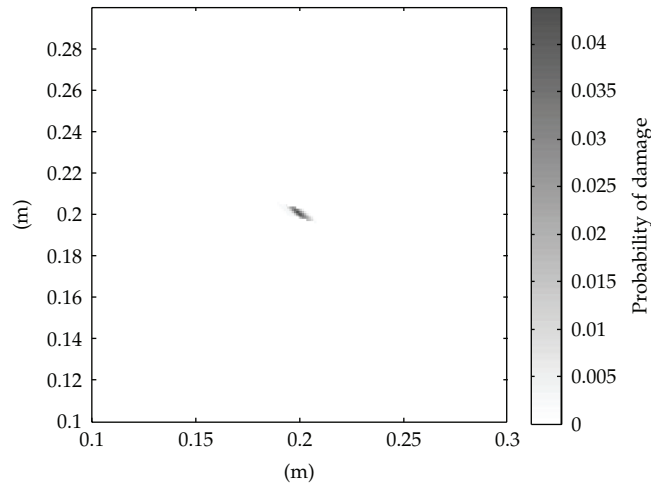


Figure 11: Damage localization result based on kernel density estimation with Gaussian approximation (partial view).

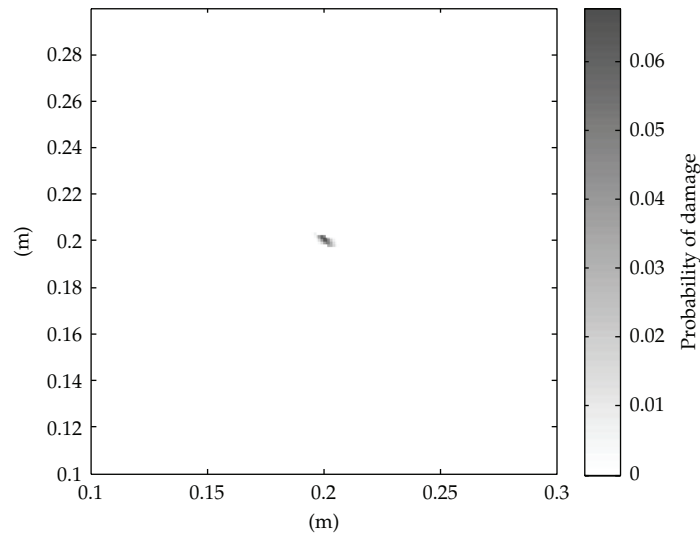


Figure 12: Damage localization result based on kernel density estimation via diffusion (partial view).

density estimation via diffusion, which is purely data driven, can give a satisfied estimating result.

The damage localization under 20dB noise environment had been carried out. Parametric estimation method with the normality assumption, the kernel density estimation based on the Gaussian approximation and the kernel density estimation via diffusion were adopted to estimate the p.d.f. of measured data. Three different p.d.f. were obtained by employing the above-motioned three kinds of density estimation methods. By using each p.d.f, a damage location result can be calculated. Through comparing the three results of damage location, it can be seen that an accurate estimation of p.d.f. has a direct effect on

the accuracy of the results. Applying kernel density estimation in Lamb wave-based damage detection was necessary.

The noise studied in this paper was the white Gaussian noise. The noise in the real field experiment was much more complex. Further study was needed to reveal the characteristic of errors in ToF data caused by noise in field experiment. However, the complex nature of noise in field experiment could not be a trouble for the application of kernel density estimation method, instead, it could be a reason to apply this method. It had been proved that when deal with simple noise, the kernel density estimation method introduced in this paper performed better, in comparison with empirical methods. Since the kernel density estimation method did not rely on any assumption about the distribution to be estimated, it could be expected that the kernel density estimation method could demonstrate a greater advantage in a complex noise environment.

Acknowledgments

This work was financially supported by National Natural Science Foundation of China under grant no. 50905141, the Program for New Century Excellent Talents in University of China, and the NPU Foundation for Fundamental Research under grant no. NPU-FFR-JC20110258.

References

- [1] Y. J. Yan, L. Cheng, Z. Y. Wu, and L. H. Yam, "Development in vibration-based structural damage detection technique," *Mechanical Systems and Signal Processing*, vol. 21, no. 5, pp. 2198–2211, 2007.
- [2] Q. Yang, "A new damage identification method based on structural flexibility disassembly," *Journal of Vibration and Control*, vol. 17, no. 7, pp. 1000–1008, 2011.
- [3] L. Yu, L. Cheng, L. H. Yam, Y. J. Yan, and J. S. Jiang, "Online damage detection for laminated composite shells partially filled with fluid," *Composite Structures*, vol. 80, no. 3, pp. 334–342, 2007.
- [4] X. Lu, M. Lu, L. M. Zhou et al., "Evaluation of welding damage in welded tubular steel structures using guided waves and a probability-based imaging approach," *Smart Materials and Structures*, vol. 20, no. 1, Article ID 015018, 2011.
- [5] J. Chen, Z. Su, and L. Cheng, "Identification of corrosion damage in submerged structures using fundamental anti-symmetric Lamb waves," *Smart Materials and Structures*, vol. 19, no. 1, Article ID 015004, 2010.
- [6] G. Zumpano and M. Meo, "A new nonlinear elastic time reversal acoustic method for the identification and localisation of stress corrosion cracking in welded plate-like structures—a simulation study," *International Journal of Solids and Structures*, vol. 44, no. 11–12, pp. 3666–3684, 2007.
- [7] Z. Su, L. Ye, and Y. Lu, "Guided Lamb waves for identification of damage in composite structures: a review," *Journal of Sound and Vibration*, vol. 295, no. 3–5, pp. 753–780, 2006.
- [8] C. R. Farrar, S. W. Doebling, and D. A. Nix, "Vibration-based structural damage identification," *Philosophical Transactions of the Royal Society A*, vol. 359, no. 1778, pp. 131–149, 2001.
- [9] H. Sohn, C. R. Farrar, F. M. Hemez, and J. J. Czarnecki, "A review of structural health monitoring literature: 1996–2001," in *Proceedings of the 3rd World Conference on Structural Control*, Como, Italy, April 2002.
- [10] Z. Su, L. Cheng, X. Wang, L. Yu, and C. Zhou, "Predicting delamination of composite laminates using an imaging approach," *Smart Materials and Structures*, vol. 18, no. 7, Article ID 074002, 2009.
- [11] E. D. Niri and S. Salamone, "A probabilistic framework for acoustic emission source localization in plate-like structures," *Smart Materials and Structures*, vol. 21, no. 3, Article ID 035009, 2012.
- [12] L. Yu, Z. Su, and X. Liu, "The definition and measurement of the probability density function in lamb wave damage detection based on data fusion," in *Proceedings of the 14th Asia Pacific Vibration Conference*, Kowloon, Hong Kong, 2011.
- [13] A. Raghavan and C. E. S. Cesnik, "Review of guided-wave structural health monitoring," *Shock and Vibration Digest*, vol. 39, no. 2, pp. 91–114, 2007.

- [14] S. G. Pierce, B. Culshaw, G. Manson, K. Worden, and W. J. Staszewski, "Application of ultrasonic Lamb wave techniques to the evaluation of advanced composite structures," in *Smart Structures and Materials 2000—Sensory Phenomena and Measurement Instrumentation for Smart Structures and Materials*, vol. 3986 of *Proceedings of SPIE*, pp. 93–103, March 2000.
- [15] D. N. Alleyne and P. Cawley, "The interaction of Lamb waves with defects," *IEEE Transactions on Ultrasonics, Ferroelectrics, and Frequency Control*, vol. 39, no. 3, pp. 381–397, 1992.
- [16] S. Grondel, C. Paget, C. Delebarre, J. Assaad, and K. Levin, "Design of optimal configuration for generating A0 Lamb mode in a composite plate using piezoceramic transducers," *Journal of the Acoustical Society of America*, vol. 112, no. 1, pp. 84–90, 2002.
- [17] Z. Su, L. Ye, and X. Bu, "A damage identification technique for CF/EP composite laminates using distributed piezoelectric transducers," *Composite Structures*, vol. 57, no. 1–4, pp. 465–471, 2002.
- [18] M. Lemistre and D. L. Balageas, "Structural health monitoring system based on diffracted Lamb wave analysis by multiresolution processing," *Smart Materials and Structures*, vol. 10, no. 3, pp. 504–511, 2001.
- [19] Y. Lu, L. Ye, Z. Su, and C. Yang, "Quantitative assessment of through-thickness crack size based on Lamb wave scattering in aluminium plates," *NDT and E International*, vol. 41, no. 1, pp. 59–68, 2008.
- [20] V. Giurgiutiu, J. Bao, and W. Zhao, "Piezoelectric wafer active sensor embedded ultrasonics in beams and plates," *Experimental Mechanics*, vol. 43, no. 4, pp. 428–449, 2003.
- [21] L. Yu, L. Cheng, and Z. Su, "Correlative sensor array and its applications to identification of damage in plate-like structures," *Structural Control and Health Monitoring*. In press.
- [22] D. A. Hutchins, D. P. Jansen, and C. Edwards, "Lamb-wave tomography using non-contact transduction," *Ultrasonics*, vol. 31, no. 2, pp. 97–103, 1993.
- [23] D. Wang, L. Ye, Z. Su, Y. Lu, F. Li, and G. Meng, "Probabilistic damage identification based on correlation analysis using guided wave signals in aluminum plates," *Structural Health Monitoring*, vol. 9, no. 2, pp. 133–144, 2010.
- [24] G. Peng and S. Yuan, "Damage localization on two-dimensional structure based on wavelet transform and active lamb wave-based method," *Materials Science Forum*, vol. 475–479, no. 3, pp. 2119–2122, 2005.
- [25] L. De Marchi, A. Marzani, N. Speciale, and E. Viola, "A passive monitoring technique based on dispersion compensation to locate impacts in plate-like structures," *Smart Materials and Structures*, vol. 20, no. 3, Article ID 035021, 2011.
- [26] A. Perelli, L. De Marchi, A. Marzani, and N. Speciale, "Acoustic emissions localization in plates with dispersion and reverberations by using sparse PZT sensors in passive mode," *Smart Materials and Structures*, vol. 21, no. 2, Article ID 025010, 2012.
- [27] X. Zhao, H. Gao, G. Zhang et al., "Active health monitoring of an aircraft wing with embedded piezoelectric sensor/actuator network: I. Defect detection, localization and growth monitoring," *Smart Materials and Structures*, vol. 16, no. 4, pp. 1208–1217, 2007.
- [28] Z. Su, X. Wang, L. Cheng, L. Yu, and Z. Chen, "On selection of data fusion schemes for structural damage evaluation," *Structural Health Monitoring*, vol. 8, no. 3, pp. 223–241, 2009.
- [29] M. Rosenblatt, "Remarks on some nonparametric estimates of a density function," *Annals of Mathematical Statistics*, vol. 27, no. 3, pp. 832–837, 1956.
- [30] E. Parzen, "On estimation of a probability density function and mode," *Annals of Mathematical Statistics*, vol. 33, no. 3, pp. 1065–1076, 1962.
- [31] D. W. Scott, "On optimal and data-based histograms," *Biometrika*, vol. 66, no. 3, pp. 605–610, 1979.
- [32] B. W. Silverman, *Density Estimation for Statistics and Data Analysis*, Monographs on Statistics and Applied Probability, Chapman & Hall, CRC Press, London, UK, 1998.
- [33] R. L. Graham, D. E. Knuth, and O. Patashnik, *Concrete Mathematics*, Addison-Wesley, Reading, Mass, USA, 2nd edition, 1994.
- [34] Z. I. Botev, J. F. Grotowski, and D. P. Kroese, "Kernel density estimation via diffusion," *Annals of Statistics*, vol. 38, no. 5, pp. 2916–2957, 2010.
- [35] P. Chaudhuri and J. S. Marron, "Scale space view of curve estimation," *Annals of Statistics*, vol. 28, no. 2, pp. 408–428, 2000.
- [36] S. Larsson and V. Thomée, *Partial Differential Equations with Numerical Methods*, vol. 45 of *Texts in Applied Mathematics*, Springer, Berlin, Germany, 2003.
- [37] M. P. Wand and M. C. Jones, *Kernel Smoothing*, vol. 60 of *Monographs on Statistics and Applied Probability*, Chapman & Hall, London, UK, 1995.
- [38] H. W. Lilliefors, "On the Kolmogorov-Smirnov test for the exponential distribution with mean unknown," *Journal of the American Statistical Association*, vol. 64, no. 325, pp. 387–389, 1969.

Research Article

Higher-Harmonic Generation Analysis in Complex Waveguides via a Nonlinear Semianalytical Finite Element Algorithm

Claudio Nucera and Francesco Lanza di Scalea

*Department of Structural Engineering, University of California, San Diego,
9500 Gilman Drive, M.C. 0085, La Jolla, CA 92093-0085, USA*

Correspondence should be addressed to Claudio Nucera, cnucera@ucsd.edu

Received 7 April 2012; Accepted 10 May 2012

Academic Editor: Ivan Bartoli

Copyright © 2012 C. Nucera and F. Lanza di Scalea. This is an open access article distributed under the Creative Commons Attribution License, which permits unrestricted use, distribution, and reproduction in any medium, provided the original work is properly cited.

Propagation of nonlinear guided waves is a very attracting phenomenon for structural health monitoring applications that has received a lot of attention in the last decades. They exhibit very large sensitivity to structural conditions when compared to traditional approaches based on linear wave features. On the other hand, the applicability of this technology is still limited because of the lack of a solid understanding of the complex phenomena involved when dealing with real structures. In fact the mathematical framework governing the nonlinear guided wave propagation becomes extremely challenging in the case of waveguides that are complex in either materials (damping, anisotropy, heterogeneous, etc.) or geometry (multilayers, geometric periodicity, etc.). The present work focuses on the analysis of nonlinear second-harmonic generation in complex waveguides by extending the classical Semianalytical Finite Element formulation to the nonlinear regime, and implementing it into a powerful commercial Finite Element package. Results are presented for the following cases: a railroad track and a viscoelastic plate. For these case-studies optimum combinations of primary wave modes and resonant double-harmonic nonlinear wave modes are identified. Knowledge of such combinations is critical to the implementation of structural monitoring systems for these structures based on higher-harmonic wave generation.

1. Introduction

Traditional techniques in nondestructive evaluation and structural health monitoring applications rely on measuring “linear” parameters of the waves (amplitude, speed, and phase shifts) to infer salient features of the inspected structure. Several studies, however, have shown that “nonlinear” parameters are, in general, more sensitive to structural condition than linear parameters [1]. Furthermore, the use of nonlinear guided waves is extremely attractive because guided waves combine the mentioned high sensitivity typical of nonlinear parameters with large inspection ranges [2–9].

From a mathematical standpoint, the framework behind nonlinear guided waves propagation is relatively challenging since the Navier elastodynamic equations are further complicated by stress-free conditions at the waveguide's cross-sectional boundaries. For this reason, most of the previous works on elastic waves in waveguide solids considered the propagation to be in the linear elastic regime with the assumption of infinitesimal deformations (coincidence between deformed and initial configurations). However, as the amplitude of the wave increases or the structure starts experiencing finite deformations (i.e., nonlinear elasticity) or another cause of nonlinear effects is present, the nonlinearity in the structural response becomes relevant and must be introduced in the analysis. Hence cubic (and eventually higher-order) terms in the particle displacements gradients must be included in the elastic strain energy density expression [10, 11].

Among the manifestations of the nonlinear behavior, higher-harmonic generation is considered in detail in the present work. In this scenario, supposing to excite an ultrasonic wave into the waveguide structure at a fixed frequency, ω (Fundamental Frequency), the nonlinearity manifests itself in the generation of multiple harmonics of ω , for example, 2ω (second harmonic), 3ω (third harmonic), and so on. For a practical use, this nonlinearity can be quantified via an ultrasonic nonlinear parameter, β , well documented in literature [2].

In the last thirty years, several successful applications of nonlinear guided waves have been discussed, spanning from assessing the fatigue damage of metals [12–14] and concrete [15], to the efficient location of internal cracks and dislocations [16–20]. The authors of the present paper recently exploited the features of nonlinear guided wave propagation in seven-wire steel strands and proposed a methodology to measure the stress level acting on these structural elements based on the theory of contact acoustic nonlinearity [21].

While several investigations pertaining to nonlinear effect in solids and second harmonic generation were reported in the past [22, 23], most of them were limited in their applicability to structures with simple geometries (plates, rods, and shells) where analytical solutions for the primary (linear) wave field are available in literature. Very few studies tried to analyze the nonlinear wave propagation phenomena in geometrically complex waveguides using specialized SAFE codes [24].

In the present work, the propagation of waves in nonlinear solid waveguides with complex geometrical and material properties is investigated theoretically and numerically. For the solution of the nonlinear boundary value problem, perturbation theory and modal expansion are used [22]. The main novelty consists in the development of a powerful numerical algorithm, able to efficiently predict and explore the nonlinear wave propagation phenomena in several types of structural waveguides. It is based on the implementation of a nonlinear semianalytical finite element formulation into a commercial multipurpose finite element package. Compared to the classical finite element formulation, the proposed solution is computationally more efficient since it simply requires the finite element discretization of the cross-section of the waveguide and assumes harmonic motion along the wave propagation direction. Furthermore, compared to traditional spectral or waveguide element method approaches, no new elements need to be developed, the full power of ready-to-use high-order shape functions (crucial for the development of the present theory) can be easily exploited through friendly GUI, and immediate and extensive postprocessing for all the required quantities can be developed.

The applicability of the proposed analysis is quite wide, since it can efficiently handle general prismatic structures, viscoelastic waveguides with damping effects, multilayered composite laminate panels, and heterogeneous systems, all cases where theoretical wave solutions are either nonexistent or extremely difficult to determine. In addition, the proposed

approach requires simple modifications to the original commercial FEM code so that the nonlinear semianalytical formulation can be taken into account and translated to match the required formalism. After a brief discussion on the background of the present work and the proposed algorithm, two case studies have been analyzed in detail: a railroad track and a viscoelastic plate. They were considered to show the potential of the algorithm in handling complex geometry as well as viscoelastic material properties. The proposed code was successful in identifying optimal combinations of resonant primary and secondary modes. The knowledge of these nonlinear resonance conditions is of paramount importance for the actual implementation of conditions assessment systems for these structures that are based on the measurement of nonlinear ultrasonic guided waves.

2. Nonlinear Guided Waves Propagation

In the present section, a brief overview of the generalized nonlinear theory of elasticity for wave propagation involving finite deformations is presented [25]. Following [22], assuming that the body is homogeneous, isotropic, and hyperelastic, it possesses a strain energy density ε which is an analytic function of the Green-Lagrange strain tensor E_{ij} via its invariants; in this scenario, the Second Piola-Kirchhoff stress tensor S_{ij} can be expressed as:

$$S_{ij} = \rho_0 \frac{\partial \varepsilon}{\partial E_{ij}}, \quad (2.1)$$

where ρ_0 is the initial density of the body.

According to finite strain theory, in (2.1) we have assumed the following:

$$E_{ij} = \frac{1}{2} (u_{i,j} + u_{j,i} + u_{k,i} u_{k,j}), \quad u_{i,j} = \frac{\partial u_i}{\partial x_j}. \quad (2.2)$$

The strain energy density expression becomes

$$\varepsilon = \frac{1}{2} \lambda I_1^2 + \mu I_2 + \frac{1}{3} C I_1^3 + B I_1 I_2 + \frac{1}{3} A I_3 + O(E_{ij}^4), \quad (2.3)$$

where I_1 , I_2 , and I_3 are the first three invariants of the Green-Lagrange strain tensor defined as $I_1 = E_{ii}$, $I_2 = E_{ij} E_{ji}$, and $I_3 = E_{ij} E_{jk} E_{ki}$; λ and μ are the Lamé elastic constants and A , B , and C are the Landau-Lifshitz third-order elastic constants [26].

In (2.3), first-order material nonlinearity was introduced through A, B, C , and geometric nonlinearity through E_{ij} . By substituting (2.3) into (2.1), and keeping up to second-order terms in E_{ij} , the nonlinear hyperelastic constitutive equation reads

$$S_{ij} = \lambda E_{kk} \delta_{ij} + 2\mu E_{ij} + \delta_{ij} (C E_{kk} E_{ll} + B E_{kl} E_{lk}) + 2B E_{kk} E_{ij} + A E_{jk} E_{ki}. \quad (2.4)$$

Using (2.4) in the general momentum equation, the nonlinear boundary value problem governing the propagation of nonlinear elastic waves in isotropic, homogeneous and hyperelastic waveguides can be formulated as [10]:

$$\begin{aligned} \rho_0 \ddot{u}_i - \mu u_{i,kk} - (\lambda + \mu) u_{l,li} = & \left(\mu + \frac{A}{4} \right) (u_{l,kk} u_{l,i} + u_{l,kk} u_{i,l} + 2u_{i,lk} u_{l,k}) \\ & + \left(\lambda + \mu + \frac{A}{4} + B \right) (u_{l,ik} u_{l,k} + u_{k,lk} u_{i,l}) + (\lambda + B) u_{i,kk} u_{l,l} \\ & + \left(\frac{A}{4} + B \right) (u_{k,lk} u_{l,i} + u_{l,ik} u_{k,l}) + (B + 2C) u_{k,ik} u_{l,l}. \end{aligned} \quad (2.5)$$

Characterizing the system of (2.5) to the “guided” wave propagation case (stress-free boundary condition), the governing equations can be recast in vector notation as:

$$\begin{aligned} (\lambda + 2\mu) \nabla (\nabla \cdot \mathbf{u}) - \mu \nabla \times (\nabla \times \mathbf{u}) + \mathbf{f} &= \rho_0 \frac{\partial^2 \mathbf{u}}{\partial t^2}, \\ S_L(\mathbf{u}) \cdot \mathbf{n}_r &= -\bar{S}(\mathbf{u}) \cdot \mathbf{n}_r \quad \text{on } \Gamma, \end{aligned} \quad (2.6)$$

where \mathbf{u} is the particle displacement vector, ρ_0 , λ and μ are defined above, \mathbf{f} is the nonlinear term acting as a body force, \mathbf{n}_r is the unit vector normal to the surface of the waveguide Γ , and S_L and \bar{S} are the linear and nonlinear parts of the second Piola-Kirchhoff stress tensor, respectively. The nonlinear waveguide system is illustrated in Figure 1.

Considering higher harmonics up to the second order, the nonlinear boundary value problem presented in (2.6) is solved using perturbation theory. The solution of the primary wave field can be obtained analytically for simple geometries (plates, rods, shells, etc.) and numerically using the classical SAFE formulation for waveguides with generic cross-section [27]. Following [22, 28], if ω is the primary frequency that is excited into the system, the first-order nonlinear solution is calculated through modal expansion using the existing propagating guided modes 2ω as:

$$\mathbf{v}(x, y, z, t) = \frac{1}{2} \sum_{m=1}^{\infty} A_m(z) \mathbf{v}_m(x, y) e^{-i2\omega t} + \text{c.c.}, \quad (2.7)$$

where (x, y) are the cross-sectional coordinates of the waveguide, z is the lengthwise coordinate of the waveguide, c.c. denotes complex conjugates, \mathbf{v}_m is the particle velocity vector referred to the m th mode at 2ω , and A_m is the higher-order modal amplitude given by:

$$A_m(z) = \bar{A}_m(z) e^{i(2kz)} - \bar{A}_m(0) e^{ik_n^* z}, \quad (2.8)$$

where k represents the wavenumber. The amplitude $A_m(z)$ quantifies how strong is the excitation of the m th secondary mode in the modal expansion.

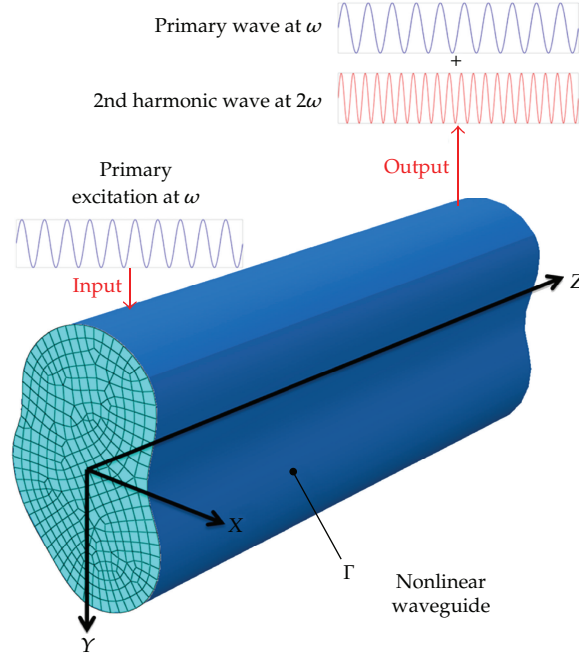


Figure 1: Generic nonlinear waveguide (finite element mesh just on the cross section) with second harmonic generation highlighted.

In (2.8), the amplitude of the secondary modes is expressed in two different forms depending on the existence or not of the phase-matching condition (synchronism). The latter occurs between two modes having the same phase velocity. The expressions are

$$\overline{A}_m(z) = i \frac{(f_n^{\text{vol}} + f_n^{\text{surf}})}{4P_{mn}(k_n^* - 2k)} \quad \text{if } k_n^* \neq 2k \text{ (ASYNCHRONISM)}, \quad (2.9)$$

$$\overline{A}_m(z) = \frac{(f_n^{\text{vol}} + f_n^{\text{surf}})}{4P_{mn}} z \quad \text{if } k_n^* = 2k \text{ (SYNCHRONISM)}, \quad (2.10)$$

where P_{mn} is the complex power flow along the direction of wave propagation and f_n^{vol} and f_n^{surf} are identified as the complex external power due to surface sources and volume force, respectively.

It is possible to notice how the nonlinearity of the waveguide transforms a monochromatic (single frequency) wave input into a distorted output where primary wave and second harmonic coexist (Figure 1). Furthermore the modal amplitude of the generic m th secondary mode oscillates in value if the solution is asynchronous, while it increases with propagation distance z if the solution is synchronous. The latter is the known cumulative behavior occurring for nonlinear resonant modes. Further details concerning the terms appearing in (2.9)-(2.10) can be found in [22]. The internal resonance mechanism relies on the simultaneous occurrence of two conditions, namely:

- (1) Phase matching: $k_n^* = 2k$.
- (2) Nonzero power transfer from primary to secondary wave field: $f_n^{\text{surf}} + f_n^{\text{vol}} \neq 0$.

Recent investigations performed by Deng et al. have analyzed the influence of an additional requirement for the occurrence of internal resonance, namely, the group velocity matching [29]. In this study, the authors showed analytically and experimentally that, as long as the two aforementioned conditions (phase-matching and nonzero power transfer) are satisfied, the cumulative effect of the secondary resonant mode takes place even when the group velocity matching condition is not satisfied. They concluded that group velocity matching does not represent a necessary requirement for cumulative second-harmonic generation. For this reason in the present work, phase-matching and power transfer only are considered in detail.

In nonlinear structural monitoring, the key consists of the identification of an optimal combination of synchronous primary and secondary modes. The rest of this paper presents a numerical tool that enables to identify these resonant conditions for various complex waveguides, that would be extremely difficult to study by other means, and that include cases of periodic structures, damped structures, multilayered geometries and heterogeneous structures.

3. Nonlinear Semianalytical Finite Element Algorithm

Linear SAFE formulation has shown in the past its great potential in calculating the dispersion characteristics of complex waveguides (where the analytical solution is not available) in a very efficient way [27, 30]. The knowledge of these curves is the starting point for the development of any application based on the use of guided waves. The present work focuses on the extension of this approach to the nonlinear regime and its implementation, into a highly flexible COMSOL commercial code, of a nonlinear SAFE formulation to solve complex waveguides (CO.NO.SAFE Algorithm).

The implementation combines the full power of existing libraries and routines of the commercial code with its ease of use and extremely capable postprocessing functions; hence internal resonance conditions of structural waveguides with different level of complexity can be conveniently analyzed via user-friendly interfaces. Furthermore, since all the nonlinear parameters involve gradients of the displacement field up to the third order, high-order finite elements (at least cubic) need to be used in order to obtain meaningful results; this task is not trivial to implement in general SAFE algorithms.

Starting from the nonlinear boundary value problem stated in (2.6), the displacement field is approximated in the cross-section of the waveguide (x, y) and is enforced to be harmonic in time and along the direction of wave propagation (z) in accordance with the classical SAFE formulation. For the generic e th element, this condition reads

$$u^e(x, y, z, t) = N^e(x, y)U^e e^{i(kz - \omega t)}, \quad (3.1)$$

where $N^e(x, y)$ is the matrix of shape functions, t is time, k is the wavenumber, and U^e is the nodal displacement vector for the e th element. The enforcement of this particular displacement field in (2.6) constitutes the main modification that needs to be applied in the original cross-sectional FEM formulation. Hence, after the original quadratic eigenvalue problem in wavenumbers has been reformulated in a linear fashion by doubling the space dimension [27], the nonlinear boundary value problem can be implemented in COMSOL using the general PDE solver engine [31]. COMSOL formalism for the boundary value

Table 1: Material properties assumed for the railroad track analysis.

ρ (kg/m ³)	λ (GPa)	μ (GPa)	A (GPa)	B (GPa)	C (GPa)
7932	116.25	82.754	-340	-646.667	-16.667

problem with Neumann boundary conditions (which correspond to the guided wave propagation) is

$$\nabla \cdot (c \nabla U + \alpha U - \gamma) - \beta \cdot \nabla U - aU + \lambda d_a U = 0, \quad (3.2)$$

$$n \cdot (c \nabla U + \alpha U) + qU = 0, \quad (3.3)$$

where n is the outward unit normal vector on the surface of the waveguide, c is the diffusion coefficient, α is the conservative flux convection coefficient, d_a is a damping coefficient, β is the convection coefficient, a is the absorption coefficient, γ is the conservative flux source term, f is the source term, q is the boundary absorption term, λ is the eigenvalue and U represents the set of dependent variables to be determined. All these coefficients generally admit complex values (appropriate for viscoelastic materials) [32]. The formalism introduced in (3.2)-(3.3) is very general and can be used for a broad range of physical problems governed by a system of PDEs, once every coefficient has been conveniently characterized to the particular physics governing the considered problem.

Once all the parameters have been defined, dispersion curves for the selected waveguide can be promptly calculated. Next, after a particular frequency has been selected as primary excitation, second harmonic generation and internal resonance occurrence can be analyzed.

In the next section, the proposed algorithm is benchmarked with two case studies of interest in structural engineering.

4. Applications

4.1. Railroad Track

A136RE railroad track was considered first for this study. Due to the complex geometry of the cross section, solutions for the dispersion curves and, consequently, for the higher harmonic generation analysis cannot be calculated analytically. After a preliminary study involving the selection and the analysis of internal resonance conditions for several primary-secondary wave field combinations, two exemplary cases were selected as representative. In the first case, phase matching between primary and secondary modes is verified. However, due to the characteristic energy distribution over the rail cross-section, no power transfer is present between the modes and, consequently, internal resonance does not occur; hence, the secondary modal amplitude is bound in value and oscillates with distance along the direction of wave propagation (3.1). In the second case, instead, both required conditions are verified and internal resonance takes place, leading to a resonant secondary wave field growing linearly with wave propagation distance.

The material properties considered are given in Table 1. The Landau-Lifshitz third-order elastic constants are detailed in [33].

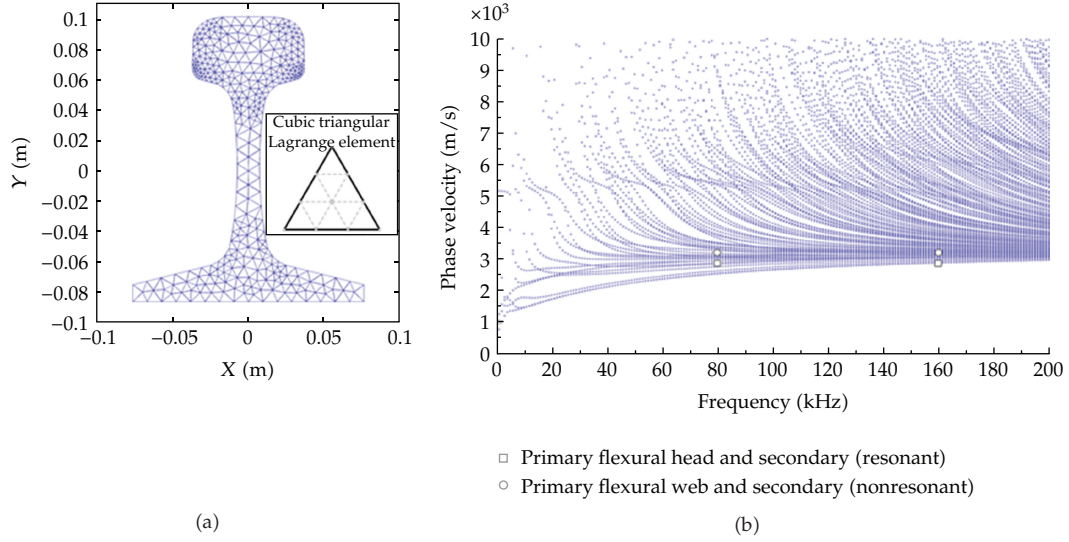


Figure 2: (a) Geometry and finite element mesh adopted for the railroad track nonlinear analysis. (b) Phase-velocity dispersion curve in the $(0 \div 200)$ kHz frequency range with selected combinations of primary and secondary modes pinpointed.

The geometry of the railroad track cross-section, with the FE mesh used for the analysis, is shown in Figure 2(a). To correctly explore the displacement field and all the derived quantities (essential for the calculation of all the terms during the nonlinear postprocessing), 618 cubic Lagrangian triangular isoparametric finite elements were employed [34]. In Figure 2(b), the resultant phase-velocity dispersion curve in the $(0 \div 200)$ kHz frequency range is represented. As detailed in the following, the same figure also pinpoints the two selected combinations of primary and secondary modes as exemplary cases for the internal resonance analysis.

The complexity of the guided wave propagation for this particular waveguide is evident considering the abundance of propagative modes present and their dispersion characteristics (especially at higher frequencies). Selecting a primary excitation frequency of 80 kHz, the eigenvalue problem has been solved, and 500 propagative modes (real eigenvalues) have been extracted at ω (80 kHz) and at 2ω (160 kHz). Next, Figure 3 shows some propagative modes found in this specific frequency range. It can be noted how differently the energy is concentrated within the waveguide.

4.1.1. Nonresonant Combination

A flexural horizontal primary mode was selected as primary excitation (input for the CO.NO.SAFE algorithm). The nonlinear analysis revealed the presence of a synchronous secondary mode at 2ω (similar flexural horizontal displacement distribution). However, the second required condition concerning the power transfer is not met for this particular combination, leading to an oscillating secondary modal amplitude value and absence of internal resonance. At the same time, a conspicuous power transfer is present between the selected primary mode and some asynchronous secondary modes; here again, because of the lack of one of the two essential requirements (phase matching) internal resonance does

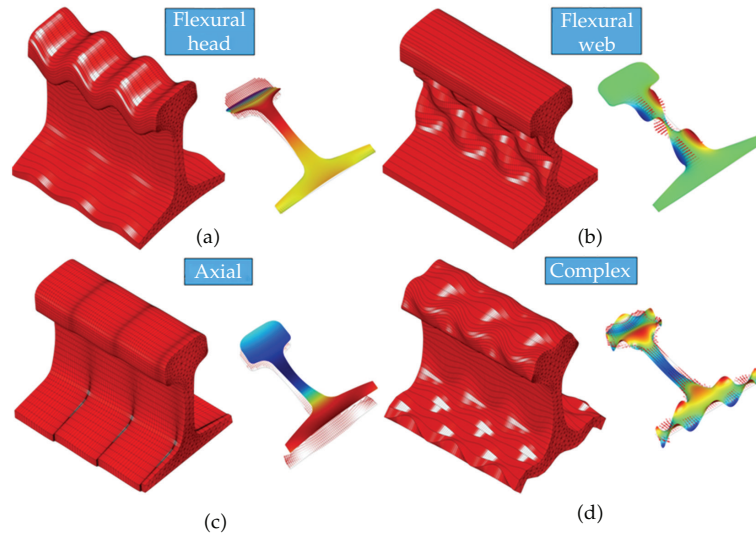


Figure 3: Propagative modes in the $(80 \div 160)$ kHz frequency range. (a) Flexural vertical mode (energy mainly concentrated in the rail's head). (b) Flexural horizontal mode (energy exclusively, confined in the rail's web). (c) Axial mode. (d) Complex mode involving a mixture of axial, torsional, and flexural displacements (color online).

not take place. This fact translates into the very small value associated of modal amplitude associated with the only synchronous mode and the relatively higher values associated to the asynchronous secondary modes.

The following Figures 4(a) and 4(b) illustrate the selected primary and secondary modes, respectively. Figure 4(c) plots the modal amplitude results as calculated from (3.2) for the propagative secondary modes present at 160 kHz.

4.1.2. Resonant Combination

In this case a flexural vertical mode was selected as primary excitation. The results of the nonlinear SAFE analysis disclosed the presence of some synchronous secondary modes with one in particular (slightly different flexural vertical type) able to verify both requirements producing internal resonance and a nonlinear double harmonic growing linearly with distance. As in the previous case, Figures 5(a)-5(b) display the selected modes, while Figure 5(c) spotlights the very high value of modal amplitude related to the secondary resonant mode; small amplitude values associated to the other synchronous modes, for which power transfer is absent, are also shown in the same figure.

The previous results point up an optimal combination of primary and secondary wave fields able to maximize the nonlinear response of the waveguide. Furthermore, it is worthwhile to notice how the selected primary mode is not only able to produce a resonant condition, but also very attractive in terms of practical excitability by a piezoelectric transducer.

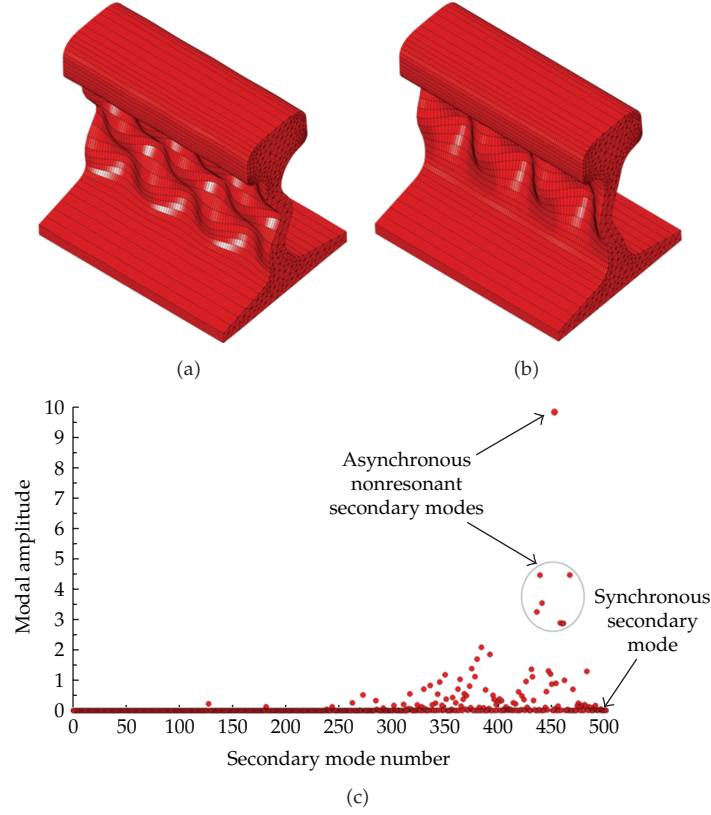


Figure 4: (a) Selected primary mode at 80 kHz. (b) Phase-matched (synchronous) but nonresonant secondary mode at 160 kHz. (c) Modal amplitude plot for propagative secondary modes.

Table 2: HPPE plate material properties.

ρ (kg/m ³)	h (mm)	c_L (m/s)	c_T (m/s)	k_L (Np/wavelength)	k_T (Np/wavelength)
953	12.7	2344	953	0.055	0.286

4.2. Viscoelastic Isotropic Plate

A viscoelastic isotropic high-performance polyethylene (HPPE) plate was investigated next to extend the applicability to dissipative waveguides. This system is of primary importance in aerospace and mechanical engineering and has been studied quite extensively in the past assuming linear elastic regime to obtain dispersion curves and associated waveguide modes [27, 35, 36]. In the present work, these results are confirmed and extended to the nonlinear regime; an efficient combination of resonant primary and secondary modes is identified and discussed in detail.

Material and geometrical properties for the plate are illustrated in Table 2 [35, 36], where ρ is the density, h is the thickness, c_L is the longitudinal bulk wave velocity, c_T is the shear bulk wave velocity, k_L is the longitudinal bulk wave attenuation, and k_T is the shear bulk wave attenuation.

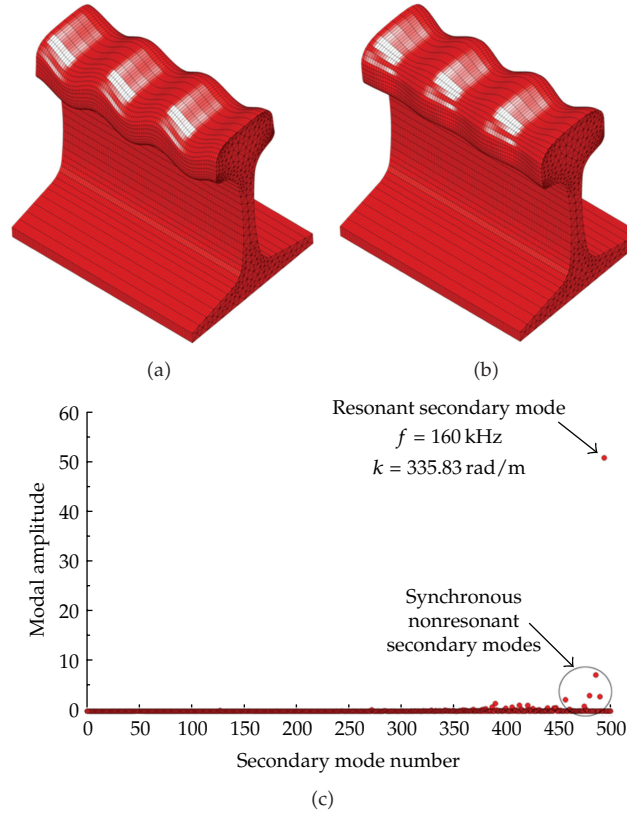


Figure 5: (a) Selected primary mode at 80 kHz. (b) Resonant secondary mode at 160 kHz. (c) Modal amplitude plot for secondary propagative modes.

The dissipative behavior of the plate was modeled via the Hysteretic formulation [27]. Hence, the resultant stiffness matrix is frequency-independent and was calculated just once at the beginning of the analysis once the complex Lamé's constants were evaluated. The results for the present case are

$$\begin{aligned}\tilde{\lambda} &= \frac{\rho \tilde{c}_T^2 ((3\tilde{c}_L^2 - 4\tilde{c}_T^2) / (\tilde{c}_L^2 - \tilde{c}_T^2)) \tilde{\nu}}{(1 + \tilde{\nu})(1 - 2\tilde{\nu})} = 3.51 + 0.06i, \text{ GPa}, \\ \tilde{\mu} &= \frac{\rho \tilde{c}_T^2 ((3\tilde{c}_L^2 - 4\tilde{c}_T^2) / (\tilde{c}_L^2 - \tilde{c}_T^2))}{2(1 + \tilde{\nu})} = 0.86 - 0.08i, \text{ GPa}.\end{aligned}\tag{4.1}$$

In (4.1) the complex bulk wave velocities (longitudinal and transverse) are calculated as follows:

$$\tilde{c}_{L,T} = \tilde{c}_{L,T} \left(1 + i \frac{k_{L,T}}{2\pi} \right)^{-1}.\tag{4.2}$$

The resultant viscoelastic stiffness matrix, with terms expressed in GPa, is given by:

$$\tilde{C} = \begin{bmatrix} \tilde{\lambda} + 2\tilde{\mu} & \tilde{\lambda} & \tilde{\lambda} & 0 & 0 & 0 \\ \tilde{\lambda} & \tilde{\lambda} + 2\tilde{\mu} & \tilde{\lambda} & 0 & 0 & 0 \\ \tilde{\lambda} & \tilde{\lambda} & \tilde{\lambda} + 2\tilde{\mu} & 0 & 0 & 0 \\ 0 & 0 & 0 & \tilde{\mu} & 0 & 0 \\ 0 & 0 & 0 & 0 & \tilde{\mu} & 0 \\ 0 & 0 & 0 & 0 & 0 & \tilde{\mu} \end{bmatrix} \quad (4.3)$$

$$= \begin{bmatrix} 5.23 - 0.09i & 3.51 + 0.06i & 3.51 + 0.06i & 0 & 0 & 0 \\ 3.51 + 0.06i & 5.23 - 0.09i & 3.51 + 0.06i & 0 & 0 & 0 \\ 3.51 + 0.06i & 3.51 + 0.06i & 5.23 - 0.09i & 0 & 0 & 0 \\ 0 & 0 & 0 & 0.86 - 0.08i & 0 & 0 \\ 0 & 0 & 0 & 0 & 0.86 - 0.08i & 0 \\ 0 & 0 & 0 & 0 & 0 & 0.86 - 0.08i \end{bmatrix}.$$

First, the plate system was solved in the linear regime in order to calculate the dispersion curves and obtain the propagative modes, necessary for the nonlinear analysis. For this purpose, an extension of the linear SAFE algorithm [32] was employed. It allows the study of the guided wave propagation along structures exhibiting material/geometrical periodicity along their width (which is normal to the direction of propagation and to the thickness and considered infinite) by applying the so-called periodic boundary conditions (PBCs). With this powerful tool, a generally complex periodic structure (grooved panel, reinforced concrete elements, just to mention a couple) can be modeled simply by considering a very small cell and applying PBCs on its sides. Mathematically, they represent a particular case of Neumann boundary conditions: the variables and their derivatives up to the element order are forced to take identical values on the pair of boundaries of the structure where the PBCs are applied. This tool is very attractive since it opens new possibilities to study the guided wave propagation (linear and nonlinear) for a general class of periodic structures by developing the analysis just on a small portion (periodic cell).

According to this approach, the present plate system was modeled using a mesh of just 60 quadrilateral cubic Lagrangian elements mapped and deployed in a (3.17×12.7) mm periodic cell (Figure 6(a)). The resulting Lamb wave solutions are displayed in Figures 6(b)-6(c) in the $(0 \div 500)$ kHz frequency range. They are found to be in perfect agreement with well-known results previously published in literature. Primary and secondary modes for the nonlinear analysis are highlighted with white circles in the same figures.

Due to the lack of studies in literature concerning specifically the HPPE material, the third-order Landau-Lifshitz elastic constants of a very similar plastic polymer (Polystyrene) were adopted for the nonlinear analysis [37]. The assumed values are $A = -10.8$ GPa, $B = -7.85$ GPa, and $C = -9.81$ GPa.

The nonlinear analysis was developed between 250 kHz (primary mode) and 500 kHz (secondary mode). The waveguide being dissipative, all the eigenvalues and eigenvectors are complex. Propagative modes were separated from evanescent and nonpropagative solutions by using a threshold of 10% between imaginary and real parts of each eigenvalue. After a preliminary analysis on different potential combinations among the propagative modes, one particular mode was selected as input (primary mode) for the nonlinear postprocessing. It is

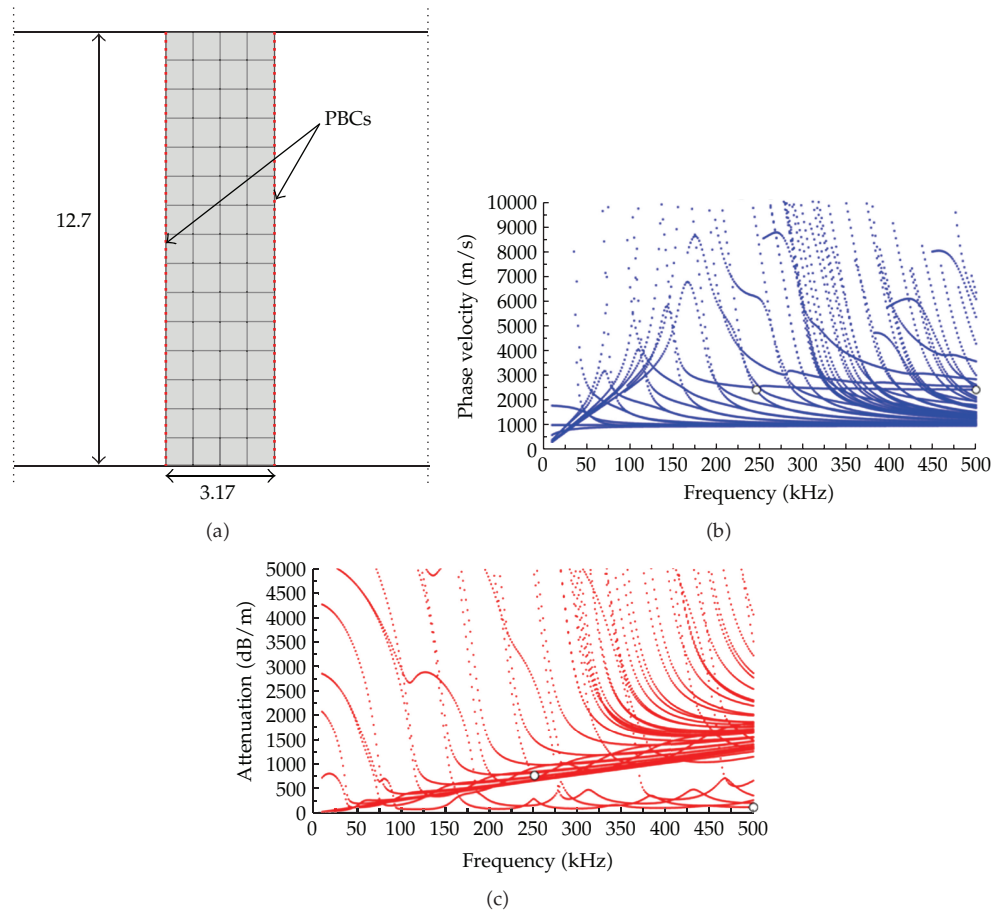


Figure 6: (a) Geometry with associated mesh for the 2D periodic cell representative of the 12.7 mm thick HPPE plate (dimensions in mm). (b) Phase-velocity dispersion curve in the (0 ÷ 500) kHz frequency range with primary and secondary modes for nonlinear analysis highlighted (white circles). (c) Attenuation curve (expressed in dB/m) in the (0 ÷ 500) kHz frequency range with primary and secondary modes for nonlinear analysis highlighted (white circles).

associated with a complex eigenvalue $k = 669.62 + 87.56i$ and a corresponding phase velocity $c_{ph} = 2345.80$ m/s at 250 kHz.

The application of the CO.NO.SAFE algorithm in this case is simplified because of the assumption of 2D strain regime (the plate is considered infinite in the width direction). For this reason all the terms used in the nonlinear postprocessing discussed before are evaluated on a line segment running through the thickness. This approach is sometimes referred as 1D SAFE [32], and was first introduced almost four decades ago [38, 39].

The results of the analysis pinpointed the presence of a resonant secondary mode. As mentioned before, while the contribution of all other modes is oscillatory and bounded (2.9), this secondary mode shows a cumulative behavior and represents the dominant term in the expansion equation (2.7) with a contribution that linearly increases with distance. In fact, after all the secondary modal amplitudes were calculated from (2.10) for the synchronous case, the identified resonant secondary mode exhibits a value which is orders of magnitude

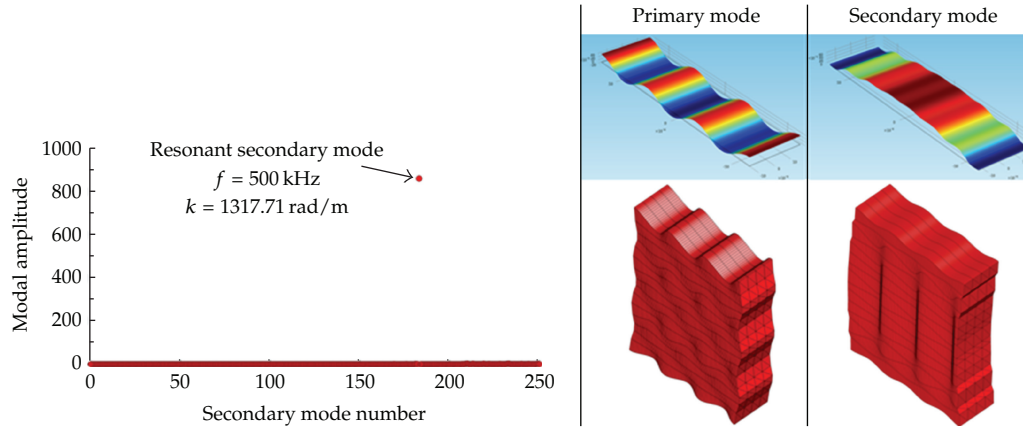


Figure 7: Modal amplitude plot for secondary propagative modes along with contour plots and 3D views of the selected primary and secondary modes for the viscoelastic HPPE plate (color online).

larger than those associated to the asynchronous modes (Figure 7). The same figure also illustrates primary and secondary modes as contour plots (height and color gradients are proportional to the out-of-plane displacement component along the propagation direction) and 3D rendered views (global modeshape) considering a length of 1 cm. The amplitudes of the displacement fields are not normalized and, consequently, they supply exact information about the mode shapes. At the same time, the values are therefore not comparable from one mode to another.

Figure 7 shows that the selected primary mode is a complex axial symmetric mode. The mode at the double harmonic shows also features typical of axial modes. This resonant secondary mode at 500 kHz looks very promising in a possible structural monitoring system because it keeps the majority of the energy in the central area of the cross-section and minimizes wave leakage into the surrounding medium. Furthermore, Figure 6(c) shows that both primary and secondary modes have very small attenuation values (especially the secondary mode at 500 kHz); this fact makes the studied combination even more attractive because of the large inspection range that can potentially be achieved.

5. Conclusions

Nondestructive evaluation and structural health monitoring communities are showing an increasing interest in nonlinear guided waves because of their significant potential in several applications. However, proper application of nonlinear features requires a complete understanding of the higher-harmonic generation phenomenon that can be expected for the test waveguide. This paper discussed the extension of the classical SAFE algorithm to the nonlinear regime and its implementation in a powerful multipurpose commercial FEM code (COMSOL). The result is an innovative tool that opens new possibilities for the analysis of dispersion characteristics and, most importantly here, nonlinear internal resonance conditions, for a variety of complex structural waveguides that do not lend themselves to alternative analyses such as purely analytical solutions. The specific cases that were examined in this paper include complex geometry (railroad track) and viscoelastic waveguides with damping effects (HPPE plate). In all these cases, the proposed algorithm

successfully identified optimal combinations of resonant primary and secondary wave modes that exhibit the desired conditions of synchronicity and large cross-energy transfer. These properties can be exploited in an actual system aimed at monitoring the structural condition of the waveguide by nonlinear waves (detect defects, measure quasi-static loads or instability conditions, etc.).

Acknowledgments

This paper was funded by Federal Railroad Administration Grant number FR-RRD-0009-10-01 (Mahmood Fateh, Program Manager) and by National Science Foundation Grant number ECCS-1028365 (George Maracas, Program Manager).

References

- [1] Dace, G. E. Thompson, R. B. Brasche, L. J. H. Rehbein, and D. K. Buck, "Nonlinear acoustic, a technique to determine microstructural changes in material," *Review of Progress in Quantitative Nondestructive Evaluation (QNDE)*, vol. 10, pp. 1685–1692, 1991.
- [2] C. Bermes, J. Y. Kim, J. Qu, and L. J. Jacobs, "Experimental characterization of material nonlinearity using Lamb waves," *Applied Physics Letters*, vol. 90, no. 2, Article ID 021901, 2007.
- [3] P. Cawley and D. Alleyne, "The use of Lamb waves for the long range inspection of large structures," *Ultrasonics*, vol. 34, no. 2–5, pp. 287–290, 1996.
- [4] J. L. Rose, *Ultrasonic Waves in Solid Media*, Cambridge University Press, Cambridge, UK, 1999.
- [5] J. L. Rose, "Standing on the shoulders of giants: an example of guided wave inspection," *Materials Evaluation*, vol. 60, no. 1, pp. 53–59, 2002.
- [6] R. Ahmad, S. Banerjee, and T. Kundu, "Pipe wall damage detection in buried pipes using guided waves," *Journal of Pressure Vessel Technology, Transactions of the ASME*, vol. 131, no. 1, pp. 0115011–01150110, 2009.
- [7] T. Kundu, S. Das, and K. V. Jata, "Health monitoring of a thermal protection system using lamb waves," *Structural Health Monitoring*, vol. 8, no. 1, pp. 29–45, 2009.
- [8] H. Reis, *Nondestructive Testing and Evaluation for Manufacturing and Construction*, Hemisphere, New York, NY, USA, 1990.
- [9] T. Kundu, S. Banerjee, and K. V. Jata, "An experimental investigation of guided wave propagation in corrugated plates showing stop bands and pass bands," *Journal of the Acoustical Society of America*, vol. 120, no. 3, pp. 1217–1226, 2006.
- [10] Z. A. Goldberg, "Interaction of plane longitudinal and transverse elastic waves," *Soviet Physics. Acoustics*, pp. 306–310, 1960.
- [11] L. K. Zarembo and V. A. Krasil'nikov, "Nonlinear phenomena in the propagation of elastic waves in solids," *Soviet Physics USPEKHI*, vol. 13, no. 6, pp. 778–797, 1971.
- [12] J. H. Cantrell, "Quantitative assessment of fatigue damage accumulation in wavy slip metals from acoustic harmonic generation," *Philosophical Magazine*, vol. 86, no. 11, pp. 1539–1554, 2006.
- [13] J. H. Cantrell and W. T. Yost, "Nonlinear ultrasonic characterization of fatigue microstructures," *International Journal of Fatigue*, vol. 23, no. 1, pp. S487–S490, 2001.
- [14] W. T. Yost and J. H. Cantrell, "The effects of fatigue on acoustic nonlinearity in aluminum alloys," *Proceedings of the IEEE*, vol. 2, pp. 947–954, 1992.
- [15] A. A. Shah and Y. Ribakov, "Non-linear ultrasonic evaluation of damaged concrete based on higher order harmonic generation," *Materials and Design*, vol. 30, no. 10, pp. 4095–4102, 2009.
- [16] N. Kim et al., "Nonlinear behaviour of ultrasonic wave at a crack," in *Review of Progress in Quantitative Nondestructive Evaluation*, vol. 1211 of *AIP Conference Proceedings*, pp. 313–318, 2010.
- [17] I. Arias and J. D. Achenbach, "A model for the ultrasonic detection of surface-breaking cracks by the scanning laser source technique," *Wave Motion*, vol. 39, no. 1, pp. 61–75, 2004.
- [18] S. S. Kulkarni and J. D. Achenbach, "Structural health monitoring and damage prognosis in fatigue," *Structural Health Monitoring*, vol. 7, no. 1, pp. 37–49, 2008.
- [19] C. Bermes, J. Y. Kim, J. Qu, and L. J. Jacobs, "Nonlinear Lamb waves for the detection of material nonlinearity," *Mechanical Systems and Signal Processing*, vol. 22, no. 3, pp. 638–646, 2008.

- [20] S. K  chler, T. Meurer, L. J. Jacobs, and J. Qu, "Two-dimensional wave propagation in an elastic half-space with quadratic nonlinearity: a numerical study," *Journal of the Acoustical Society of America*, vol. 125, no. 3, pp. 1293–1301, 2009.
- [21] C. Nucera and F. Lanza Di Scalea, "Nonlinear ultrasonic guided waves for prestress level monitoring in prestressing strands for post-tensioned concrete structures," *Structural Health Monitoring-an International Journal*, vol. 10, no. 6, pp. 617–629, 2011.
- [22] W. J. N. De Lima and M. F. Hamilton, "Finite-amplitude waves in isotropic elastic plates," *Journal of Sound and Vibration*, vol. 265, no. 4, pp. 819–839, 2003.
- [23] M. Deng, "Analysis of second-harmonic generation of Lamb modes using a modal analysis approach," *Journal of Applied Physics*, vol. 94, no. 6, pp. 4152–4159, 2003.
- [24] A. Srivastava, I. Bartoli, S. Salamone, and F. Lanza Di Scalea, "Higher harmonic generation in nonlinear waveguides of arbitrary cross-section," *Journal of the Acoustical Society of America*, vol. 127, no. 5, pp. 2790–2796, 2010.
- [25] F. D. Murnaghan, *Finite Deformation of an Elastic Solid*, Dover, New York, NY, USA, 1967.
- [26] L. D. Landau and E. M. Lifshitz, *Theory of Elasticity*, Addison-Wesley, London, UK, 1959.
- [27] I. Bartoli, A. Marzani, F. Lanza di Scalea, and E. Viola, "Modeling wave propagation in damped waveguides of arbitrary cross-section," *Journal of Sound and Vibration*, vol. 295, no. 3–5, pp. 685–707, 2006.
- [28] B. A. Auld, "Application of microwave concepts to theory of acoustic fields and waves in solids," *IEEE Transactions on Microwave Theory and Techniques*, vol. 17, no. 11, pp. 800–811, 1969.
- [29] M. Deng, Y. Xiang, and L. Liu, "Time-domain analysis and experimental examination of cumulative second-harmonic generation by primary Lamb wave propagation," *Journal of Applied Physics*, vol. 109, no. 11, Article ID 113525, 2011.
- [30] T. Hayashi, W. J. Song, and J. L. Rose, "Guided wave dispersion curves for a bar with an arbitrary cross-section, a rod and rail example," *Ultrasonics*, vol. 41, no. 3, pp. 175–183, 2003.
- [31] COMSOL, COMSOL v4.2a Multiphysics User's Guide 2011: COMSOL, Inc. 1166.
- [32] M. V. Predoi, M. Castaings, B. Hosten, and C. Bacon, "Wave propagation along transversely periodic structures," *Journal of the Acoustical Society of America*, vol. 121, no. 4, pp. 1935–1944, 2007.
- [33] S. S. Sekoyan and A. E. Eremeev, "Measurement of the third-order elasticity constants for steel by the ultrasonic method," *Measurement Techniques*, vol. 9, no. 7, pp. 888–893, 1966.
- [34] E. Onate, *Structural Analysis with the Finite Element Method. Linear Statics* ?vol. 1, 2009.
- [35] A. Bernard, M. Deschamps, and M. J. S. Lowe, "Energy velocity and group velocity for guided waves propagating within an absorbing or non-absorbing plate in vacuum," in *Review of Progress in Quantitative NDE*, D. O. Thompson and D. E. Chimenti, Eds., vol. 18, pp. 183–190, Plenum Press, New York, NY, USA, 1999.
- [36] A. Bernard, M. J. S. Lowe, and M. Deschamps, "Guided waves energy velocity in absorbing and non-absorbing plates," *Journal of the Acoustical Society of America*, vol. 110, no. 1, pp. 186–196, 2001.
- [37] C. Cattani and Y. Y. Rushchitskii, *Wavelet and Wave Analysis as Applied to Materials with Micro or Nanostructure*, Series on Advances in Mathematics for Applied Sciences, World Scientific, Hackensack, NJ, USA, 2007.
- [38] S. B. Dong and R. B. Nelson, "High frequency vibrations and waves in laminated orthotropic plates," *Journal of Applied Mechanics, Transactions ASME*, vol. 39, no. 3, pp. 739–745, 1972.
- [39] R. B. Nelson and S. B. Dong, "High frequency vibrations and waves in laminated orthotropic plates," *Journal of Sound and Vibration*, vol. 30, no. 1, pp. 33–44, 1973.

Research Article

Wave Propagation Analysis in Composite Laminates Containing a Delamination Using a Three-Dimensional Spectral Element Method

Fuca Li, Haikuo Peng, Xuewei Sun, Jinfu Wang, and Guang Meng

State Key Laboratory of Mechanical System and Vibration, Shanghai Jiao Tong University, Shanghai 200240, China

Correspondence should be addressed to Fucai Li, fcli@sjtu.edu.cn

Received 30 December 2011; Revised 13 February 2012; Accepted 23 February 2012

Academic Editor: Zhongqing Su

Copyright © 2012 Fucai Li et al. This is an open access article distributed under the Creative Commons Attribution License, which permits unrestricted use, distribution, and reproduction in any medium, provided the original work is properly cited.

A three-dimensional spectral element method (SEM) was developed for analysis of Lamb wave propagation in composite laminates containing a delamination. SEM is more efficient in simulating wave propagation in structures than conventional finite element method (FEM) because of its unique diagonal form of the mass matrix. Three types of composite laminates, namely, unidirectional-ply laminates, cross-ply laminates, and angle-ply laminates are modeled using three-dimensional spectral finite elements. Wave propagation characteristics in intact composite laminates are investigated, and the effectiveness of the method is validated by comparison of the simulation results with analytical solutions based on transfer matrix method. Different Lamb wave mode interactions with delamination are evaluated, and it is demonstrated that symmetric Lamb wave mode may be insensitive to delamination at certain interfaces of laminates while the antisymmetric mode is more suited for identification of delamination in composite structures.

1. Introduction

Owing to its superior mechanical properties and light weight, composite materials are finding more and more applications especially in aerospace industries [1]. However, composite structures still run a high risk of suffering from damage due to abrupt impact or growth of fatigue defects, which can result in catastrophic failure during their service life. It is, therefore, essential to develop techniques to inspect integrity and improve safety, reliability, and operational life of structures [2–7].

Traditionally, nondestructive evaluation (NDE) techniques, such as C-scan and radiographic inspection, are used to evaluate the integrity and degradation of structures on a periodic basis. Now online structural health monitoring (SHM) techniques, for example,

vibration-based and Lamb-wave-based techniques, are being developed to provide early warning and assure the performance of structures. Among them, Lamb-wave-based techniques for damage detection have received a considerable attention in the past decades due to its ability of long-distance propagation and sensitivity to a variety of defects.

For Lamb waves-based damage detection techniques, understanding wave propagation characteristics in structures is essential for their successful application. Therefore, a number of numerical methods have been applied to analyze propagation of elastic waves, such as finite difference method (FDM) [8, 9], finite element method (FEM) [10–12], boundary element method (BEM) [13, 14], finite strip elements (FSE) [15, 16], mass-spring lattice model (MSLM) [17–21], and local interaction simulation approach (LISA) [22, 23].

In the literature, two kinds of spectral element method (SEM) were applied to wave propagation modeling, namely, fast-Fourier-transform- (FFT-) based SEM and the orthogonal polynomials-based SEM [24–26]. In the FFT-based SEM [24], a single element is sufficient to model wave propagation in large uniform structures, which is suited for simple 1D and 2D problems [27]. On the other hand, the orthogonal-polynomials- (e.g., Legendre and Chebysev polynomials) based SEM [25] is much more suitable for analyzing wave propagation in structures with complex geometry. The formulation of the spectral finite element (SFE) is similar to FE when assembly of element matrices and solution of equations are considered. Hence, the SEM can be used to handle the wave propagation in structures with complex geometry, and various types of defects can be modeled. The difference between the SEM and FEM comes in that orthogonal polynomials are used as approximation functions in SEM and, therefore, calculation can be more efficient because of the diagonal mass matrix. This method has been successfully applied to many fields, such as fluids, seismology and acoustics [28, 29]. More recently, the SEM was used to simulate wave propagation in structures for damage detection, for example, wave propagation in 1D structures, such as rod and beam [30, 31]. Numerical simulation results of the elastic wave propagation in a composite plate were presented by Kudela et al. [32]. A 2D spectral membrane finite element-based model, developed by Zak et al. [33], was used to analyze wave propagation in a cracked isotropic panel. Wave propagation in 2D plate structures using a 3D SEM for damage detection was also discussed by Peng et al. [34].

A wave propagation analysis in composite structures using 3D SEM for the purpose of damage detection has not been widely reported in the literature so far. Although characteristics of Lamb wave propagation in composite laminates and the damage evaluation using numerical simulation have been rigorously explored for a couple of years, in most of the related work, structures were simplified by either one- or two-dimensional models, resulting in approximate results especially for laminates of complicated layup or with damage. The SEM combines accuracy with flexibility in describing problems with complex geometries, which is highly desirable for modeling of elastic wave propagation. In this paper, multilayered composite laminates are modeled using the Legendre polynomials-based spectral finite element, elastic wave propagation characteristics are analyzed, and wave interaction with delamination is discussed.

2. Wave Propagation in Composite Plate

Composite laminates are commonly fabricated by stacking unidirectional lamina with a certain layup configuration. After a composite is properly cured, a multilayered structure is formed with all the layers bonded together. For analysis of wave propagation, each lamina

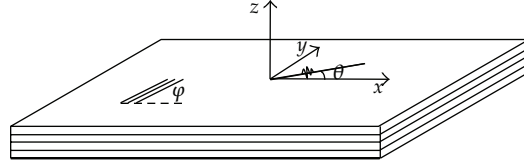


Figure 1: Sketch of a multilayered structure and the coordinate system.

can be regarded as a quasihomogeneous orthotropic or transversely isotropic material with the main principal axis parallel to the fibres. Therefore, in numerical calculations, a composite laminate is modeled as a multilayered medium with different elastic and anisotropic material properties [35].

In order to form a numerical model of composite structure, a Cartesian coordinate system is firstly defined by the z -axis normal to the central plane of a composite laminate spanned by the x -axis and the y -axis for modeling of the wave propagation, as shown in Figure 1.

For each layer of the composite laminate, the stress-strain relations for arbitrary direction have the following form [36]:

$$\boldsymbol{\sigma} = D\boldsymbol{\varepsilon}, \quad (2.1)$$

where $\boldsymbol{\sigma}$ is stress vector, $\boldsymbol{\varepsilon}$ is strain vector, and D is the flexibility matrix. In order to study wave propagation, the elastic constants of all the layers must be expressed in the global coordinate system. For those layers, the principal material coordinate system does not coincide with the global coordinate system; this can be achieved by using a transformation matrix method.

In a homogeneous media, the elastic wave propagation is described by the governing equation [37]:

$$\rho \partial_t^2 \mathbf{u} = \nabla \cdot \boldsymbol{\sigma} + \mathbf{f}, \quad (2.2)$$

where \mathbf{u} is the displacement vector. ρ is mass density and \mathbf{f} is external force vector.

3. Formulation of 3D Spectral Element Method

For the Legendre polynomials-based 3D spectral finite element, it requires that the domain Ω in three dimensions is decomposed into a number of nonoverlapping hexahedrons, Ω_e , as in the conventional FE method. In SEM, the equations of wave propagation is [37]

$$\int_{\Omega} \rho \mathbf{w} \cdot \partial_t^2 \mathbf{u} \, d\Omega + \int_{\Omega} \nabla \mathbf{w} : \mathbf{C} : \nabla \mathbf{u} \, d\Omega = \int_{\Omega} \mathbf{w} \cdot \mathbf{f} \, d\Omega, \quad (3.1)$$

where the Ω denotes the physical region of interest and \mathbf{w} is an arbitrary test vector.

In SEM, the nodes are defined into two steps: (1) each element in its physical domain is mapped to a reference domain $\Lambda = [-1, 1]^3$ using an invertible local mapping f ; a set of basis functions consisting of Legendre polynomials of degree N are introduced; (2) a set of

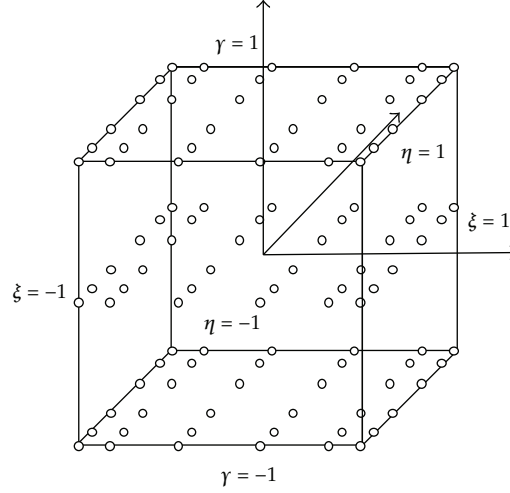


Figure 2: A 108-node spectra element in the local coordinate.

nodes are defined as $\xi_i \in [-1, 1], i = 1, \dots, N+1$. These Gauss-Lobatto-Legendre (GLL) points are the $(N+1)$ roots of [29]

$$(1 - \xi^2)P'_N(\xi) = 0, \quad (3.2)$$

where $P'_N(\xi)$ is the derivative of the Legendre polynomial of degree N . The ξ_i are different from the classical FE method in which the nodes are uniformly spaced. As an example, a 108-node spectral element in the local coordinate is shown in Figure 2.

The Lagrange interpolation function, u_N^e , supported by the GLL points can be expressed as

$$\begin{aligned} u_N^e(\xi, \eta, \gamma) &= \sum_{m=1}^{n_1} \sum_{n=1}^{n_2} \sum_{r=1}^{n_3} u_N^e(\xi_m, \eta_n, \gamma_r) h_m(\xi) h_n(\eta) h_r(\gamma) \\ &= \sum_{m=1}^{n_1} \sum_{n=1}^{n_2} \sum_{r=1}^{n_3} u_N^e(\xi_m, \eta_n, \gamma_r) \Psi_{mnr}, \end{aligned} \quad (3.3)$$

where Ψ_{mnr} is defined as the orthogonal shape functions in 3-D $h_m(\xi)$ denotes the m th 1D Lagrange interpolation at the $(N+1)$ GLL points defined above. The property of $h_m(\xi)$ is

$$h_m(\xi_n) = \delta_{mn}, \quad (3.4)$$

where δ_{mn} denotes the Kronecker delta and $n_i, i = 1, 2, 3$, are the numbers of GLL points in each direction in the local coordinate.

Therefore, the element matrices, \mathbf{M}^e (mass matrix), \mathbf{K}^e (stiffness matrix), and \mathbf{F}^e (force vectors), are calculated numerically on the reference coordinate:

$$\begin{aligned}
 \mathbf{M}^e &= \rho \int_{\Omega_e} (\boldsymbol{\Psi}^e(x, y, z))^T (\boldsymbol{\Psi}^e(x, y, z)) d\Omega_e \\
 &= \rho \int_{-1}^{+1} \int_{-1}^{+1} \int_{-1}^{+1} (\boldsymbol{\Psi}^e(\xi, \eta, \gamma))^T (\boldsymbol{\Psi}^e(\xi, \eta, \gamma)) \det[\mathbf{J}_e] d\xi d\eta d\gamma \\
 &= \rho \sum_{i=1}^{n_1} \omega_i \sum_{j=1}^{n_2} \omega_j \sum_{k=1}^{n_3} \omega_k [\boldsymbol{\Psi}^e(\xi_i, \eta_j, \gamma_k)]^T [\boldsymbol{\Psi}^e(\xi_i, \eta_j, \gamma_k)] \det[\mathbf{J}_e], \\
 \mathbf{K}^e &= \int_{\Omega_e} (\mathbf{B}^e(x, y, z))^T \mathbf{D}^e(\mathbf{B}^e(x, y, z)) d\Omega_e \\
 &= \int_{-1}^{+1} \int_{-1}^{+1} \int_{-1}^{+1} (\mathbf{B}^e(\xi, \eta, \gamma))^T \mathbf{D}^e(\mathbf{B}^e(\xi, \eta, \gamma)) \det[\mathbf{J}_e] d\xi d\eta d\gamma \quad (3.5) \\
 &= \sum_{i=1}^{n_1} \omega_i \sum_{j=1}^{n_2} \omega_j \sum_{k=1}^{n_3} \omega_k [\mathbf{B}^e(\xi_i, \eta_j, \gamma_k)]^T \mathbf{D}^e[\mathbf{B}^e(\xi_i, \eta_j, \gamma_k)] \det[\mathbf{J}_e], \\
 \mathbf{F}^e &= \int_{\Omega_e} (\boldsymbol{\Psi}^e(x, y, z))^T \mathbf{P} d\Omega_e \\
 &= \int_{-1}^{+1} \int_{-1}^{+1} \int_{-1}^{+1} (\boldsymbol{\Psi}^e(\xi, \eta, \gamma)) \mathbf{P}(\xi, \eta, \gamma) \det[\mathbf{J}_e] d\xi d\eta d\gamma \\
 &= \sum_{i=1}^{n_1} \omega_i \sum_{j=1}^{n_2} \omega_j \sum_{k=1}^{n_3} \omega_k [\boldsymbol{\Psi}^e(\xi_i, \eta_j, \gamma_k)]^T \mathbf{P}(\xi_i, \eta_j, \gamma_k) \det[\mathbf{J}_e],
 \end{aligned}$$

where ρ is the mass density, \mathbf{D}^e is termed material stiffness matrix, and \mathbf{P} is a distributed load. $\boldsymbol{\Psi}^e$ are the shape functions based on the Legendre polynomials. The matrix \mathbf{B}^e is the strain-displacement matrix calculated by

$$\mathbf{B}^e = \mathbf{L} \boldsymbol{\Psi}^e(x, y, z), \quad (3.6)$$

where \mathbf{L} denotes a differential operator matrix:

$$\mathbf{L} = \begin{bmatrix} \partial_x & 0 & 0 & \partial_y & 0 & \partial_z \\ 0 & \partial_y & 0 & \partial_x & \partial_z & 0 \\ 0 & 0 & \partial_z & 0 & \partial_y & \partial_x \end{bmatrix}^T. \quad (3.7)$$

\mathbf{J}_e is the Jacobian matrix associated with the mapping f from the physical domain Ω_e to the reference domain Λ :

$$\mathbf{J}_e = \begin{bmatrix} \partial_{\xi}x & \partial_{\xi}y & \partial_{\xi}z \\ \partial_{\eta}x & \partial_{\eta}y & \partial_{\eta}z \\ \partial_{\gamma}x & \partial_{\gamma}y & \partial_{\gamma}z \end{bmatrix}. \quad (3.8)$$

The weights ω_i are defined by

$$\omega_i = \frac{2}{n(n-1)[P_{n-1}(\xi_i)]^2}, \quad i \in 1, \dots, n, \quad n = N + 1. \quad (3.9)$$

Therefore, wave equation (3.1) can be rewritten into matrix form and wave propagation modeling is transformed to an ordinary differential equation in time. Let \mathbf{U} denotes the global vector of unknown displacement in the medium. Then the ordinary differential equation can be written as

$$\mathbf{M}\ddot{\mathbf{U}} + \mathbf{K}\mathbf{U} = \mathbf{F}, \quad (3.10)$$

where \mathbf{M} denotes the global mass matrix, \mathbf{K} is the global stiffness matrix, and \mathbf{F} is the vector of time-dependent excitation force.

In this study, the differential equation (3.10) is solved using a central difference time integration scheme. Initial conditions of displacement and velocity are $\mathbf{U} = 0$ and $\dot{\mathbf{U}} = 0$ at the time $t = 0$, and the central difference time integration scheme is implemented as

$$\frac{1}{\Delta t^2}\mathbf{M}\mathbf{U}_{t+\Delta t} = \mathbf{F}_t - \left(\mathbf{K} - \frac{2}{\Delta t^2}\mathbf{M}\right)\mathbf{U}_t - \frac{1}{\Delta t^2}\mathbf{M}\mathbf{U}_{t-\Delta t}, \quad (3.11)$$

where the symbol t denotes time and Δt denotes the time step of integration. In the central difference time integration scheme, the stable condition is $\Delta t \leq \Delta t_{cr} = L/c$, where L is the minimum distance between two adjacent nodes and c is the wave speed in elastic medium.

In comparison with FE, less computation effort is required for SFE because of the choice of Lagrange interpolation supported on the GLL points in conjunction with the GLL integration rule. The efficiency of SEM was demonstrated using two 3D models based on SFEs and FEs with the same degrees of freedom, and a reduction of about 65% in CPU time for calculation is used in comparison with the FEM.

4. Numerical Calculation

Lamb wave propagation in 8-ply T300/F593 composite laminates is analyzed in this study. The material properties of unidirectional lamina are listed in Table 1. Three types of composite laminates, namely, unidirectional $[0_8]$, symmetric cross-ply $[0_2/90_2]_s$, and quasi-isotropic $[+45/45/0/90]_s$ laminates are investigated. All the laminates have the same geometric configurations of $500 \text{ mm} \times 500 \text{ mm} \times 1.72 \text{ mm}$, as shown in Figure 3. The composite plate

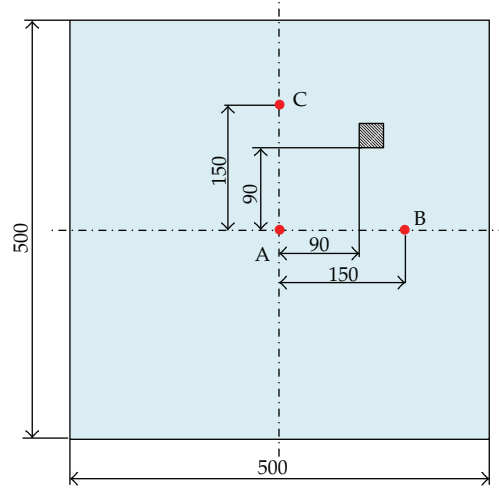


Figure 3: Scheme of composite laminate containing a delamination.

Table 1: Material properties of composite lamina.

E_1 (GPa)	E_2 (GPa)	E_3 (GPa)	G_{12} (GPa)	G_{13} (GPa)	G_{23} (GPa)	ν_{12}	ν_{13}	ν_{23}	ρ (10^3 kg/m ³)
128.1	8.2	8.2	4.7	4.7	3.44	0.27	0.27	0.2	1.57

was meshed using the three-dimensional spectral finite elements with 108-node (shown in Figure 2).

In the literature, piezoelectric (PZT) wafer is one of the frequently applied transducers to excite and capture Lamb waves propagating in structures for damage detection. The PZT transducers can be modeled by adding force to the incident points or using electromechanical coupling for elastic wave modeling in structures [38, 39]. In the present study, in order to obtain relatively simple Lamb wave mode, two forces perpendicular to the plane of the plate are applied at point A in Figure 3 on the upper and the lower surfaces of the plate, respectively. When the two forces are in phase, antisymmetric modes are activated, and when the two forces are out of phase, symmetric modes are excited. The excitation force is a 5-cycle sinusoidal signal modulated by Hanning window with a center frequency of 100 kHz and absolute maximum magnitude is 1N, as shown in Figure 4. The displacement responses at point B and C on the upper surface of the composite laminate are used to investigate wave propagation characteristics.

4.1. Wave Propagation in a Multilayered Composite Plate

As aforementioned, three types of the composite laminates are analyzed in this study. Firstly, Lamb wave propagation in the unidirectional composite laminate $[0]_8$ is investigated. The plate is meshed to $50 \times 50 \times 1$ spectral elements. Under the two excitation of in-phase forces, the fundamental antisymmetric mode A_0 is excited. According to the simulation results, the displacement component in the z -direction is dominant. Therefore, only the displacement component in the z -direction is analyzed here. Responses of the laminate at 0.097 ms are

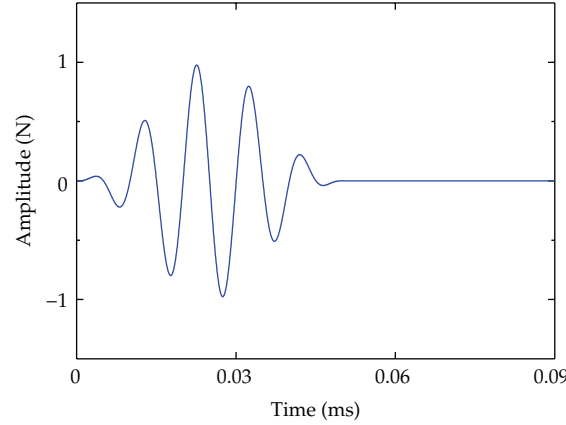


Figure 4: Waveform of the excitation force in the time domain.

plotted in Figure 5(a). It can be observed that the wave front of the A_0 mode has ellipse-like shape, and the group velocity in the fibre direction is greater than that in the direction perpendicular to the fibre, indicating that group velocity of this type of wave mode in the composite depends on the orientation of wave propagation. Generally, group velocity in composite laminate is a function of the direction of wave propagation and direction of the fibres. The group velocity in composite laminates can be calculated analytically using the transfer matrix method (In the appendix). For such an 8-ply unidirectional laminate, the analytical group velocity is plotted in a polar coordinate, as shown in Figure 5(b). It presents similar feature as Figure 5(a). Group velocities in the direction along the fibres (x -axis) and perpendicular to the fibres (y -axis) are further calculated from displacement responses of SEM simulations at the point B and C, as shown in Figure 6. Based on the peak of the received responses, time of flight (ToF) from point A to B can be defined. The calculated group velocity c_g of the A_0 mode of Lamb waves propagating in the x direction is 1794 m/s, which is 2.6% smaller than the analytical value. In a similar way, the group velocity of the A_0 mode in the y -direction is 1319 m/s and the one calculated analytically is 1245 m/s, which gives a relative error of 5.9%. It can be concluded that the simulation results of SEM model, the proposed model, are in good agreement with the analytical results thus validating the effectiveness of the model.

Under the two excitations of out-of-phase forces, the fundamental symmetric wave modes, the S_0 mode and the SH_0 mode, are excited. According to the simulation results, the displacement components in the x -direction and in the y -direction are dominated. Hence, only those two displacement components are plotted, as shown in Figures 7(a) and 7(b). It can be seen that S_0 mode and the SH_0 mode are excited simultaneously, which is because the S_0 mode and the SH_0 mode are coupled in multilayered composite laminate. Analytical group velocities of the S_0 mode and the SH_0 mode are also calculated, as shown in Figure 7(c), and the simulation results of SEM modeling are in good agreement of the analytical results.

In case of cross-ply laminates $[0_2/90_2]_s$, the laminate was meshed to $50 \times 50 \times 4$ spectral finite elements. The symmetric mode and antisymmetric modes are excited using the above-mentioned method. In case of antisymmetric mode, the displacement component in the z -direction is shown in Figure 8. On the other hand, in case of symmetric mode the displacement in the x -direction and the y -direction are plotted in Figure 9. The complexity

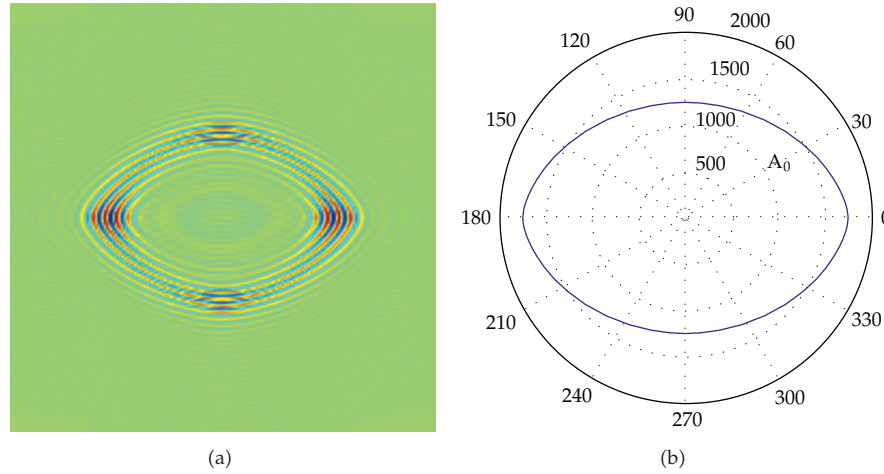


Figure 5: Displacement component in the z -direction at 0.097 ms under (a) the A_0 mode and (b) theoretical group velocity.

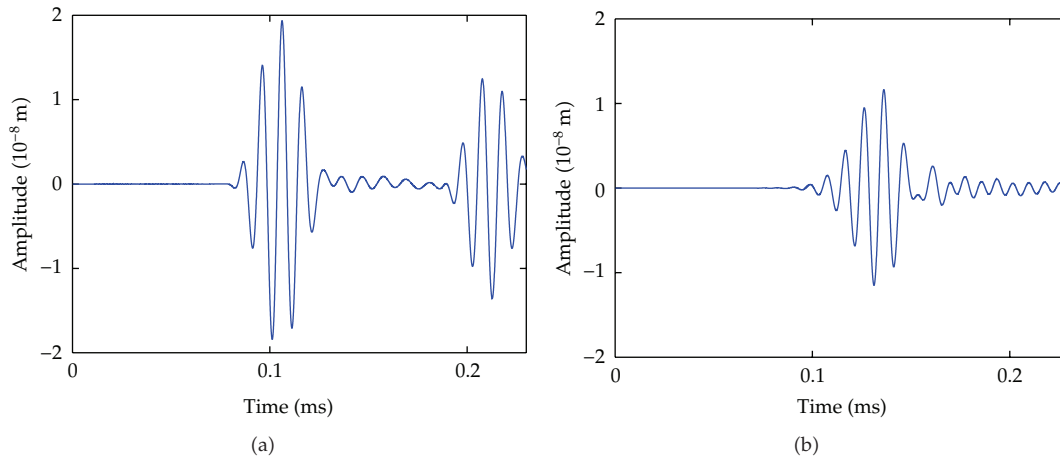


Figure 6: Displacement response in the z -direction at point B (a) and at point C (b).

of Lamb wave propagation in composite is also demonstrated, and the effectiveness of the proposed model is validated by comparison of simulation results and the analytical results.

In case of angle-ply laminates $[-45/45/0/90]_s$, the composite laminate is meshed by using $50 \times 50 \times 8$ spectral finite elements. The displacement components in the z -direction at 0.086 ms are plotted in Figure 10(a), while displacement components in the x -direction and in the y -direction at 0.069 ms are plotted in Figures 11(a) and 11(b). The group velocities of analytical solutions for those Lamb modes are also plotted in a polar coordinate for comparison, as shown in Figures 10(b) and 11(c). A good agreement found in both symmetric and antisymmetric modes. It can be observed that the angular dependence of Lamb modes in the laminates $[-45/45/0/90]_s$ becomes weaker because of its quasi-isotropic layup. Under the S_0 and the SH_0 modes, the group velocities are approximately independent of direction of wave propagation, but it still can be discerned that the A_0 mode has the maximum in the 45°

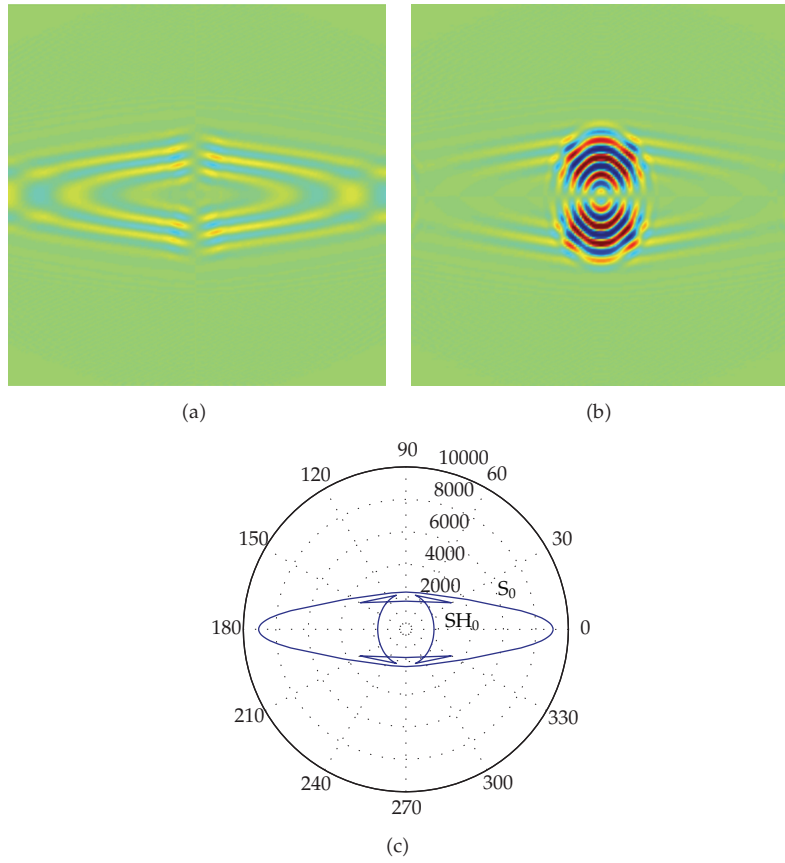


Figure 7: Displacement components in (a) the x -direction and (b) the y -direction at 0.039 ms under the S_0 and the SH_0 modes and (c) theoretical group velocity.

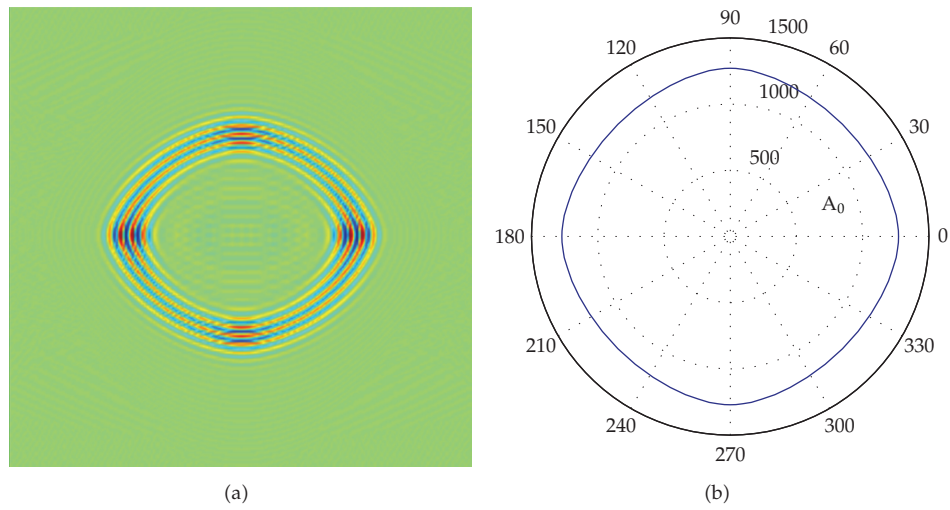


Figure 8: Displacement component in the z -direction at 0.097 ms under (a) the A_0 mode and (b) analytical group velocities.

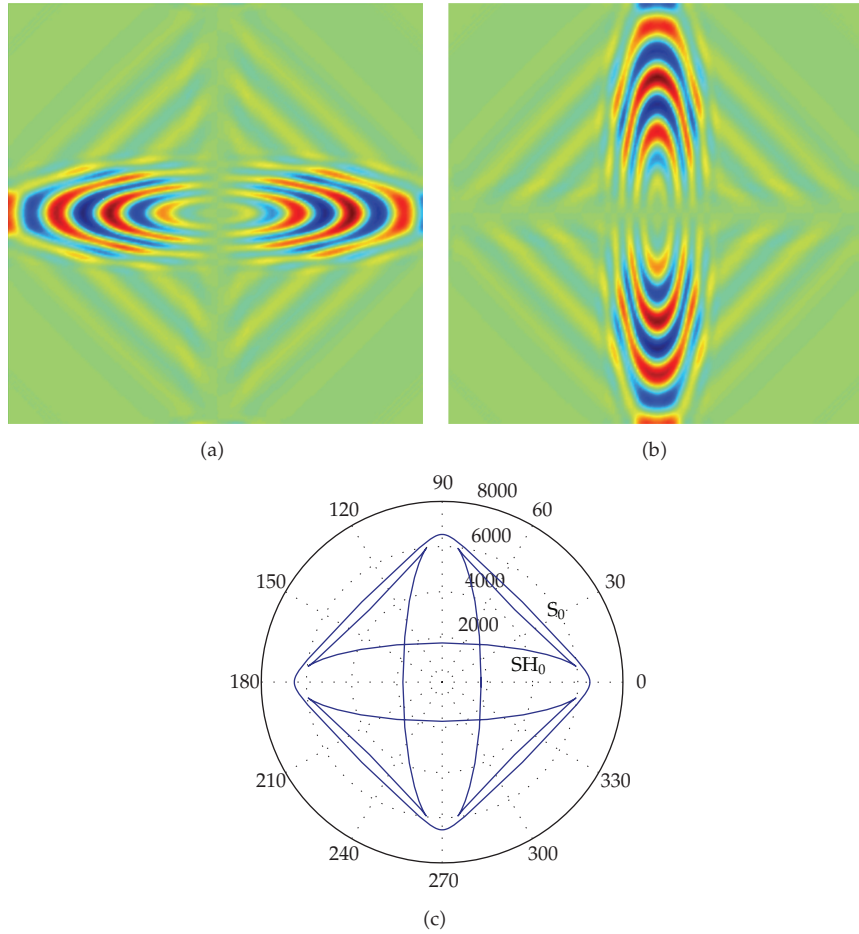


Figure 9: Displacement components in (a) the x -direction and in (b) the y -direction at 0.097 ms under the S_0 and the SH_0 modes and (c) theoretical group velocity.

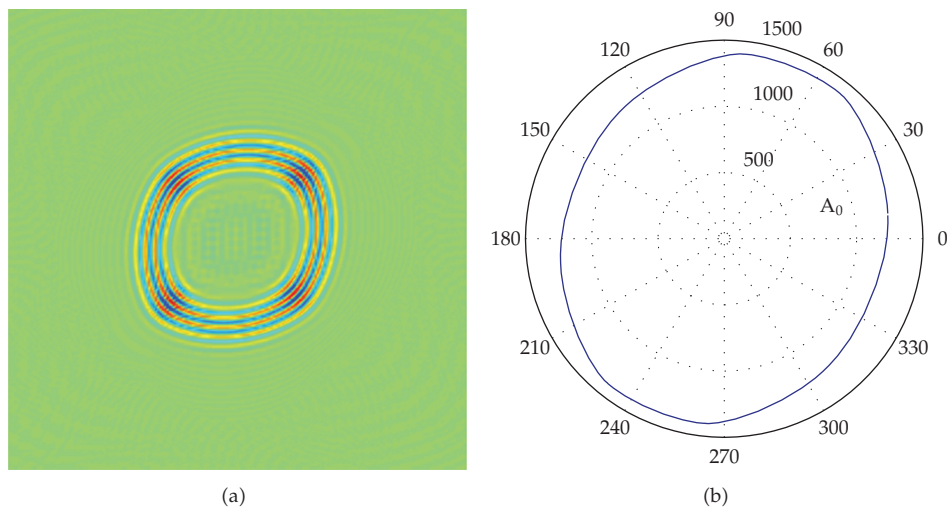


Figure 10: Displacement component in (a) the z -direction at 0.086 ms under the A_0 mode and (b) analytical group velocities.

(or 225°) directions because outer lamina are orientated in these directions, which dominates the bending properties related to A_0 mode.

In case of angle-ply laminate, the wavelength of the A_0 mode is shorter than that of the S_0 and the SH_0 modes in composite laminate from the simulation results and analytical results. It can be expected that the A_0 mode is possibly more sensitive to small damage than the S_0 mode and the SH_0 mode because of its short wavelength.

It is demonstrated that characteristics of the wave propagation in multilayered composite is complex due to the nature of anisotropic of the material constants and the multilayered configurations, which leads to the group velocity of Lamb waves depending on the laminate layup and the direction of wave propagation. Good agreement between the simulation results based on SEM and the analytical results demonstrates that the proposed model provides an effective tool to investigate the wave propagation in composite structures.

4.2. Wave Propagation in a Composite Plate Containing Delamination

The typical damage forms in composite laminate are transverse microcracking, fiber-breakage, and delamination. Typically, the transverse microcracking through the thickness of the ply occurs as the first-ply failure, and then delamination damage follows. The fiber breakage usually happens at the last stage of the failure. However, a catastrophic failure can occur only with the microcracking and delamination damage without the fiber breakage. Delamination is known to happen because of excessive interlamina normal and shear stress at the ply boundaries, which not only causes reduction in stiffness, but also affects the strength and integrity of the structure, leading to failure.

The wave propagation in composite laminates containing a delamination is investigated in this study. The delamination in the laminates is modeled using nodes separation method. Laminate without delamination is initially meshed. At the interface between the adjacent elements where the delamination occurs, nodes that are affected by the delamination are separated, as shown in Figure 12.

Lamb wave modes interaction with delamination is analyzed in quasi-isotropic laminates $[45/-45/0/90]_s$ using the proposed 3D SEM model. The size of the delamination is $30\text{ mm} \times 30\text{ mm}$ in a square shape, as shown in Figure 3. The wave interaction of the symmetric mode and antisymmetric mode with delamination is investigated.

The effects of the delamination at different interfaces in the composite laminate are addressed. Under the symmetric mode, the displacement responses at the point B in the x - and the y -directions are plotted in Figure 13. Responses of the intact composite laminate are also provided for comparison. It is evident that the scattered waves from the delamination are not so obvious in comparison with the intact laminate, on the captured responses at the point B, when the delamination is located in different interfaces. The displacement responses at 0.069 ms in the x - and the y -directions of the composite laminates are plotted in Figure 14, when there is a delamination at the interfaces between 3-4 layers. However, when the delamination is at the interface between 4-5 layers, responses of the point B are same as those from intact composite laminate, indicating that the symmetric mode is insensitive to the delamination in the symmetric plane of the plate, attributed to the reason that the layup of the composite laminate is symmetric about the central plane between 4-5 layers. Therefore, the symmetric wave mode related to extensional wave mode can travel through the delamination without any scattering from it.

Under the antisymmetric mode, the displacements at the point B in the z -direction are plotted in Figure 15. It can be seen that the antisymmetric mode is more sensitive to

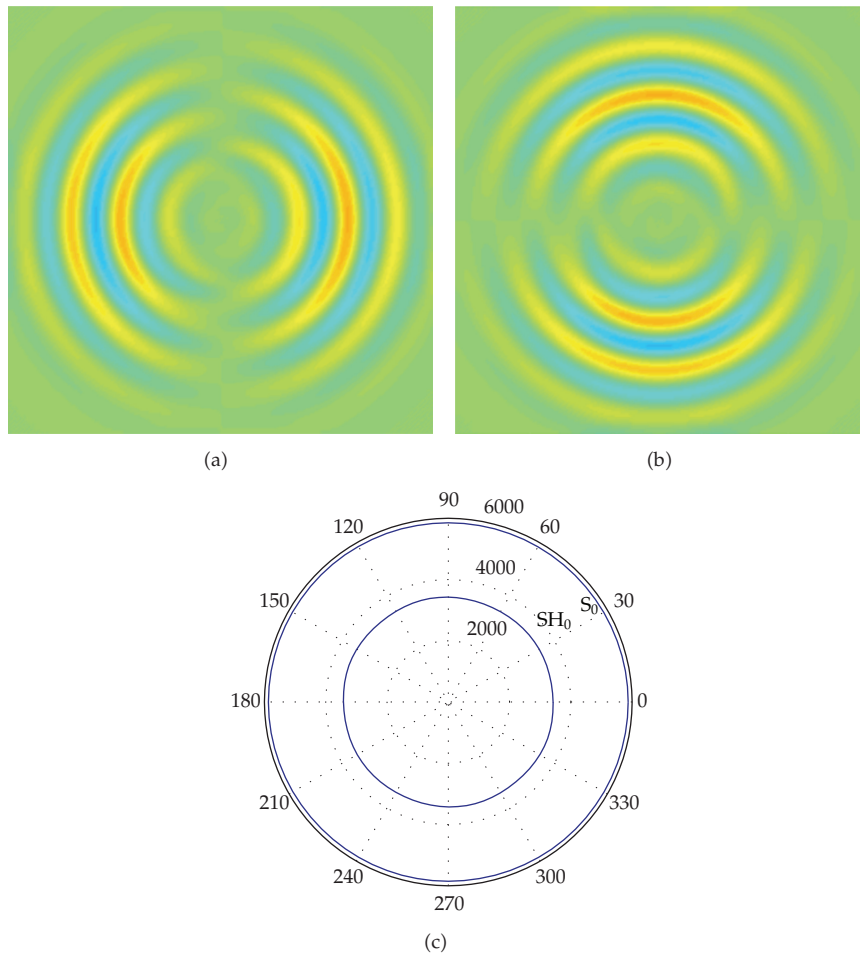


Figure 11: Displacement components in (a) the x -direction and in (b) the y -direction at 0.069 ms under the S_0 and the SH_0 modes and (c) theoretical group velocity.

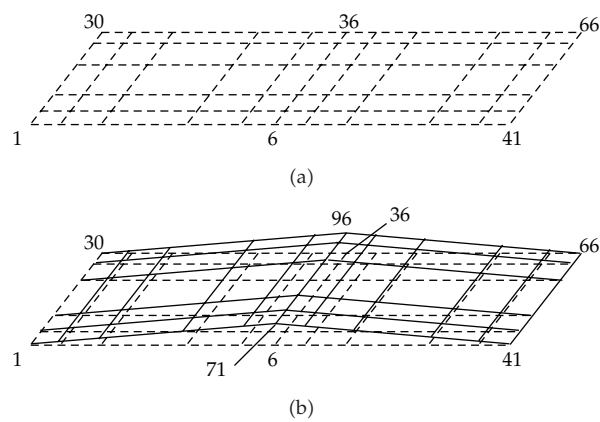


Figure 12: Modeling of delamination in a laminate (a) mesh without delamination and (b) mesh with a delamination.

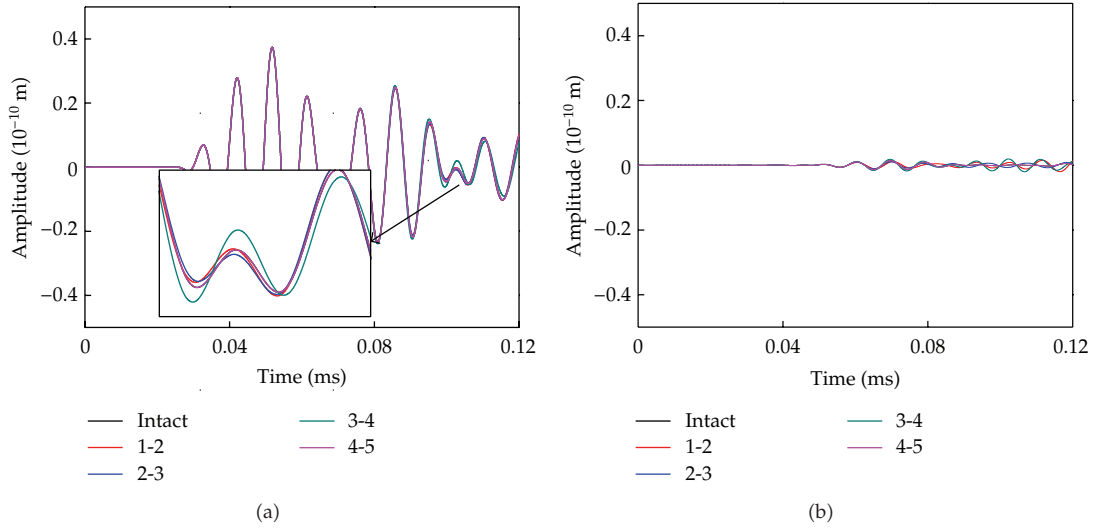


Figure 13: Displacement components in (a) the x -direction and (b) the y -direction at the point B as the delamination is located in different interfaces.

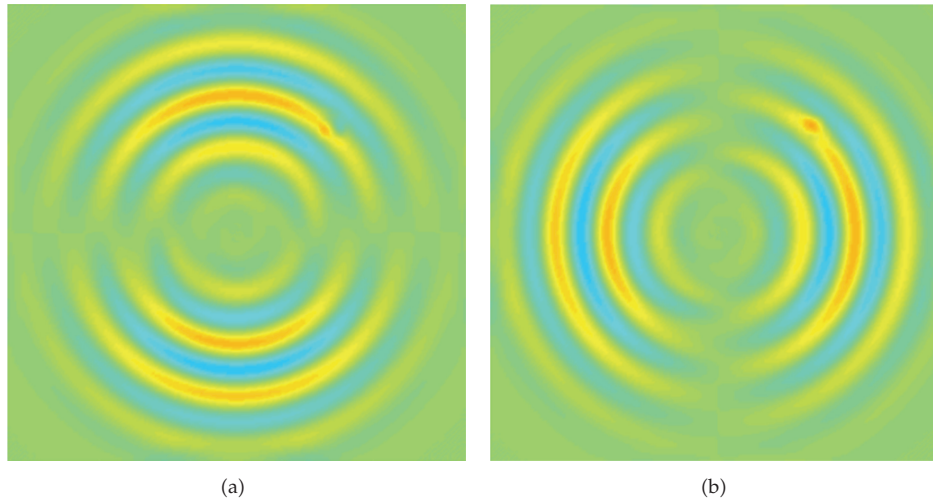


Figure 14: Displacement components in (a) the x -direction and (b) the y -direction of composite laminate at 0.069 ms with a delamination.

delamination located at all interfaces of the composite laminate. The displacement responses of the laminate in the z -direction at 0.173 ms are plotted in Figure 16.

Under the same excitation frequency, the scattered waves from delamination become clearer in the captured response at the point B under the antisymmetric mode than that under symmetric mode. Hence, the antisymmetric mode can be used to detect smaller delamination than the symmetric mode, since the wavelength of the antisymmetric mode is less than that of the symmetric mode. In addition, according to the simulation results, the symmetric mode may be less sensitive to delamination located at certain interfaces. It can be expected that the antisymmetric mode is more suitable for identification of the delamination.

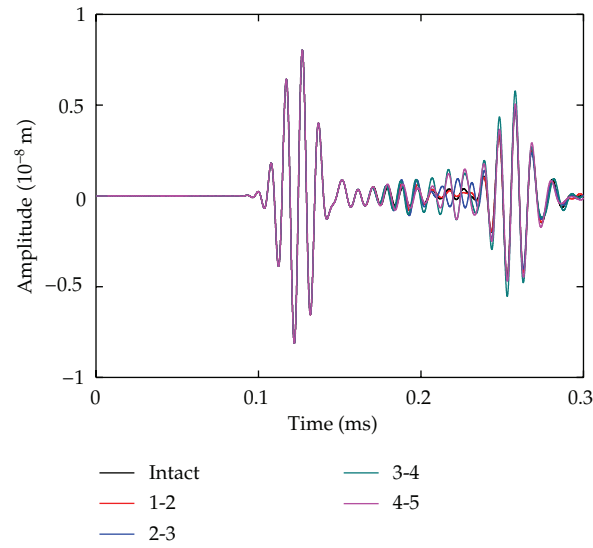


Figure 15: Displacement component in the z-direction at the point B as the delaminations are located in different interfaces.

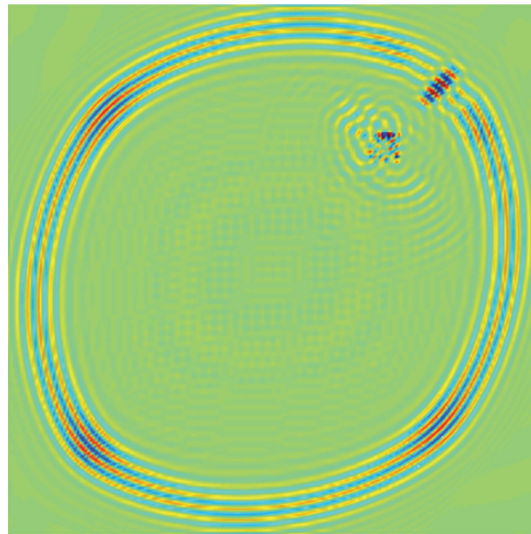


Figure 16: Displacement component in the z-direction of composite laminate at 0.173 ms with a delamination.

The scattered waves are very weak compared with the incident wave, resulting in that the reflected wave packet is difficult to identify delamination in such composite materials with a high attenuation ratio. Fortunately, the transmitted wave has been affected a lot, as shown in Figure 16.

5. Conclusions

A three-dimensional spectral element method is developed to investigate the wave propagation characteristics in composite laminates in the present study. Three types of laminates, namely, unidirectional $[0]_8$, cross-ply $[0_2/90_2]_s$, and quasi-isotropic $[-45/45/0/90]_s$ laminates are modeled using 3D spectral elements, and the laminates are excited using two forces in-phase and out-of-phase to generate the symmetric mode and antisymmetric mode respectively. It is demonstrated that the proposed 3D spectral element method can be efficiently and effectively used to simulate wave propagation in composite laminates. Complexity of wave propagation characteristic is also demonstrated even for a single Lamb wave mode in composite laminates. Finally, interactions between the Lamb wave mode and a delamination are analyzed. It is concluded that symmetric mode of Lamb wave may be insensitive to delamination in certain interfaces in the laminate. And, therefore, it is essential to understand wave propagation characteristics in composite laminate when Lamb-wave-based structural health monitoring strategy is carried out.

Appendix

The analytical wave front can be calculated as follows.

Consider wave propagation solutions in the following form:

$$\{u, v, w\} = (1, V, W)Ue^{[i\xi(x_1 + \alpha x_3) - \omega t]}, \quad (\text{A.1})$$

where ξ is the wave number, ω is the circular frequency, α is still an unknown parameter, and V and W are ratios of the displacement amplitudes of v and w , respectively. The choice of the solution leads to the three coupled equations that can be written as

$$\begin{bmatrix} K_{11} & K_{12} & K_{13} \\ K_{21} & K_{22} & K_{23} \\ K_{31} & K_{32} & K_{33} \end{bmatrix} \begin{bmatrix} U_1 \\ U_2 \\ U_3 \end{bmatrix} = 0, \quad (\text{A.2})$$

where the elements of the matrix K are

$$\begin{aligned} K_{11} &= C_{11} + C_{55} - \rho c^2, \\ K_{12} &= C_{16} + C_{45}\alpha^2, \\ K_{13} &= (C_{13} + C_{55})\alpha, \\ K_{22} &= C_{66} - \rho c^2 + C_{44}\alpha^2, \\ K_{23} &= (C_{36} + C_{45})\alpha, \\ K_{33} &= C_{55} - \rho c^2 + C_{33}\alpha^2. \end{aligned} \quad (\text{A.3})$$

The existence of nontrivial solutions for U_1 , U_2 , and U_3 demands the vanishing of the determinant of the matrix K and yields the sixth-degree polynomial equation:

$$\alpha^6 + A_1\alpha^4 + A_2\alpha^2 + A_3 = 0. \quad (\text{A.4})$$

There are six roots of this equation, which correspond to the three sets of mode pairs. For each α_q , $q = 1, 2, \dots, 6$, the displacement ratios $V_q = U_{2q}/U_{1q}$ and $W_q = U_{3q}/U_{1q}$ can be expressed as

$$\begin{aligned} V_q &= \frac{K_{11}(\alpha_q)K_{23}(\alpha_q) - K_{13}(\alpha_q)K_{12}(\alpha_q)}{K_{13}(\alpha_q)K_{22}(\alpha_q) - K_{12}(\alpha_q)K_{23}(\alpha_q)}, \\ W_q &= \frac{K_{11}(\alpha_q)K_{23}(\alpha_q) - K_{12}(\alpha_q)K_{13}(\alpha_q)}{K_{12}(\alpha_q)K_{33}(\alpha_q) - K_{23}(\alpha_q)K_{13}(\alpha_q)}. \end{aligned} \quad (\text{A.5})$$

The formal solutions for the displacements and stresses in the expanded matrix form

$$\begin{bmatrix} u_1 \\ u_2 \\ u_3 \\ \sigma_{33} \\ \sigma_{13} \\ \sigma_{23} \end{bmatrix} = \begin{bmatrix} 1 & 1 & 1 & 1 & 1 & 1 \\ V_1 & V_1 & V_3 & V_3 & V_5 & V_5 \\ W_1 & -W_1 & W_3 & -W_3 & W_5 & -W_5 \\ D_{11} & D_{11} & D_{13} & D_{13} & D_{15} & D_{15} \\ D_{21} & -D_{21} & D_{23} & -D_{23} & D_{25} & D_{25} \\ D_{31} & -D_{31} & D_{33} & -D_{33} & D_{35} & -D_{35} \end{bmatrix} \begin{bmatrix} U_{11}E_1 \\ U_{12}E_2 \\ U_{13}E_3 \\ U_{14}E_4 \\ U_{15}E_5 \\ U_{16}E_6 \end{bmatrix}, \quad (\text{A.6})$$

where

$$\begin{aligned} E_q &= e^{i\xi\alpha_q x_3}, \\ D_{1q} &= i\xi(C_{13} + C_{36}V_q + C_{33}\alpha_q W_q), \\ D_{2q} &= i\xi[C_{55}(\alpha_q + W_q) + C_{45}\alpha_q V_q], \\ D_{3q} &= i\xi[C_{45}(\alpha_q + W_q) + C_{44}\alpha_q V_q], \\ q &= 1, 2, \dots, 6. \end{aligned} \quad (\text{A.7})$$

Acknowledgments

The authors are grateful for the support received from the National Natural Science Foundation of China (NSFC nos. 11072148 and 11061160491), Research Project of State Key Laboratory of Mechanical System and Vibration (MSV201110), and the National High Technology Research and Development Program of China (no. 2009AA044800).

References

- [1] L. Ye, Y. Lu, Z. Su, and G. Meng, "Functionalized composite structures for new generation airframes: a review," *Composites Science and Technology*, vol. 65, no. 9, pp. 1436–1446, 2005.
- [2] Z. Su, L. Ye, and Y. Lu, "Guided Lamb waves for identification of damage in composite structures: a review," *Journal of Sound and Vibration*, vol. 295, no. 3–5, pp. 753–780, 2006.
- [3] A. Raghavan and C. E. S. Cesnik, "Review of guided-wave structural health monitoring," *Shock and Vibration Digest*, vol. 39, no. 2, pp. 91–114, 2007.
- [4] Z. Su and L. Ye, "An intelligent signal processing and pattern recognition technique for defect identification using an active sensor network," *Smart Materials and Structures*, vol. 13, no. 4, pp. 957–969, 2004.
- [5] Z. Su and L. Ye, "Lamb wave propagation-based damage identification for quasi-isotropic CF/EP composite laminates using artificial neural algorithm: part II—implementation and validation," *Journal of Intelligent Material Systems and Structures*, vol. 16, no. 2, pp. 113–125, 2005.
- [6] X. Wang, G. Foliente, Z. Su, and L. Ye, "Multilevel decision fusion in a distributed active sensor network for structural damage detection," *Structural Health Monitoring*, vol. 5, no. 1, pp. 45–58, 2006.
- [7] N. Hu, S. Takahito, F. Hisao, and Z. Su, "Damage identification of metallic structures using A_0 mode of lamb waves," *Structural Health Monitoring*, vol. 7, no. 3, pp. 271–285, 2008.
- [8] J. C. Strikwerda, Ed., *Finite Difference Schemes and Partial Differential Equations*, 2nd edition, 2004.
- [9] J. C. Strikwerda, *Finite Difference Schemes and Partial Differential Equations*, Wadsworth Publishing Company, 1989.
- [10] O. C. Zienkiewicz, *The Finite Element Method*, McGraw-Hill, London, UK, 4th edition, 1989.
- [11] Y. Liu, N. Hu, C. Yan, X. Peng, and B. Yan, "Construction of a Mindlin pseudospectral plate element and evaluating efficiency of the element," *Finite Elements in Analysis and Design*, vol. 45, no. 8–9, pp. 538–546, 2009.
- [12] N. Hu, H. H. Wang, B. Yan, H. Fukunaga, D. R. Mahapatra, and S. Gopalakrishnan, "The partition of unity finite element method for elastic wave propagation in Reissner-Mindlin plates," *International Journal for Numerical Methods in Engineering*, vol. 70, no. 12, pp. 1451–1479, 2007.
- [13] Y. Cho and J. L. Rose, "A boundary element solution for a mode conversion study on the edge reflection of Lamb waves," *Journal of the Acoustical Society of America*, vol. 99, no. 4, pp. 2097–2109, 1996.
- [14] X. G. Zhao and J. L. Rose, "Boundary element modeling for defect characterization potential in a wave guide," *International Journal of Solids and Structures*, vol. 40, no. 11, pp. 2645–2658, 2003.
- [15] A. Bergamini and F. Biondini, "Finite strip modeling for optimal design of prestressed folded plate structures," *Engineering Structures*, vol. 26, no. 8, pp. 1043–1054, 2004.
- [16] D. J. Dawe, "Use of the finite strip method in predicting the behaviour of composite laminated structures," *Composite Structures*, vol. 57, no. 1–4, pp. 11–36, 2002.
- [17] P. P. Delsanto and M. Scalerandi, "A spring model for the simulation of the propagation of ultrasonic pulses through imperfect contact interfaces," *Journal of the Acoustical Society of America*, vol. 104, no. 5, pp. 2584–2591, 1998.
- [18] P. P. Delsanto, R. S. Schechter, H. H. Chaskelis, R. B. Mignogna, and R. Kline, "Connection machine simulation of ultrasonic wave propagation in materials. II: the two-dimensional case," *Wave Motion*, vol. 20, no. 4, pp. 295–314, 1994.
- [19] P. P. Delsanto, R. S. Schechter, and R. B. Mignogna, "Connection machine simulation of ultrasonic wave propagation in materials III: the three-dimensional case," *Wave Motion*, vol. 26, no. 4, pp. 329–339, 1997.
- [20] P. P. Delsanto, T. Whitcombe, H. H. Chaskelis, and R. B. Mignogna, "Connection Machine simulation of ultrasonic wave propagation in materials. I. The one-dimensional case," *Wave Motion*, vol. 16, no. 1, pp. 65–80, 1992.
- [21] Y. Sohn and S. Krishnaswamy, "Mass spring lattice modeling of the scanning laser source technique," *Ultrasonics*, vol. 39, no. 8, pp. 543–551, 2002.
- [22] B. C. Lee and W. J. Staszewski, "Lamb wave propagation modelling for damage detection: II. Damage monitoring strategy," *Smart Materials and Structures*, vol. 16, no. 2, article 004, pp. 260–274, 2007.
- [23] B. C. Lee and W. J. Staszewski, "Lamb wave propagation modelling for damage detection: I. two-dimensional analysis," *Smart Materials and Structures*, vol. 16, no. 2, article 003, pp. 249–259, 2007.
- [24] J. F. Doyle, *Wave Propagation in Structures*, Springer, New York, NY, USA, 1989.
- [25] A. T. Patera, "A spectral element method for fluid dynamics: laminar flow in a channel expansion," *Journal of Computational Physics*, vol. 54, no. 3, pp. 468–488, 1984.

- [26] N. Hu, H. Fukunaga, M. Kameyama, D. R. Mahapatra, and S. Gopalakrishnan, "Analysis of wave propagation in beams with transverse and lateral cracks using a weakly formulated spectral method," *Journal of Applied Mechanics*, vol. 74, no. 1, pp. 119–127, 2007.
- [27] M. Krawczuk, M. Palacz, and W. Ostachowicz, "The dynamic analysis of a cracked Timoshenko beam by the spectral element method," *Journal of Sound and Vibration*, vol. 264, no. 5, pp. 1139–1153, 2003.
- [28] D. Komatitsch, C. Barnes, and J. Tromp, "Simulation of anisotropic wave propagation based upon a spectral element method," *Geophysics*, vol. 65, no. 4, pp. 1251–1260, 2000.
- [29] D. Komatitsch and J. Tromp, "Introduction to the spectral element method for three-dimensional seismic wave propagation," *Geophysical Journal International*, vol. 139, no. 3, pp. 806–822, 1999.
- [30] R. Sridhar, A. Chakraborty, and S. Gopalakrishnan, "Wave propagation analysis in anisotropic and inhomogeneous uncracked and cracked structures using pseudospectral finite element method," *International Journal of Solids and Structures*, vol. 43, no. 16, pp. 4997–5031, 2006.
- [31] P. Kudela, M. Krawczuk, and W. Ostachowicz, "Wave propagation modelling in 1D structures using spectral finite elements," *Journal of Sound and Vibration*, vol. 300, no. 1-2, pp. 88–100, 2007.
- [32] P. Kudela, A. Zak, M. Krawczuk, and W. Ostachowicz, "Modelling of wave propagation in composite plates using the time domain spectral element method," *Journal of Sound and Vibration*, vol. 302, no. 4-5, pp. 728–745, 2007.
- [33] A. Zak, M. Krawczuk, and W. Ostachowicz, "Propagation of in-plane waves in an isotropic panel with a crack," *Finite Elements in Analysis and Design*, vol. 42, no. 11, pp. 929–941, 2006.
- [34] H. Peng, G. Meng, and F. Li, "Modeling of wave propagation in plate structures using three-dimensional spectral element method for damage detection," *Journal of Sound and Vibration*, vol. 320, no. 4-5, pp. 942–954, 2009.
- [35] N. Hu, T. Shimomukai, C. Yan, and H. Fukunaga, "Identification of delamination position in cross-ply laminated composite beams using S0 Lamb mode," *Composites Science and Technology*, vol. 68, no. 6, pp. 1548–1554, 2008.
- [36] L. Wang and F. G. Yuan, "Group velocity and characteristic wave curves of Lamb waves in composites: modeling and experiments," *Composites Science and Technology*, vol. 67, no. 7-8, pp. 1370–1384, 2007.
- [37] D. Komatitsch, S. Tsuboi, and J. Tromp, *The Spectral-Element Method in Seismology*, vol. 157 of *Geophysical Monograph*, American Geophysical Union, 2005.
- [38] A. Lonkar and F. K. Chang, "Development of SEM-based PESEA code for modeling PZT induced acousto-ultrasonic waves propagation in metallic and composite structures," in *Proceedings of the 8th International Workshop on Structural Health Monitoring*, vol. 2, pp. 2512–2520, Stanford, Calif, USA, 2011.
- [39] P. Kudela and W. Ostachowicz, "Spectral elements with electro-mechanical coupling for elastic wave modeling in 3D solids," in *Proceedings of the 4th European Conference on Computational Mechanics, Solids, Structures and Coupled Problems in Engineering*, Paris, France, May 2010.